Oceanic bottom boundary layers and abyssal overturning circulation

Thesis by

Xiaozhou Ruan

In Partial Fulfillment of the Requirements for the
Degree of
Doctor of Philosophy

CALIFORNIA INSTITUTE OF TECHNOLOGY
Pasadena, California

2019
Defended February 26, 2019

To my parents and my wife

ACKNOWLEDGEMENTS

I thank my advisor, as well as my friend, Andy Thompson, for his patience, support and encouragement throughout my doctoral training. I am always impressed by his intelligence and broad interests in both science and life. I thank him for taking me on two Antarctic adventures, which were invaluable experiences. I especially thank him for his belief in me when admitting me to the graduate program at Caltech from China. I will forever be grateful for this.

I would also like to thank Jörn Callies for spending time with me in a very fun project in which I got to learn many new topics and techniques. I look forward to continuing this enjoyable collaboration with him in the future. My other committee members, Tapio Schneider, Beverley McKeon and Andrew Stewart offered helpful comments and criticism on my research, which greatly improved my thesis work. A special thanks goes to John Taylor, who led me into the numerical world and helped me patiently via countless emails.

I was fortunate to have Mar Flexas in the group who introduced me to traditional observational oceanography. She was always there to encourage me when times were difficult and I will miss our afternoon tea times. I thank Georgy Manucharyan for answering all of my questions and for always pushing me to think in big pictures. It was great to have him sit by my side for almost four years. This thesis would not have been possible without my fellow friends in ESE and GPS. I want to thank Zach Erickson, Giuliana Viglione, Lia Siegelman, Eric Praske, Sally Zhang, Ho-Hsuan Wei and Emily Newsom for making my stay at Caltech lively.

Last but not the least, I thank my parents, Ding Ruan and Jian Zhou for their support and understanding across the Pacific. I thank my wife, Yuan Zhou, for coming to the United States. It feels wonderful to have a family here.

The work presented here was supported by the National Science Foundation through OPP-1246460 and OPP-1644172.

ABSTRACT

The vast amount of carbon and heat exchange between the abyssal and upper ocean and subsequently the atmosphere is paced by the abyssal overturning circulation. A key component of the abyssal overturning circulation is the formation and consumption of the densest water mass on Earth, Antarctic Bottom Water (AABW), namely the conversion of North Atlantic Deep Water (NADW) to AABW and the consumption of AABW via small-scale diapycnal mixing. Yet, this pathway of AABW spanning thousands of kilometers has not been successfully reproduced in large-scale general circulation models (GCM). What is missing is essentially the understanding and resolution of small-scale physics involved in converting deep and bottom waters from one density class to another, the water mass transformation (WMT). In this thesis, we focus on small-scale (both in the horizontal and vertical directions) dynamics near the BBL, where enhanced shear, mixing and turbulence exist to facilitate effective WMT above the seafloor.

From high-resolution ocean glider observations around Antarctica, we find that a portion of Lower Circumpolar Deep Water, a branch of NADW, becomes lighter via mixing with light shelf water over the continental slope and shelf, instead of being converted into dense AABW under sea ice. This mixing is likely induced by submesoscale symmetric instability coming from a strong boundary current interacting with the sloping topography in the BBL. We then consider how to sustain the consumption of AABW in the global mid-ocean ridge system. Using numerical models, we show that submesoscale baroclinic eddies are crucial to maintaining strong stratification over the flanks of the mid-ocean ridges and thus permitting effective WMT. Lastly, we consider the interaction between external mean flows and stratified BBL over sloping topography. With the large-scale turbulence resolved in a large-eddy simulation model, we propose a new theoretical framework to describe the evolution of the BBL and the Eulerian advection of its associated stratification when external barotropic flows are present. This new framework can be used to parameterize bottom friction, important for closing the kinetic energy budget of the global ocean. We further extend this interaction to a horizontally-sheared and temporally-oscillating external mean flow and explore the response of the BBL and the BBL-interior mass exchange with simple turbulent parameterizations.

Using a combination of different approaches, we confirm that the long-overlooked oceanic BBL is the key location for closing the abyssal overturning circulation.

More importantly, without appropriate techniques to tackle the currently unresolved small-scale processes, they will likely remain a narrow bottleneck in understanding the abyssal overturning circulation.

PUBLISHED CONTENT AND CONTRIBUTIONS

Ruan, Xiaozhou, Andrew F Thompson, and John R Taylor (2019). “The evolution and arrest of a turbulent stratified oceanic bottom boundary layer over a slope: Downslope regime”. In: *Journal of Physical Oceanography* 49.2, pp. 469–487. DOI: `10.1175/JPO-D-18-0079.1`.
All authors conceived the study and wrote the paper. X.R. performed the numerical simulations and data analysis.

Ruan, Xiaozhou et al. (2017). “Contribution of topographically generated submesoscale turbulence to Southern Ocean overturning”. In: *Nature Geoscience* 10.11, pp. 840–845. DOI: `10.1038/NGEO3053`.
X.R. participated in the data collection, performed the data analysis and co-wrote the paper.

Ruan, Xiaozhou and Andrew F Thompson (2016). “Bottom boundary potential vorticity injection from an oscillating flow: A PV pump”. In: *Journal of Physical Oceanography* 46.11, pp. 3509–3526. DOI: `10.1175/JPO-D-15-0222.1`.
Both authors conceived the study and wrote the paper. X.R. performed the numerical simulations and data analysis.

TABLE OF CONTENTS

LIST OF ILLUSTRATIONS

LIST OF TABLES

Chapter 1

INTRODUCTION

The Earth has been in radiative imbalance, with heat trapped within its atmosphere since at least about 1970 (Murphy et al., 2009; Church et al., 2011; Levitus et al., 2012). About thirty-percent of this excessive heat is stored in the ocean below seven hundred meters (Rhein et al., 2013). Besides this large amount of heat, the abyssal ocean stores about sixty times more carbon than the atmosphere, making it the largest carbon reservoir in the climate system (Sigman and Boyle, 2000). Considering this enormous amount of carbon and heat storage, the abyssal ocean is thought to regulate Earth's climate over centennial to millennial timescales via its meridional overturning circulation (Clark et al., 2002; McManus et al., 2004). In the present abyssal circulation, the dense water mass that is formed in the north Atlantic, North Atlantic Deep Water (NADW), flows southward away from its formation site. As NADW approaches the Antarctic margin, it shoals towards the sea surface. As a consequence, part of NADW outcrops in regions where surface buoyancy forcing is positive and this part of NADW is incorporated into the upper overturning circulation and is returned to lower latitudes (Talley, 2013). The other part of NADW is exposed to negative buoyancy forcing due to atmospheric cooling and brine rejection from sea ice formation and thus transforms into denser Antarctic Bottom Water (AABW), which subsequently sinks to the ocean bottom and spreads into all major ocean basins (Talley, 2013; Lumpkin and Speer, 2007; Ferrari et al., 2014). To maintain mass and buoyancy balances in the global ocean, this high-latitude sinking has to be balanced by diffusive upwelling, enabled by small-scale diapycnal mixing across density surfaces. This basin-scale upwelling was first envisioned by Munk (1966) in his seminal "abyssal recipes" study and was generally assumed to be uniform across the global ocean following Stommel and Arons (1959) (Fig. 1.1).

As more observational profiles on diapycnal mixing became available, it was realized that diapycnal mixing is enhanced towards the ocean bottom (Polzin et al., 1997; St Laurent and Thurnherr, 2007; Ledwell et al., 2000; Waterhouse et al., 2014). In other words, a water parcel becomes denser mixing with denser water below than with lighter water above and thus sinks in the abyssal mixing layers, where this bottom-intensification of mixing occurs. To reconcile this conundrum of diapycnal sinking with basin-scale upwelling, De Lavergne et al. (2016) and Ferrari et al. (2016)

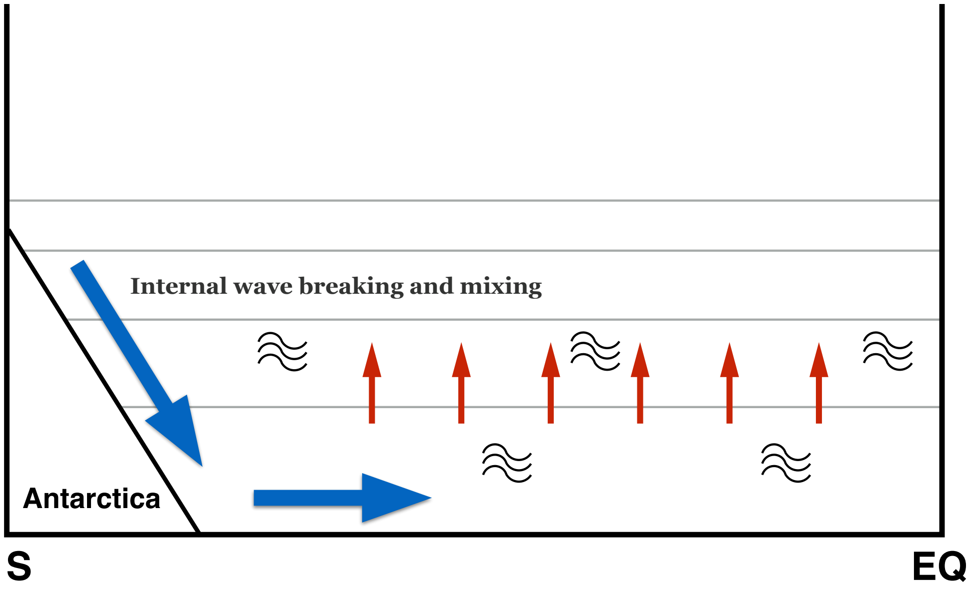

Figure 1.1: Schematic of the classic uniform upwelling of Antarctic Bottom Water (AABW). The thin gray lines denote constant density surfaces. The thick blue arrows represent the sinking and spreading of AABW along the Antarctic margins. The thin red arrows represent the uniform lightening and upwelling of AABW across density surfaces. The squiggly lines are ubiquitous internal wave generation and breaking.

proposed that large-compensating upwelling has to take place near topographic bottom boundary layers (BBL) where buoyancy flux converges (Fig. 1.2). This links the abyssal ocean circulation spanning thousand of kilometers with the BBL whose thickness does not typically exceed several hundreds of meters. Moreover, this large gap in spatial scales has made it more challenging to correctly simulate the abyssal ocean circulation in general circulation models (GCM), casting uncertainties in future climate predictions. This thesis explores small-scale physics within the BBL, and more importantly their connection with the large-scale abyssal overturning circulation and associated water mass transformation (WMT) processes. We will focus on submesoscale dynamics, generally defined with a spatial scale ranging from 1 to 100 km, that are currently not resolved in GCMs.

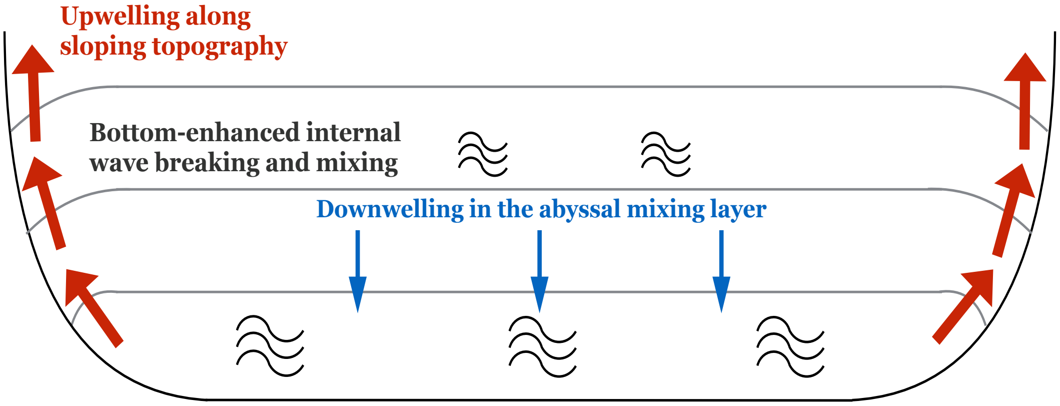

Figure 1.2: Schematic of the upwelling of Antarctic Bottom Water (AABW) along topographic bottom boundary layers (BBL). The thin gray lines denote constant density surfaces. The blue arrows represent the densification and sinking caused by bottom-enhanced diapycnal mixing in the abyssal mixing layer. The red arrows represent the lightening and upwelling of AABW along BBL. The squiggly lines are internal wave generation and breaking which is intensified towards the bottom.

The oceanic BBL is traditionally defined as a thin layer near the seafloor, characterized by enhanced shear and turbulence when external flows are present (e.g. Garrett et al., 1993; Thorpe, 2005; Perlin et al., 2007). In this thesis, we refer to the BBL as a weakly stratified region near the seafloor without a detailed dynamical definition. This should be distinguished from the bottom Ekman layer and the abyssal mixing layer, which are dynamically defined and used in this thesis with subtle differences. The bottom Ekman layer, similar to its surface counterpart, is defined by the veering of the near-bottom flow, as a result of Earth's rotation. Extending several hundreds of meters away from the bottom, the abyssal mixing layer is typically associated with enhanced turbulent dissipation rates and mixing from internal wave breaking, rather than from shear associated with external flows (Callies, 2018).

Besides being the pathways for bottom water upwelling, the BBL has also been considered an important source of drag in the abyssal overturning circulation (Wunsch and Ferrari, 2004). As deep boundary currents and eddying flows pass over the seafloor, they experience strong friction exerted by the solid bottom and thus lose their kinetic energy into heat. The wind stress at the ocean surface has been estimated to input kinetic energy directly into the global geostrophic circulation at a rate of about 1 TW (= 10^{12} W) (Wunsch, 1998). However, it is unknown yet how this kinetic energy input is dissipated in the ocean interior. Several candidates have been proposed, including bottom friction, lee wave generation and breaking, energy extraction by submesoscale instabilities, and surface drag, which is the energy loss from the surface currents interacting with opposing wind stress (Ferrari and Wunsch, 2009). Previous estimates of the global bottom dissipation rate in the BBL have not reached an agreement. In fact, the estimates are vastly different, ranging from negligibly small to as large as 0.83 TW (Wunsch and Ferrari, 2004; Sen et al., 2008; Arbic et al., 2009; Wright et al., 2013).

The goal in this thesis work is twofold. First, we aim to study the submesoscale processes involved in the formation and consumption of AABW, from observations and numerical simulations. Second, we plan to examine the role of the BBL in dissipating the kinetic energy of the abyssal ocean, by proposing theoretical frameworks to diagnose and parameterize the bottom friction experienced by external mean flows near the seafloor.

In Chapter 2, we show how Lower Circumpolar Deep Water (LCDW) can be transformed into lighter water masses due to submesoscale symmetric instability in the BBL over the continental slope. Significant modification of LCDW can occur at intermediate depths due to the interaction of strong boundary currents with sloping topography in the Southern Ocean, as opposed to the prevailing speculation that LCDW is modified predominantly at the ocean surface and is transformed into dense AABW and sinks into the ocean abyss. This new mechanism may short-circuit traditional overturning pathways in the Southern Ocean.

Chapter 2 emphasizes the dynamic importance of submesoscale processes near the BBL in the formation of AABW. In Chapter 3, we focus on the consumption of AABW after it is spread into the ocean basins and is close to the ubiquitous mid-ocean ridge system. The consumption of AABW relies on buoyancy flux convergence as a result of mixing acting on the sustained background stratification near the bottom. Using the MIT general circulation model (Marshall et al., 1997), we explore the mean flow structures driven by the prescribed diapycnal mixing as a function of height above the bottom. At the same time, we demonstrate that the stratification over the mid-ocean ridge flanks and inside the ridge-flank canyons are maintained by two different mechanisms, the former involving the generation of submesoscale baroclinic eddies in abyssal mixing layers and the latter involving a mean up-canyon flow, driven by a baroclinic pressure gradient in the along-canyon direction. From the model results, the total consumption of the AABW in the Brazil Basin in the south Atlantic is around 2 Sv (1 Sv = 10^6 m^3/s), of the same order as previous estimate from observations.

Chapter 3 examines the BBL, specifically the abyssal mixing layers, in permitting effective bottom water consumption. However, external flows associated with boundary currents and mesoscale eddies are common features in the BBL near the seafloor. The resulted Eulerian advection of stratification in the bottom Ekman layer across sloping topography will affect not only the pattern of buoyancy flux convergence and WMT, but also the flows close to the seafloor and thus friction and local kinetic energy dissipation. Chapter 4 thus introduces a new framework to describe the evolution of cross-slope velocity in the bottom Ekman layer when steady downwelling-favorable flows are present. This complements the previous exploration in the abyssal mixing layers in which stratification is only influenced by turbulent buoyancy diffusion. Furthermore, we apply this new framework to parameterizing the evolution of bottom friction based on observable variables, including the bottom mixed layer depth, stratification and topographic slope angle. This will shed light on the estimates of the bottom dissipation rate in the BBL and thus the global kinetic energy budget.

Oceanic boundary currents and eddying flows over sloping topography exhibit variability with a range of time scales and are often characterized by horizontal velocity shears. When the flows near the bottom are not uniform in the horizontal directions, mass transport in the BBL is converging/diverging, resulting in mass injection/suction into and out of the interior. We show in Chapter 5 that, when combined with the potential vorticity (PV) anomalies of the imposed barotropic flow, the induced secondary circulation can give rise to a time-mean, rectified, vertical eddy PV flux into the ocean interior. With simple constant turbulent coefficients, we also provide a preliminary study on the response of the boundary circulation to changes in the oscillation frequency of the mean flow, the background flow amplitude, bottom slope angle, and stratification.

We summarize our main findings in Chapter 6, along with our understanding of the linkage between the abyssal overturning circulation and the BBL dynamics.

Chapter 2

CONTRIBUTION OF TOPOGRAPHICALLY GENERATED SUBMESOSCALE TURBULENCE TO SOUTHERN OCEAN OVERTURNING

Ruan, Xiaozhou et al. (2017). "Contribution of topographically generated submesoscale turbulence to Southern Ocean overturning". In: *Nature Geoscience* 10.11, pp. 840–845. DOI: `10.1038/NGEO3053`.

2.1 Abstract

The ocean's global overturning circulation regulates the transport and storage of heat, carbon and nutrients. Upwelling across the Southern Ocean's Antarctic Circumpolar Current and into the mixed layer, coupled to water mass modification by surface buoyancy forcing, has been highlighted as a key process in the closure of the overturning circulation. Here, using twelve high-resolution hydrographic sections in southern Drake Passage, collected with autonomous ocean gliders, we show that Circumpolar Deep Water originating from the North Atlantic, known as Lower Circumpolar Deep Water, intersects sloping topography in narrow and strong boundary currents. Observations of strong lateral buoyancy gradients, enhanced bottom turbulence, thick bottom mixed layers and modified water masses are consistent with growing evidence that topographically-generated submesoscale flows over continental slopes enhance near-bottom mixing, and that cross-density upwelling occurs preferentially over sloping topography. Interactions between narrow frontal currents and topography occur elsewhere along the path of the Antarctic Circumpolar Current, which leads us to propose that such interactions contribute significantly to the closure of the overturning in the Southern Ocean.

2.2 Southern Ocean overturning pathways

The influence of the Southern Ocean in the global overturning circulation depends on three distinct characteristics of the region: (i) a circumpolar geometry that allows water masses to be exchanged between different basins through the Antarctic Circumpolar Current (ACC); (ii) strongly tilted density surfaces, or isopycnals, that provide an adiabatic pathway for deep water masses towards the ocean surface; and (iii) the exposure of these dense water masses to transformation by surface buoyancy forcing. These features of the ACC are most pertinent to the upper 2000 m, or the region above the sill depth of Drake Passage, and have been prominent in discussions of how deep water masses are modified and returned to near-surface formation sites of deep and bottom waters (Speer et al., 2000; Marshall and Speer, 2012; Sloyan and Rintoul, 2001). Direct surface forcing circumvents the need for an interior diabatic closure of the overturning (Munk, 1966) and can support "adiabatic" overturning cells when isopycnals outcrop at high latitudes in both hemispheres and diapcynal mixing is weak (Wolfe and Cessi, 2011). However, isopycnals that host Lower Circumpolar Deep Water (LCDW) do not outcrop in regions where the surface buoyancy forcing is positive, and therefore cannot be converted, via surface transformation, into the lighter Upper Circumpolar Deep Water (UCDW) or Antarctic Intermediate Water (AAIW) and participate in the upper branch of the overturning circulation (Naveira Garabato et al., 2014). Instead, it has been suggested that LCDW upwells under sea ice and is preferentially incorporated into Antarctic Bottom Water (AABW) and into the lower branch of the overturning circulation (Talley, 2013; Ferrari et al., 2014). Here, we report observational evidence from Drake Passage of a pathway by which a portion of LCDW is modified to become more buoyant, via the generation of submesoscale turbulence over sloping topography that enhances near-bottom mixing. LCDW then enters the upper branch of the overturning without being incorporated into AABW.

Hydrographic sections obtained around Antarctica show UCDW having unfettered access to the continental shelf while LCDW, instead, predominantly intersects, or "incrops", either over the Antarctic continental slope or along one of the major topographic features encountered by the ACC (Orsi and Whitworth III, 2005) (Fig. 2.1). This raises the possibility that the overturning circulation in the Southern Ocean may depend sensitively on diabatic processes at these incrop locations (Ferrari et al., 2016; De Lavergne et al., 2016).

Previous studies have reported subsurface diabatic pathways in the Southern Ocean due to various mechanisms, including interior diapycnal mixing between the upper and lower branch of the overturning (Naveira Garabato et al., 2007), tidal boundary mixing (Silvester et al., 2014), entrainment into sinking plumes (Orsi et al., 2002), and entrainment in the deep ACC through bottom-enhanced wave-breaking (De Lavergne et al., 2016). While the importance of bottom boundary layer processes on mixing has been noted (Armi, 1978; Polzin et al., 2014), the direct closure of the overturning due to these processes has received less attention. Nevertheless, there

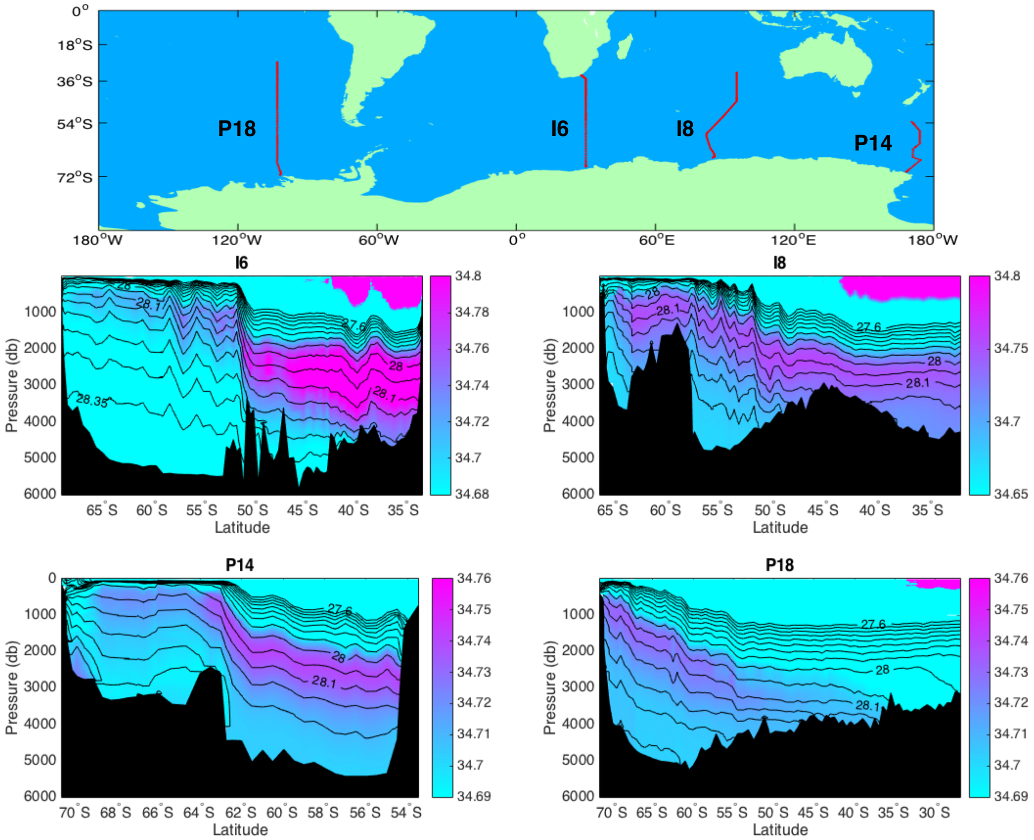

Figure 2.1: Salinity distributions from WOCE transects (summer measurements) I6, I8, P14 and P18 (Orsi and Whitworth III, 2005). The purple colors highlight that Lower Circumpolar Deep Water (characterized by a salinity maximum) incrops on the Antarctic continental slope and deeper topographic features broadly around Antarctica. Neutral density surfaces are indicated as black contours.

is increasing evidence that boundary currents flowing along steep topography may catalyze strong turbulent mixing due to the generation of submesoscale motions (Molemaker et al., 2015; Gula et al., 2016); bottom boundary layers (BBLs) may even be the principal location for the overturning's diabatic upwelling (De Lavergne et al., 2016; Ferrari et al., 2016). Here we use observations in a region where the southern boundary of the ACC (Bdy) (Orsi et al., 1995) runs along the continental slope of the Antarctic Peninsula to show that the interaction between strong frontal currents and sloping bathymetry can lead to modification of LCDW into lighter waters.

2.3 Drake Passage glider observations

In austral summer 2014-15, a high-resolution survey of the hydrographic and biogeochemical properties of the Drake Passage continental shelf and slope, located north of the Antarctic Peninsula's tip (Fig. 2.2a), was completed using a pair of autonomous ocean gliders; these measurements were complemented with two ship-based hydrographic sections (Fig. 2.2b). The gliders were deployed between 5 December, 2014 and 8 April, 2015 to measure temperature, salinity, dissolved oxygen, fluorescence and optical backscatter (see appendix for data processing). Each glider dive described a V-shaped pattern with a surface spacing between 1 and 5 km, depending on water depth and currents, and a vertical resolution of ~1 m. The glider survey was designed to complete multiple cross-slope sections and to sample to the seafloor or to 1000 m, whichever was shallower (see appendix). We focus here on observations collected from the glider deployed west of the Shackleton Fracture Zone (SFZ). This study region is characterized by a steep continental slope that hosts the ACC's eastward-flowing Bdy along the ~2000 m isobath, as well as a westward-flowing frontal current over the shelf break, typically found at 500 m in this region.

2.4 Hydrographic and hydrodynamic information

The Bdy is defined as the southern limit of UCDW, the warmest water mass found around Antarctica (Orsi et al., 1995). The interaction of the Bdy and the continental slope produces a sharp front, where changes in temperature greater than 2°C over a distance of only 10 km are common. In this region, the Bdy is also characterized by many intrusive features (Fig. 2.2c), indicating a vigorous exchange between shelf water and offshore Circumpolar Deep Water (CDW). In Drake Passage, the core of UCDW has a neutral density $\gamma^n = 27.95$ kg m^{-3}, which connects, along isopycnals, to colder and fresher waters over the continental shelf (Fig. 2.2c,d). Below the UCDW temperature maximum, LCDW, identified by a maximum in salinity, incrops on the continental slope.

At the Antarctic margins, slope boundary currents typically exhibit up to 20 cm s^{-1} mean speeds (Gill, 1973). The channeling of the ACC into the narrow Drake Passage elevates the near-bottom eastward flow to velocities greater than ~30 cm s^{-1} (Fig. 2.3a). The strong and narrow boundary current produces large Rossby numbers (~0.5) at subsurface levels, where the Rossby number is defined by the ratio of the vertical component of the relative vorticity ζ to the Coriolis frequency f (see Methods for discussion of vorticity calculation with the gliders).

The front is also characterized by a weak vertical stratification, defined by the buoyancy frequency $N^2 = \partial_z b$, an enhancement of the vertical shear $\partial u/\partial z$, and

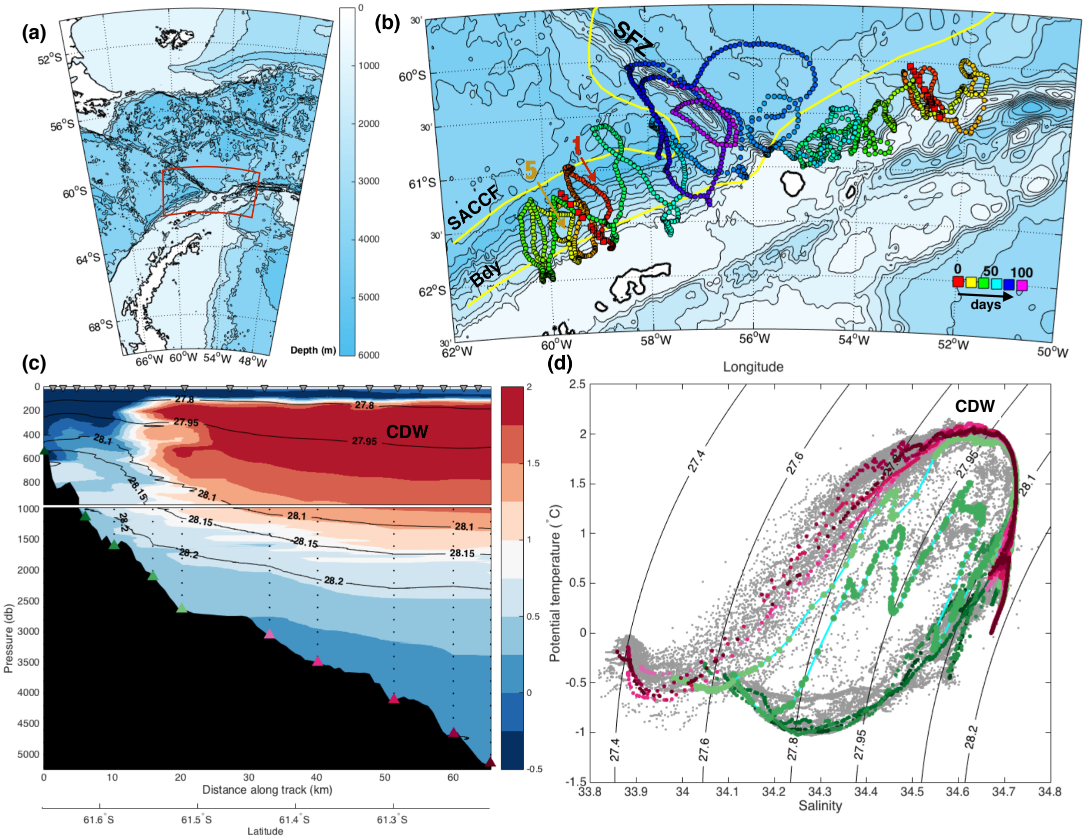

Figure 2.2: Overview of the ChinStrAP (Changes in Stratification at the Antarctic Peninsula) field program. (a) Location of the study site and bathymetry (color, in meters). (b) Enlarged map of the red box in panel (a) with glider sampling locations colored by sampling date (in days, from December 5, 2014). Glider transects 1 (red) and 5 (yellow) are indicated with a bold number. Ship-based CTD transects are indicated with red squares. This study focuses on the region west of the Shackleton Fracture Zone (SFZ). Climatological frontal positions of the Southern ACC Front (SACCF) and the ACC's southern boundary (Bdy) (Orsi et al., 1995) are shown as yellow contours. (c) Potential temperature composite section obtained from glider Transect 1 (surface to 1000 m) and from the western CTD section (1000 m to bottom) overlaid with neutral density (kg m^{-3}) in black contours. Bottom triangles and vertical dotted lines indicate the position of CTD casts. Surface triangles indicate glider surface positions. (d) Potential temperature/salinity (Θ/S) diagram from full-depth CTD stations colored by geographical location as in panel (c). Glider measurements from Transect 1 are shown as gray dots. Isolines of neutral density (kg m^{-3}) are given by the black curve.

an enhancement of the lateral buoyancy gradient $M^2 = \partial_y b$ (Fig. 2.3c), where $b = -g\left(\rho - \rho_0\right)/\rho_0$ is the buoyancy and ρ_0 is a reference density. The weak stratification and high shear reduce the Richardson number $Ri = N^2/(\partial_z u)^2$ (Fig.

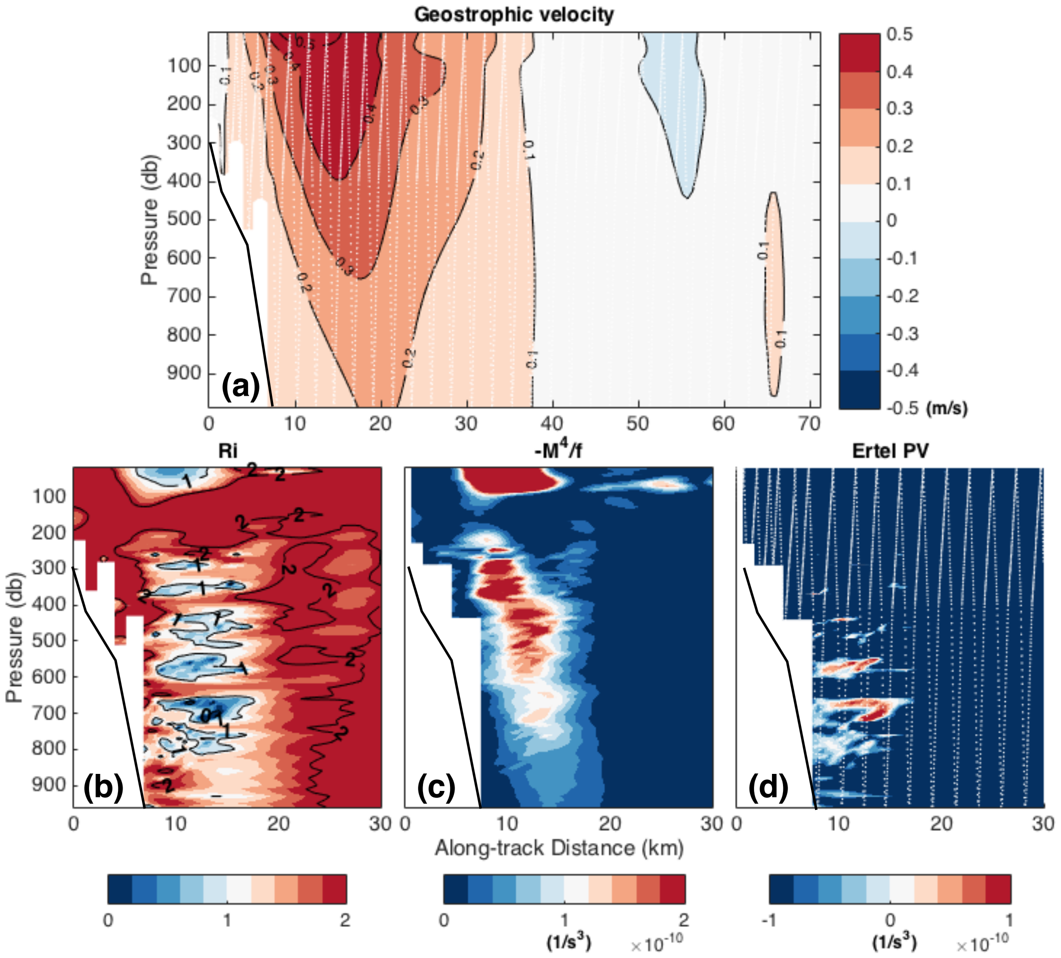

Figure 2.3: Stratification and flow characteristics from a typical glider section (transect 5 in Fig.2.2). (a) Geostrophic velocity (m s^{-1}) referenced to the depth-averaged current from the glider (eastward, positive). (b) Logarithm of the Richardson number, $Ri = N^2/u_z^2$ (in color, e.g. 1 corresponds to 10^1). (c) Lateral buoyancy gradient, plotted as M^4/f (s^{-3}), where $M^2 = \partial_y b$, b is buoyancy and f is the Coriolis frequency. (d) Ertel potential vorticity (s^{-3}), defined in Methods. The white dotted curve in panels (a) and (d) indicates the glider path.

2.3b). Large values of Ri are indicative of regimes where stratification can suppress the growth of shear instabilities. While $Ri < 0.25$ is the typical criteria to overcome this suppression, regions of low Ri indicate locations where vertical mixing may be active (i.e., $Ri < 10$ in Fig. 2.3b).

Information related to horizontal and vertical gradients in the velocity and buoyancy fields can be encapsulated in a single diagnostic, the Ertel potential vorticity (PV, defined in Methods), which is a materially-conserved property that can be used to identify and classify flow regimes susceptible to hydrodynamic instabilities. We approximate the PV using cross-slope gradients only. Where PV takes the opposite sign of f, which for the Southern Ocean is where PV>0, the flow will be unstable and generate mixing that will return the PV to neutral stability, or PV= 0. The vertical stratification fN^2, relative vorticity ζN^2, and baroclinic $-M^4/f$ terms all make leading-order contributions to the PV. A weak vertical stratification N^2 and strong lateral stratification M^2 leads to positive PV values in discrete, thin, $O(10)$ m, layers over the continental slope (Fig. 2.3d); these layers are collocated with the intrusive features at the CDW-shelf boundary (Fig. 2.2c). The positive PV regions are found on the cyclonic side of the boundary current (shoreward), where $|M^4/f| > |fN^2|$, suggesting that the flow instability type is symmetric (Thomas et al., 2013). The positive PV values are likely signatures of strong BBL mixing that are exported along isopycnals to the ocean interior, in agreement with recent numerical simulations (Gula et al., 2016).

2.5 Bottom mixed layers and water mass modification

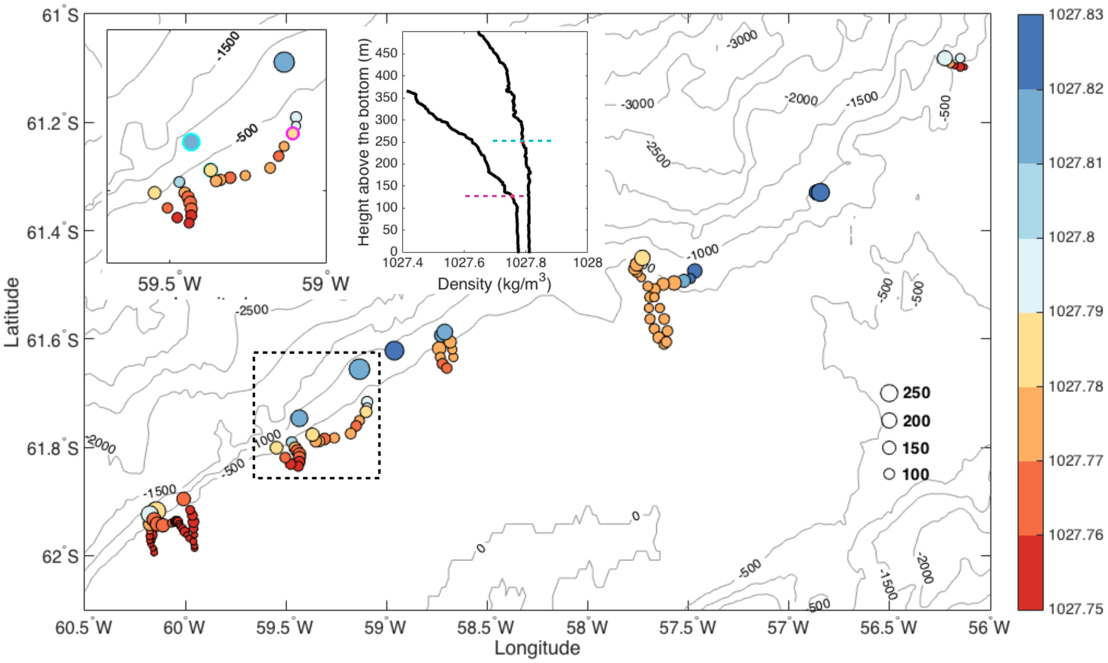

Figure 2.4: Bottom mixed layer (BML) properties over continental shelf and slope. Glider dive locations are indicated as circles colored by the bottom-most density value (kg m^{-3}) and sized by the BML thickness. Details from the dashed box are shown in the upper left inset, and two example near-bottom density profiles (highlighted in cyan and magenta) are shown in the upper right inset. Horizontal dashed lines denote the top of the BML using the Δ 0.02 kg m^{-3} criterion.

Additional evidence of strong bottom mixing comes from the large bottom mixed layer (BML) thickness observed by the gliders across all transects (Fig. 2.4). Typical BML thickness approaches 40 m for most of the North Atlantic basin (Lozovatsky et al., 2008). In contrast, along the southern boundary of Drake Passage, BML thickness, defined with a Δ 0.02 kg m^{-3} density threshold from the bottom, is typically 100 m or larger (Fig. 2.5) over the continental shelf and slope. This BML thickness is similar to recent observations within the Gulf Stream over topographic features (Todd, 2017), and complement the *Ri* calculations, which typically show the lowest values just off the shelf break. Moving offshore, the BML becomes thicker and denser (Fig. 2.4). The hydrographic, velocity and potential vorticity fields, as well as the deep BML observations, all provide evidence of vigorous mixing over the continental slope. However, diabatic transfer, or water mass modification, is required to provide a closure mechanism for the LCDW circulation in the overturning.

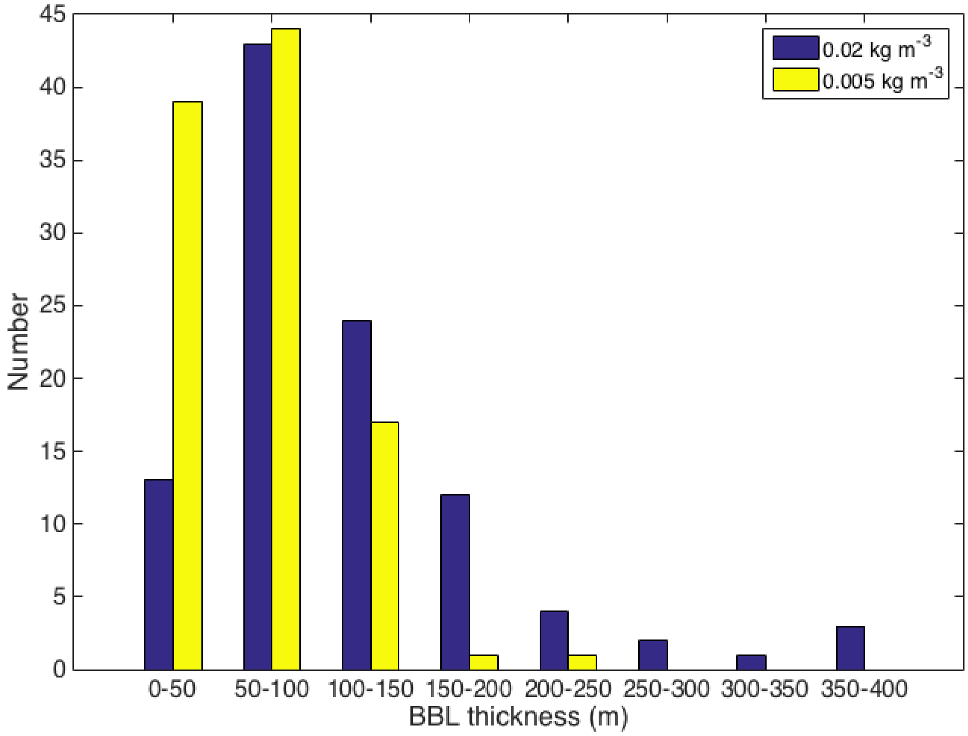

Figure 2.5: Statistics of bottom mixed layer (BML) thickness (m) based on a Δ 0.02 kg m^{-3} threshold (blue) and a Δ 0.005 kg m^{-3} threshold (yellow).

For the twelve transects collected by our gliders, there are distinct differences between water mass properties when the CDW core is located near the shelf break or further offshore. In particular, when the Bdy is close to the shelf break, positive PV values are more common and water masses that are a mixture of LCDW and shelf waters occur (Fig. 2.6a,b). In contrast, when the CDW core is located offshore, shelf and off-shelf waters are well separated (Fig. 2.7) and modified water masses are absent. The modification is aided by the strong near-bottom eastward flow of the Bdy that produces an onshore (and convergent) bottom Ekman transport that brings deeper density classes up the slope (Phillips et al., 1986; Garrett et al., 1993). Additionally, tidal mixing contributes to water mass modification. At ebb, CDW is pulled onshore, over the upper slope, leading to strong mixing near the bottom. At flood, modified waters are injected offshore, leading to additional mixing in lighter density classes (Flexas et al., 2015).

Here, the source of lighter water comes from the continental shelf leading to a lightening of LCDW, but similar submesoscale processes happening elsewhere in the ACC could cause LCDW to become denser depending on the configuration of the density surfaces incropping on topography. Modification of LCDW in the BBL over topography provides a potential pathway that "connects" the overturning's upper and lower branches away from the ocean surface. This process is distinct from the entrainment of LCDW into bottom water plumes that occurs over the continental slope in the subpolar gyres (Orsi et al., 2002).

Quantifying the contribution of the proposed submesoscale mechanism to the overturning requires an estimate of the water mass transformation rate, ideally derived from direct turbulent dissipation measurements. In their absence, we turn to well-tested parameterizations of dissipation due to shear-induced mixing (see appendix), which will necessarily be an underestimate, since other mixing processes, e.g. symmetric instability, are not included. Assuming the leading order balance in the BML is between shear production and dissipation, and that shear production can be estimated from the velocity profiles, we estimate that the local dissipation rate in the BML is of order 10^{-7} W kg^{-1}. This dissipation rate agrees with direct microstructure observations near Elephant Island (Silvester et al., 2014) (~61°S, 54.5°W); these latter measurements may even exceed our glider estimates over short time periods. These values are considerably larger than Southern Ocean background dissipation values, which are typically between 10^{-10} and 10^{-9} W kg^{-1}. Based on these dissipation values, water mass transformation rates, both locally and integrated over the path of the ACC, are estimated in the Supplementary Material. Our extrapolation to the entire Southern Ocean is poorly constrained, but provides transformation values, between 1 and 5 Sv (1 Sv = 10^6 m^3 s^{-1}), that warrant further exploration.

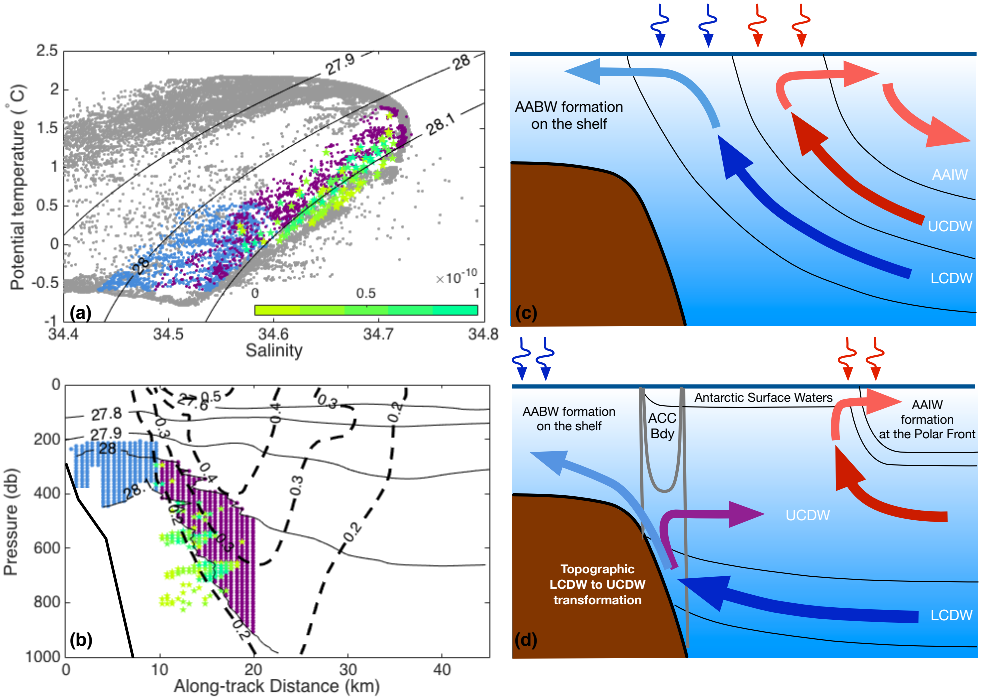

Figure 2.6: Water mass transformation over the continental slope and schematics of the upper overturning closure in the Southern Ocean. (a) Potential temperature-salinity (Θ/S) diagram from Transect 5 (Fig. 2.2b), where offshore and shelf waters are well-mixed. Neutral density surfaces are shown as black contours. The bottom-most water mass ($\gamma^n > 28.1$ kg m^{-3}) becomes lighter due to mixing, filling in the region between the 28 and 28.1 neutral density contours. Two families of modified waters (blue and purple) are found. Green stars show those locations in Θ/S space that correspond to $PV > 0$ values, indicating strong mixing. (b) Glider Transect 5 showing the position of the blue, purple, and green dots defined in (a). Neutral density surfaces are shown as black contours. Referenced geostrophic velocity (m s^{-1}, as in Fig. 2.3a) are shown as dashed contours. One family of the modified water is found near the continental shelf and the other family is exported offshore from the mixing region along isopcynals. (c) Traditional Southern Ocean overturning schematic where both UCDW and LCDW outcrop at the surface along adiabatic pathways and are modified by surface buoyancy forcing after turbulent entrainment into the mixed layer (red and blue squiggly arrows indicate positive and negative surface buoyancy fluxes). Upwelling into a region of negative buoyancy forcing leads to Antarctic Bottom Water (AABW) formation and upwelling into a region of positive buoyancy forcing leads to Antarctic Intermediate Water (AAIW) formation. (d) Modified schematic where LCDW principally incrops on the continental slope or other topography. The generation of strong mixing due to flow-topography interactions transforms LCDW into lighter waters. Adiabatic pathways to AABW or AAIW formations sites, over the shelf or at the surface respectively, are available in UCDW density classes.

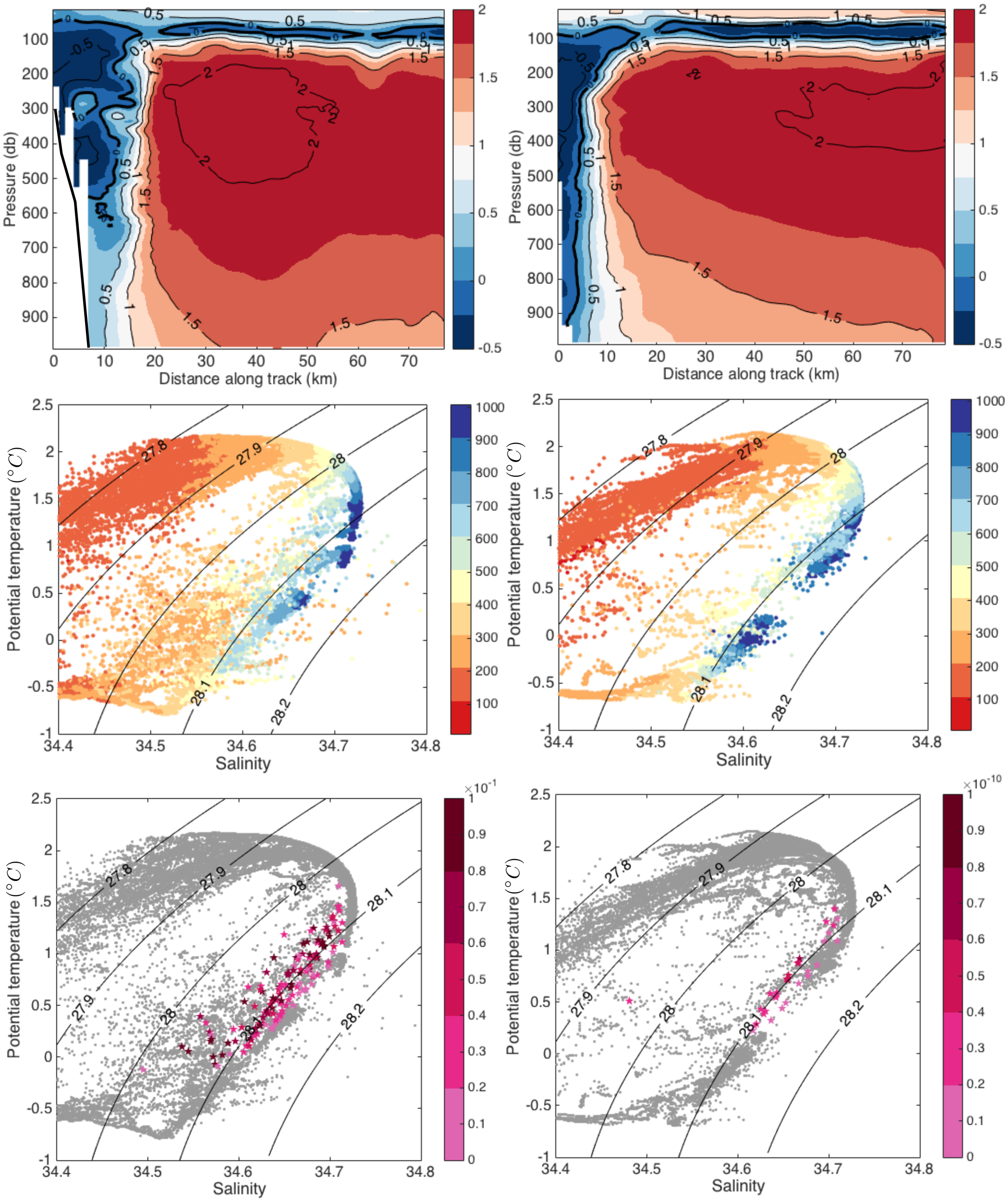

Figure 2.7: Two transect examples of CDW being close to (left panels; Transect 5) and away from (right panels; Transect 8) the slope. (Upper panels) Potential temperature sections. Isothermals are labeled every 0.5°C. The 2°C contour roughly defines the location of the Bdy. The 0°C isotherm (in bold black) marks the front separating warm CDW from cold shelf water. (Middle panels) Θ/S diagram of glider data colored by depth (in meters). (Lower panels) Positive Ertel PV (in magenta) over all data sampled for each given transect (in gray).

In light of our findings, we propose an additional pathway to close the overturning circulation and transform CDW over sloping topography along the path of the ACC (Fig. 2.6c,d). Strong frontal currents are found uniformly around Antarctica, and models indicate that flow-topography interactions can generate submesoscale motions (Rosso et al., 2015). Due to its unique characteristics, Drake Passage possibly favors the strongest mixing of LCDW and shelf waters, making this site disproportionately significant in closing the overturning circulation. Nevertheless, the propensity for LCDW to incrop on continental slopes (Fig. 2.1) and for deep-reaching ACC currents to intersect topography in the Southern Ocean (Fig. 2.8) suggests that BBL mixing due to submesoscale turbulence may contribute significantly to the modification of LCDW. This study suggests that the relationship between the incropping of density classes on sloping topography and the location of swift ACC boundary currents may be as critical as surface outcropping for understanding the overturning closure. Intricate patterns of deep water mass modification must be considered in efforts to map the traditional two-dimensional Southern Ocean residual overturning (Marshall and Radko, 2003; Marshall and Speer, 2012) to more realistic three-dimensional overturning pathways (Talley, 2013; Thompson et al., 2016; Naveira Garabato et al., 2014; Tamsitt et al., 2017) and their changes across different climate regimes (Ferrari et al., 2014).

2.6 Appendix A: Methods

Glider measurements

An ocean glider is a buoyancy-driven, autonomous underwater vehicle. As part of the ChinStrAP (Changes in Stratification at the Antarctic Peninsula) project, two ocean gliders (SG566 and SG539) were deployed from the *ARSV Laurence Gould* in southern Drake Passage between 5 December, 2014 and 8 April, 2015. Equipped with a Seabird SBE3 temperature sensor and a SBE4 conductivity sensor, an Aanderaa 4330F oxygen optode, and a WET Labs ECO Puck sensor, the gliders collected vertical profiles of temperature and salinity, dissolved oxygen, optical backscatter and fluorescence west and east of the Shackleton Fracture Zone (SFZ). Each glider carried an altimeter which actively detects the bottom, allowing the glider to turn around once the bottom is seen. In total, the gliders completed over 1400 dives, to a maximum depth of 1000 m or to a certain distance within the seafloor (normally between 20 and 30 m) in shallow water depending on an adjustable parameter for each dive. During part of the field project, the altimeter on SG566 (west of the SFZ) did not function properly, which caused the glider to

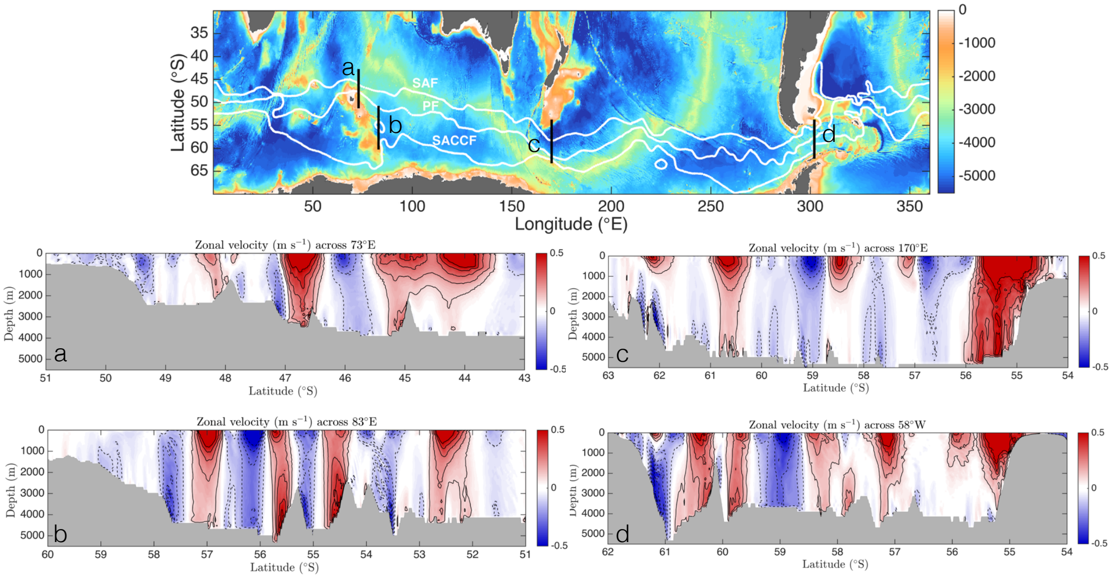

Figure 2.8: Zonal velocity snapshots across topographic features in the Southern Ocean from a high-resolution numerical model (See model introduction in Supplementary Material). Transects a, b, c and d correspond to Northern and Southern Kerguelen Plateau, Campbell Plateau (including the Macquarie Ridge) and Drake Passage. White contours in the upper panel are the climatological frontal positions in the Southern Ocean (Orsi *et al.* 1995) and black straight lines correspond to the transects from which zonal velocity snapshots are shown below. Black contours in the lower four panels are zonal velocities (eastward, positive, solid lines). Contour levels are from 0.1m/s to 0.5m/s with a 0.1m/s interval. Deep-reaching fast boundary currents (some with bottom velocity intensification) interacting with sloping topography can be seen widely in the Southern Ocean across the chosen major topographic features.

come to rest on the seafloor. Measurements of salinity are valid when the glider is moving at speeds in excess of 10 cm s^{-1}, but not when the glider is at rest.

The gliders complete each V-shaped dive approximately every four hours for 1000 m dives, or for shorter periods for shallower dives. The gliders collected a measurement every 5 s, or approximately every 0.5 m in the upper water column, and every 10 s (or 1 m) in the lower water column. The sampling resolution changed at either 300 m or 400 m during the mission. The V-shaped profiles were optimally interpolated onto regular grids with a vertical resolution of 5 m and a horizontal resolution of 0.6 km; interpolation scales were 15 m and 5 km in vertical and horizontal directions, respectively. The raw measurements of temperature and salinity are shown in all the Θ/S diagrams, and the geostrophic velocity, Richardson number and PV values are calculated based on the interpolated dataset. The geostrophic shear is obtained after applying a moving-average window to the density field with a width of twice the local deformation radius (i.e., ~5 km). The interpolated and filtered glider data produce good agreement with ship-based CTD measurements (Fig. 2.2c,d) on the property distribution and boundary current location and speed. The barotropic, or depth-averaged component of the velocity, is calculated directly from the gliders using both the glider surfacing positions in each dive and a glider flight model which assumes no background mean flow.

The Ertel PV is defined as:

$$Q_{\text{Ertel}} = (f\hat{\mathbf{k}} + \nabla \times \mathbf{u}) \cdot \nabla b \tag{2.1}$$

where $\nabla \times \mathbf{u}$ and b are, respectively, the relative vorticity and buoyancy (defined in the main text). Vertical velocities are assumed small and neglected. Geostrophic balance is assumed, and thus, the thermal wind balance (relating vertical shear of the horizontal velocities and horizontal buoyancy gradients) holds and can be used to simplify the term arising from lateral gradients in buoyancy, $(v_z, u_z) \cdot (b_x, b_y) = |\nabla_h b|^2 / f = M^4/f$, where ∇_h denotes the horizontal gradient. It is assumed that the cross-front variations are larger than the along-front variations throughout this paper. Thus the approximated PV calculated in this study can be written as:

$$Q_{\text{glider}} \approx (f - u_y)N^2 - M^4 f^{-1} \tag{2.2}$$

where the subscript y is the cross-front direction and it increases offshore; $M^2 = \partial_y b$ is defined as the cross-front buoyancy gradient.

Estimate of the kinetic energy dissipation rate

Assuming the leading order balance in the bottom mixed layer is between shear production and dissipation,

$$u_* = \left(\frac{\epsilon}{\frac{\partial u}{\partial z}} \right)^{1/2}, \tag{2.3}$$

where u_* is the friction velocity in the bottom mixed layer and ϵ is the turbulent kinetic energy dissipation rate. The friction velocity may be parameterized (Thorpe, 2005) as

$$u_* \approx \left(5 \times 10^{-2}\right) U_\infty, \tag{2.4}$$

where U_∞ is the background mean current velocity. Using typical values from the ChinStrAP study, $\frac{\partial u}{\partial z} \approx 3 \times 10^{-4}$ s^{-1} and $U_\infty \approx 0.3$ m s^{-1}, the inferred dissipation rate ϵ is of order 10^{-7} W kg^{-1}. Note that this is entirely based on shear-driven mixing and symmetric instability-induced dissipation is not accounted for in the estimate, thus this inferred value is likely an underestimate of the actual dissipation rates.

2.7 Appendix B: Estimates for water mass transformation rates

The water mass transformation rate can be expressed, following Marshall et al. (1999), using a diapycnal velocity $\tilde{\mathbf{e}}$, as

$$T = -\int\int_A \tilde{\mathbf{e}} \cdot \mathbf{n}_b \, dA = \int\int_A \frac{\nabla \cdot \mathbf{F}_b}{|\nabla b|} dA. \tag{2.5}$$

Here $b = -g\left(\rho - \rho_0\right)/\rho_0$ is the buoyancy and ρ_0 is a reference density, A is the area of a buoyancy surface across which the diapycnal transport is measured, $\mathbf{n}_b$ is the unit vector normal to the isopycnal and $\mathbf{F}_b$ is the turbulent buoyancy flux. It has been argued that the vertical buoyancy flux scales with the dissipation rate as $\Gamma\epsilon$, where Γ is the mixing efficiency (Osborn, 1980). Thus, the buoyancy flux divergence can be estimated as $\Gamma\epsilon/h$ where h is the thickness of the bottom mixed layer (BML); this assumes that the buoyancy flux vanishes at the solid bottom. Using a mixing efficiency $\Gamma = 0.2$, a typical bottom mixed layer thickness $h = 100$ m and a local vertical stratification $N^2 = \frac{\partial b}{\partial z} = 10^{-6}s^{-2}$, the diapycnal velocity can be estimated as 2×10^{-4} m s^{-1}, or ~20 m day^{-1}. Considering a 5 km-wide boundary current (associated with the southern boundary of the ACC) that flows along the continental slope for a distance of 500 km in southern Drake Passage (Fig. 2.8; Orsi et al. (1995)), A is 2.5×10^9 m^2. Using equation (5), this yields a local water mass transformation rate of 0.5 Sv. We acknowledge that the mixing efficiency, Γ, is uncertain in this area, nevertheless, this likely remains an underestimate since only the shear-induced mechanism is accounted for here.

The use of the vertical buoyancy gradient N^2 assumes that the diapycnal mixing and associated water mass modification is a local, one-dimensional (vertical) process, which relies on the rapid export of modified water into the interior. McDougall and Ferrari (2017) hypothesize that water masses may be modified and upwell in boundary layers over sloping topography. In this case, N^2 should be replaced by the lateral buoyancy gradient across the continental slope. Estimating this value across multiple glider sections gives a value of roughly 5×10^{-8} s^{-2} (Fig. 2.2c). This smaller buoyancy gradient suggests a local diapycnal velocity 20 times larger than the previous estimate using the vertical buoyancy gradient. We note that the lateral buoyancy gradient is a more challenging quantity to estimate, especially if the incropping of density surfaces is heterogeneous along the slope (see, for instance, Fig. 4 in Thompson and Heywood (2008)). Now we estimate the area of relevant buoyancy surfaces A within the BML using the BML thickness of 100 m and a longitudinal distance of 500 km along Southern Drake Passage which yields $A = 5 \times 10^7$ m^2. The water mass transformation rate can be thus estimated to be 0.2 Sv. It is important to note that, according to the hypothesis, the excessive (upwelling) diapycnal volume flux along the bottom boundary layers has to be largely compensated by diapycnal downwelling in the stratified mixed layers globally. While the estimates above are associated with some uncertainty, they are sufficiently large to warrant further investigation.

2.8 Appendix C: Extrapolation to the circumpolar Southern Ocean using numerical model output

In order to estimate the circumpolar relevance of the proposed mechanism, we turn to output from a high-resolution global numerical model to examine the interactions between ACC fronts and major topographic features in the Southern Ocean.

LLC4320 is a global ocean and sea ice simulation that represents full-depth ocean processes. The simulation is based on a Latitude/Longitude/polar-Cap (LLC) configuration of the MIT general circulation model (MITgcm; Marshall et al. (1997); Hill et al. (2007)). The LLC grid has 13 square tiles with 4320 grid points on each side (hereafter called LLC4320) and 90 vertical levels for a total grid count of 2:21010. Horizontal grid spacing ranges from 0.75 km near Antarctica to 2.2 km at the Equator and verticalet levels have 1-m thickness near the surface to better resolve the diurnal cycle. The simulation is initialized from a data-constrained global ocean and sea ice solution provided by the Estimating the Circulation and Climate of the Ocean, Phase II (ECCO2) project (Menemenlis et al. (2005); Menemenlis et al. (2008); Losch et al. (2010)), and includes atmospheric pressure and tidal forcing. The inclusion of tides allows for successful reproduction of shelf-slope dynamics and water mass modification (Flexas et al., 2015). Surface boundary conditions are from the European Center for Medium-Range Weather Forecasts (ECMWF) atmospheric operational model analysis, starting in 2011. The sections shown in Fig. 2.8 correspond to a snapshot of LLC4320 on 29/11/2011.

Assuming that there are strong interactions between deep-reaching ACC currents and sloping bottom topography near the Kerguelen Plateau, Campbell Plateau, Drake Passage and ridges and fracture zones in the South Pacific and Atlantic, as seen in Fig. 2.8, then a conservative estimate for A in equation (5) would be 2.5×10^{10}

m^2 (an average of 5km-wide narrow front is assumed). This area estimation would yield a global transformation of LCDW of 5 Sv for the local vertical process. For the along-bottom diapycnal upwelling framework, we estimate the area A to be 5×10^8 m^2 which yields a transformation rate of 2 Sv (with the possible compensating downwelling neglected).

Chapter 3

MIXING-DRIVEN MEAN FLOWS AND SUBMESOSCALE EDDIES OVER MID-OCEAN RIDGE FLANKS AND FRACTURE ZONE CANYONS

3.1 Abstract

To close the abyssal meridional overturning circulation, dense bottom water has to become lighter and upwell by mixing with lighter water above. The classic uniform upwelling view has been challenged, as accumulating observations show that small-scale diapycnal mixing is non-uniform in both the horizontal and vertical direction. Diapycnal mixing has been found to be srongly bottom-enhanced over rough topography, particularly over mid-ocean ridge systems that span thousands of kilometers in the global ocean. This study explores the circulation driven by bottom-intensified mixing over mid-ocean ridge flanks and within ridge-flank canyons, and it examines how stratification is maintained to sustain diapycnal transformation. The stratification over the ridge flanks and inside the ridge-flank canyons is shown to be maintained by two different mechanisms, the former involving the generation of submesoscale baroclinic eddies in abyssal mixing layers and the latter involving a mean up-canyon flow, driven by a baroclinic pressure gradient in the along-canyon direction. Finally, the contributions to deep water mass transformation from the different components of the mid-ocean ridge system are discussed.

3.2 Introduction

Storing and exchanging with the atmosphere vast amounts of carbon and heat, the abyssal ocean is thought to regulate Earth's climate on centennial to millennial timescales (Sarmiento and Toggweiler, 1984; Primeau and Holzer, 2006). In the present abyssal circulation, bottom waters are formed around Antarctica, sink to the ocean bottom, and spread into all ocean basins (Lumpkin and Speer, 2007; Talley, 2013). The high-latitude sinking must be balanced by upwelling across density surfaces, which is enabled by small-scale turbulence that mixes the dense bottom water with the lighter water above (Ferrari, 2014; MacKinnon et al., 2017).

Over the past two decades, it has become increasingly clear that the small-scale turbulence that allows flow across density surfaces is highly non-uniform, implying that the pathways of Antarctic Bottom Water (AABW) back toward the surface are more complicated than the uniform upwelling originally envisioned by Stommel and Arons (1959). Where tidal and subinertial flows pass over a rough sea floor, turbulence is strongly enhanced in abyssal mixing layers that span the bottom few hundred meters of the water column (Polzin et al., 1997; Ledwell et al., 2000; Waterhouse et al., 2014). Given the observed stratification, this bottom-intensification of mixing implies a dipole of diapycnal velocities: downwelling where turbulent buoyancy fluxes increase toward the bottom and upwelling where buoyancy fluxes converge, within tens of meters of the sea floor. This suggests that the net diapycnal upwelling of AABW is a small residual of much larger but compensating transports across density surfaces (Ferrari et al., 2016; De Lavergne et al., 2016). The up- and downwelling dipole on the slopes of large-scale topographic features has been argued to also shape the horizontal circulation of the abyssal ocean (Callies and Ferrari, 2018; Holmes et al., 2019).

For small-scale turbulence to drive a diapycnal circulation, however, it must occur in stratified waters. Callies (2018) argued that bottom-intensified mixing on a large-scale slope quickly erodes the stratification of abyssal mixing layers if left unopposed. The mean flows up and down the slope that develop in response to the mixing are too weak to maintain realistic stratification. But the mixing generates potential energy and powers submesoscale baroclinic eddies, whose buoyancy fluxes restratify abyssal mixing layers. A realistically strong stratification can be maintained by a balance between the homogenizing effect of the mixing and the restratifying effect of submesoscale eddies.

We here study the circulation driven by bottom-intensified mixing in geometries more realistic than those considered previously and ask whether stratification can be maintained by other mechanisms. Callies (2018) investigated the dynamics on an infinitely extending planar slope, employing a setup similar to that used in the study of boundary layers of a rotating stratified fluid adjacent to a sloping boundary (Phillips, 1970; Wunsch, 1970; Garrett, 1991). That setup precludes any effects arising from changes in the topographic slope on both large and small scales.

The geometry that we consider in this study is meant to represent a meridionally oriented mid-ocean ridge. The ridge (Fig. 3.1a) has large-scale variations of its topographic slope in the longitudinal direction. Including such large-scale variations can result in longitudinal variations in the mixing-driven flow, driving mass convergence or divergence and thus so-called tertiary circulation (Garrett, 1991; Dell, 2013). Whether this affects the stratification and its maintenance in the face of bottom-intensified mixing is unclear and will be investigated in this study.

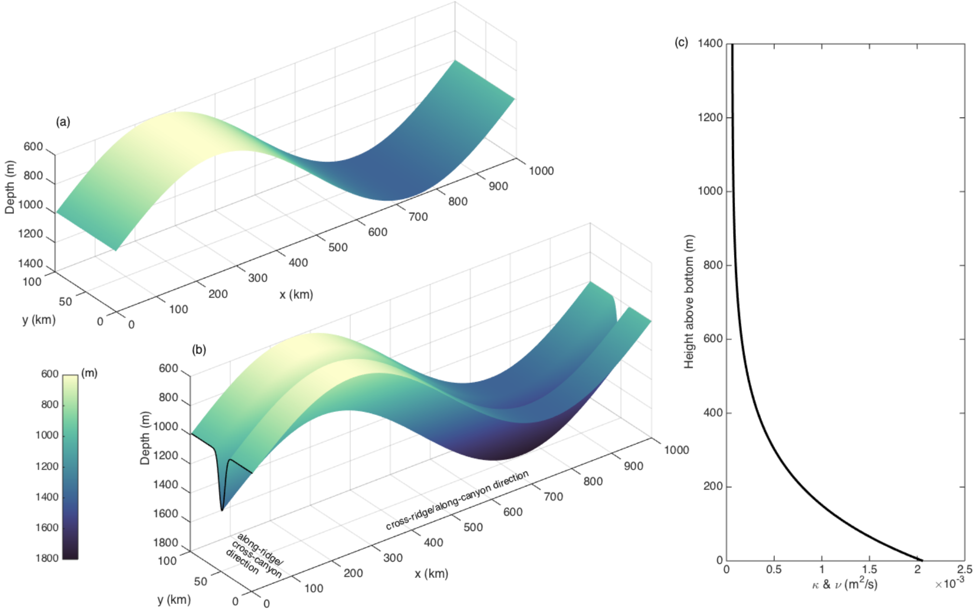

Figure 3.1: Topography and diffusivity/viscosity profiles used in the model simulations. (a) Model topography for the three-dimensional simulation without a canyon. (b) Model topography for the three-dimensional simulation with canyon. (c) Diffusivity and viscosity profile as a function of height above the bottom. Not the stretching of the along-ridge coordinate y relative to the cross-ridge coordinate x.

Moreover, over the flanks of the mid-ocean ridges, there are ubiquitous deep canyons cutting across the ridge flank and crest (see Fig. 3.2 for an example in the South Atlantic). Not shown in the figures are even smaller scale ($1-10\,\text{km}$) anisotropic abyssal hills that are perpendicular to the ridge flank canyons. Previous observations have revealed a strong (greater than $1\,\text{cm}\,\text{s}^{-1}$) up-canyon mean flow inside a particularly deep canyon (Thurnherr et al., 2005). The observed up-canyon mean flow is much greater than predicted by one-dimensional theory on a planar slope (Callies, 2018). Dell (2013) suggested that the up-canyon flow is due to both the baroclinic pressure gradient across the slope and the blocking of an along-ridge flow by the canyon walls, but she considered an infinitely deep canyon that might exaggerate these effects. A primary goal of this study is to examine how canyons running across a ridge flank affect mean flows and whether these mean flows are strong enough to maintain stratification without the need for restratification by submesoscale eddies.

Motivated by a relative wealth of observations, we consider idealized geometries and mixing coefficients inspired by the Brazil Basin in the South Atlantic, where an

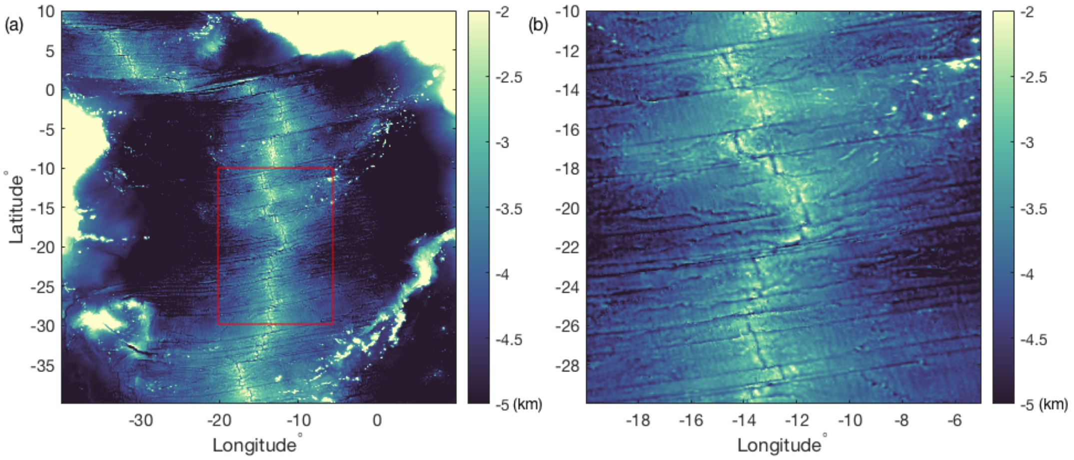

Figure 3.2: The Mid-Atlantic Ridge bathymetry and ridge flank canyons. (a) Bathymetry in the South Atlantic from the Smith and Sandwell dataset (Smith and Sandwell, 1997). (b) Zoom-in to the red rectangle, showing the fracture zone canyon bathymetry on the ridge flanks. Note that this dataset resolves abyssal hills only in a few locations, where multi-beam data are available.

estimated 4 Sv (Sverdrup, 10^6 m^3 s^{-1}) of AABW is consumed (Hogg et al., 1982). We note that the processes considered here do not only apply to the Brazil Basin but can be extended to the global ocean, as mid-ocean ridge systems with ridge-flank canyons are ubiquitous features around the globe. The Brazil Basin is bounded by the relatively smooth abyssal plains and the South American continental margin on the west and the rough Mid-Atlantic Ridge system on the east (Fig. 3.2). During several microstructure surveys, bottom-enhanced mixing has been found both over the flanks of the Mid-Atlantic Ridge and inside ridge-flank canyons, and it has been suggested that this bottom-enhanced mixing comes from the breaking of internal waves forced by tidal currents over rough topography (Polzin et al., 1997; Ledwell et al., 2000). This explanation has been corroborated by numerical simulations that can reproduce much of the observed bottom-enhanced dissipation rates by forcing tidal flow over abyssal hills (Nikurashin and Legg, 2011). Inside the ridge-flank canyons, however, the picture becomes more complicated. Close to the seafloor, hydraulics-related processes over abyssal sills cutting the along-canyon axis have been reported to influence the local turbulent mixing (Thurnherr et al., 2005). Away from the seafloor but still within the canyons, the local mixing may be affected by the interaction between internal tides, near-inertial waves and the mean flow (Toole, 2007; Clément et al., 2017).

Our focus here is on the subinertial response to bottom-enhanced mixing over the mid-ocean ridge and inside the ridge flank canyons. It is currently impossible to resolve the generation and breaking of internal waves while considering the entire mid-ocean ridge spanning thousands of kilometers. We thus ignore the presence of small-scale abyssal hills and represent the associated mixing by turbulent diffusion. We apply the observed bottom-enhanced turbulent diffusivity profile as a function of height above the bottom. We expect that deep canyons cutting across the full width of the ridge flanks have a more pronounced effect on the subinertial flows than the more broken-up abyssal-hill topography.

Our model simulations all start with uniform background stratification with the prescribed bottom-enhanced mixing acting to homogenize the water column. We focus on the evolution of mean flows and stratification over subinertial time scales. Note that our simulations do not reach long-term equilibrium due to the absence of bottom water import and lighter deep water export. However, the targeted boundary layer dynamics and associated restratification occur on much faster timescales and thus the transient solutions could shed light on the key processes regardless of the long-term equilibrium. The detailed model configuration is provided in section 3.3.

We first consider the mixing-driven mean flows in a mid-ocean ridge system without canyons in both two-dimensional and three-dimensional set-ups. We confirm that submesoscale baroclinic instability helps maintain a realistic stratification over the mid-ocean ridges, consistent with predictions made over planar slopes. This is detailed in section 3.4, along with some discussions on the modifications of the induced flow structures compared with those in the planar slope experiments; The effects of canyons are examined in section 3.5 where we find an effective restratification associated with a strong up-canyon flow inside the ridge flank canyons. The flow pattern within the canyons is explained and also compared with *in-situ* observations; We discuss the implications of these flow structures and re-stratification mechanisms for water mass transformation from different components of the mid-ocean ridge system in section 3.6 and a summary of our main findings is provided in section 3.7.

3.3 Numerical model configuration

All numerical experiments described below employ the same basic model configuration. We use the MIT general circulation model (MITgcm, Marshall et al., 1997) to solve the hydrostatic Boussinesq equations

$$u_t + \mathbf{u} \cdot \nabla u - f v = -p_x + (\nu u_z)_z - \nu_4 \nabla_h^4 u, \tag{3.1}$$

$$v_t + \mathbf{u} \cdot \nabla v + f u = -p_y + (\nu v_z)_z - \nu_4 \nabla_h^4 v, \tag{3.2}$$

$$b = p_z, \tag{3.3}$$

$$\nabla \cdot \mathbf{u} = 0, \tag{3.4}$$

$$b_t + \mathbf{u} \cdot \nabla b = [\kappa(N^2 + b_z)]_z - \kappa_4 \nabla_h^4 b. \tag{3.5}$$

Here, $\mathbf{u} = u\mathbf{x} + v\mathbf{y} + w\mathbf{z}$ is the velocity vector, buoyancy $b = -g\rho'/\rho_0$ is defined as a perturbation from the background buoyancy profile $N^2 z$, ρ' is the density perturbation, ρ_0 is a constant reference density, and p is pressure normalized by the reference density.[1] Biharmonic horizontal diffusion with coefficients $\nu_4 = \kappa_4 = 3.125 \times 10^4\,\mathrm{m^4\,s^{-1}}$ is included to absorb grid-scale noise. In the x-direction, the model domain is 1000 km wide, and the grid spacing is $\Delta x = 2.5\,\mathrm{km}$. In the y-direction (if present), the domain is 100 km wide, and the grid spacing is $\Delta y = 2.5\,\mathrm{km}$ as well. The domain is 1500 m tall, and the vertical grid spacing is $\Delta z = 2\,\mathrm{m}$. The model is integrated with a 1000 s time step. The vertical diffusivity κ and viscosity ν are prescribed as profiles depending on the local height above the bottom:

$$\nu = \kappa = \kappa_0 + \kappa_1 e^{-z/h}. \tag{3.6}$$

The values $\kappa_0 = 6 \times 10^{-5}\,\mathrm{m^2\,s^{-1}}$, $\kappa_1 = 2 \times 10^{-3}\,\mathrm{m^2\,s^{-1}}$, and $h = 200\,\mathrm{m}$ were obtained by fitting this functional form to the observed bottom-enhanced diffusivity profile observed in the Brazil Basin (Fig. 3.1c, Callies, 2018). The turbulent Prandtl number is $\mathrm{Pr} = \nu/\kappa = 1$. All these values are fixed throughout the numerical experiments, along with the inertial frequency $f = -5.5 \times 10^{-5}\,\mathrm{s^{-1}}$ for the latitude of the Brazil Basin. The background buoyancy frequency is $N = 10^{-3}\,\mathrm{s^{-1}}$. Insulating boundary conditions are applied at both the bottom and the top of the model domain. No-slip and free-slip boundary conditions are used at the bottom and top, respectively. Periodic boundary conditions are imposed in both horizontal directions.

All the simulations start from rest and the initial flow acceleration is induced by mixing-driven buoyancy diffusion. The prescribed diapycnal mixing acting on the background stratification generates vertical buoyancy flux that accumulates the

---

[1] The MITgcm solves for the full buoyancy $N^2 z + b$, but the split into the background and a perturbation becomes useful when making connection to boundary layer theory (see below).

local available potential energy, which subsequently energizes the mean flows and submesoscale baroclinic eddies.

3.4 Mean flows and submesoscale baroclinic eddies over mid-ocean ridge flanks

The two-dimensional ridge

When mixing occurs near sloping boundaries, isopycnals tilt down toward the slope because turbulent buoyancy fluxes converge on the insulating boundary. An upslope near-bottom flow is induced that balances the convergence of the buoyancy flux with the advection of dense water from below. For constant mixing coefficients and infinitely extending slopes, simple analytical solutions can be derived for both a non-rotating system (Wunsch, 1970; Phillips, 1970) and a rotating system (Wunsch, 1970; Thorpe, 1987). The magnitude of these up-slope flows are much larger in the non-rotating than in the rotating case. In a rotating system, the Coriolis force deflects the cross-slope momentum into the along-slope direction, and for weak slopes the boundary layer is in an approximate Ekman balance.

When the mixing is intensified towards the bottom, there is a layer of buoyancy flux divergence that is balanced by downslope flow (Garrett, 1991; Callies, 2018). The dipolar cross-slope flow has a restratifying tendency for the boundary layer system. But in the planar-slope case, this mean-flow restratification is too weak to sustain strong stratification and thus allow sustained mixing.

When variations in topographic slopes are introduced, mass convergence and divergence can be induced by variations in the cross-slope flow. Our goal here is to examine whether the large-scale variations in the topographic slope of a mid-ocean ridge can modify the mean flow field and the associated restratification, or whether a local application of the planar-slope dynamics captures the essential physics.

To that end, we consider a two-dimensional large-scale ridge of sinusoidal shape (Fig. 3.1a). The setup is as described in Section 3.3, except that no y-dependence is allowed.

As initially flat isopycnals tilt down into the slope because of the prescribed mixing, buoyancy forces accelerate the water in the cross-ridge direction. In a thin layer near the bottom, an up-ridge flow of order $10^{-4}\,\mathrm{m\,s^{-1}}$ develops (Fig. 3.3a). A weaker downwelling emerges in a broader outer layer further up in the water column (Fig. 3.3a). Because of Earth's rotation, an along-ridge mean flow develops that is much stronger than the cross-ridge flow (Fig. 3.3b). The dipole pattern in the cross-slope direction is consistent with mixing-driven boundary layer solutions derived over a planar slope and with bottom-enhanced mixing (Garrett, 1991; Callies, 2018), although the magnitude of the flow is much weaker in this two-dimensional system than in the one-dimensional planar-slope case (Fig. 3.4a, b). The discrepancy in the mean flow field between these two cases will be explained later in this section.

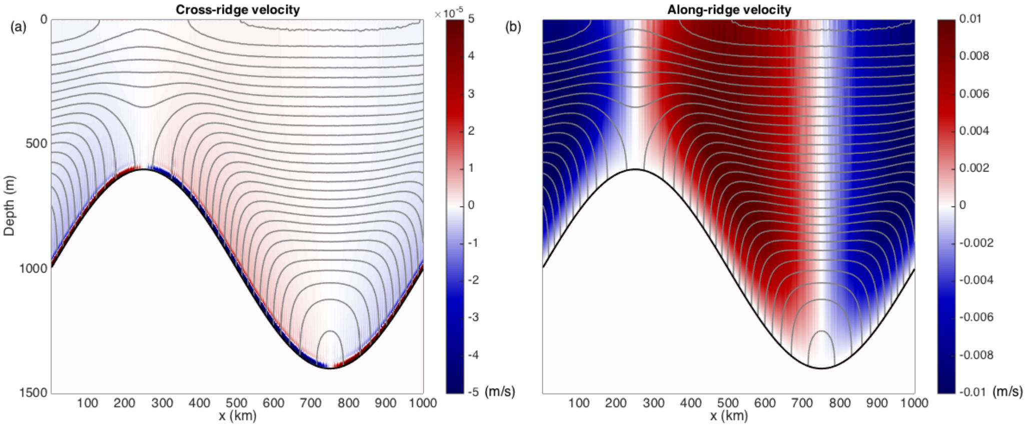

Figure 3.3: Flow in the two-dimensional simulation at day 694. (a) Cross-ridge flow showing strong near-bottom upwelling and a weaker return flow above. (b) Along-ridge flow showing thermal-wind shear in the weakly stratified layer and nearly depth-independent flow above.

Since the cross-ridge flow in the two dimensional system is even weaker than the planar slope case (Fig. 3.4a, b), the cross-slope buoyancy advection and thus the associated restratification are weak. As a result, stratification keeps getting eroded in the mixing layer (Fig. 3.5a). Just like in the one-dimensional case in Callies (2018), two-dimensional setup does not capture the physics required to maintain realistic stratification. (Note that the simulated system is also not self-consistent because the generation and breaking of internal waves would be strongly modified by the homogenized layer, and it is unlikely the prescribed mixing profile would emerge in that situation.)

We now compare the velocity and stratification evolution at the center of the two-dimensional ridge flank ($x = 0$) and in the planar slope system. Note that with all perturbations assumed independent of the cross- and along-slope directions, the planar slope BBL system reduces to a one-dimensional system in the slope-normal direction. In the two-dimensional domain, buoyancy evolution is only subjected to vertical diffusion and cross-ridge advection associated with the weak cross-ridge velocity. It has been shown that mixing-driven BBL over a planar slope in a rotating

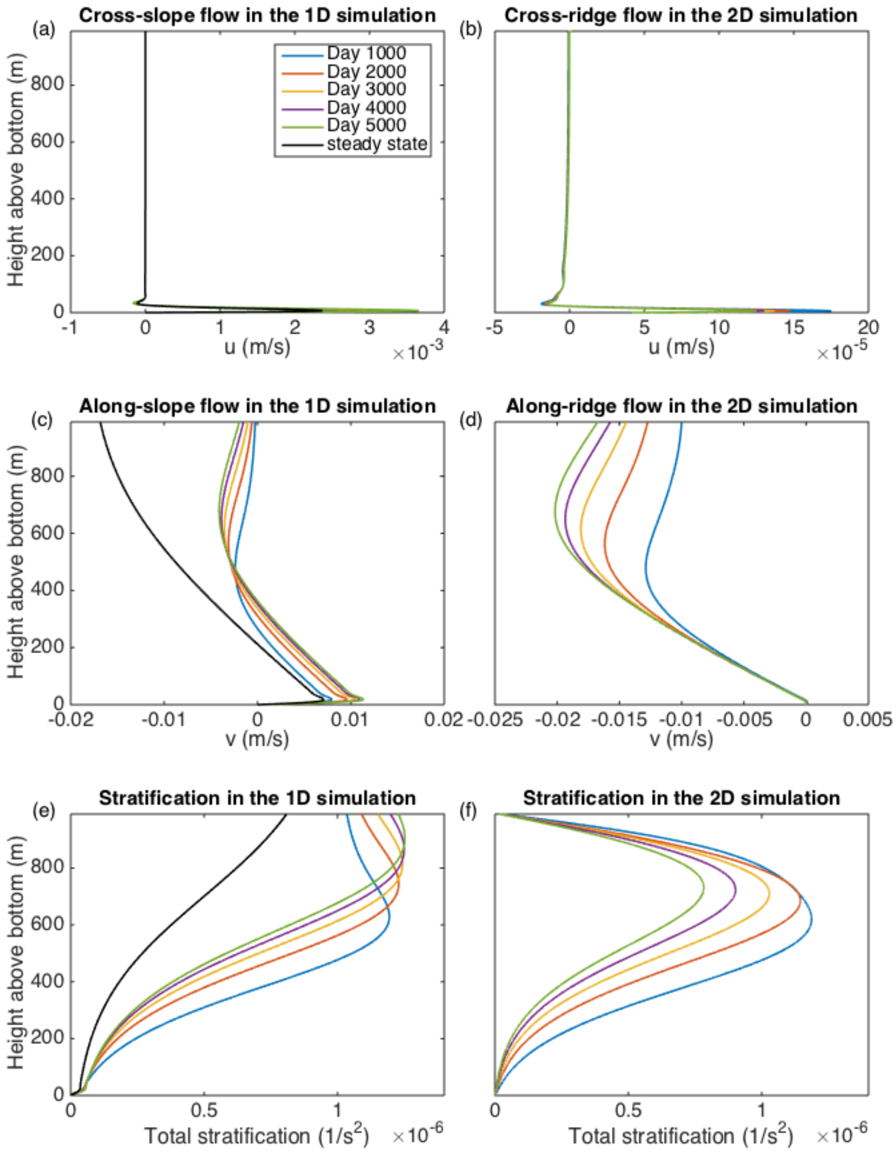

Figure 3.4: Comparison between the one-dimensional planar slope solution (left) and the two-dimensional model solution at the center of the ridge flank ($x = 0$, right). (a, b) Cross-ridge velocity profiles, (c, d) along-ridge velocity profiles, and (e, f) stratification profiles. The times after initialization with a uniform buoyancy and no flow are noted in the legend. For the one-dimensional solution, we also show the steady state.

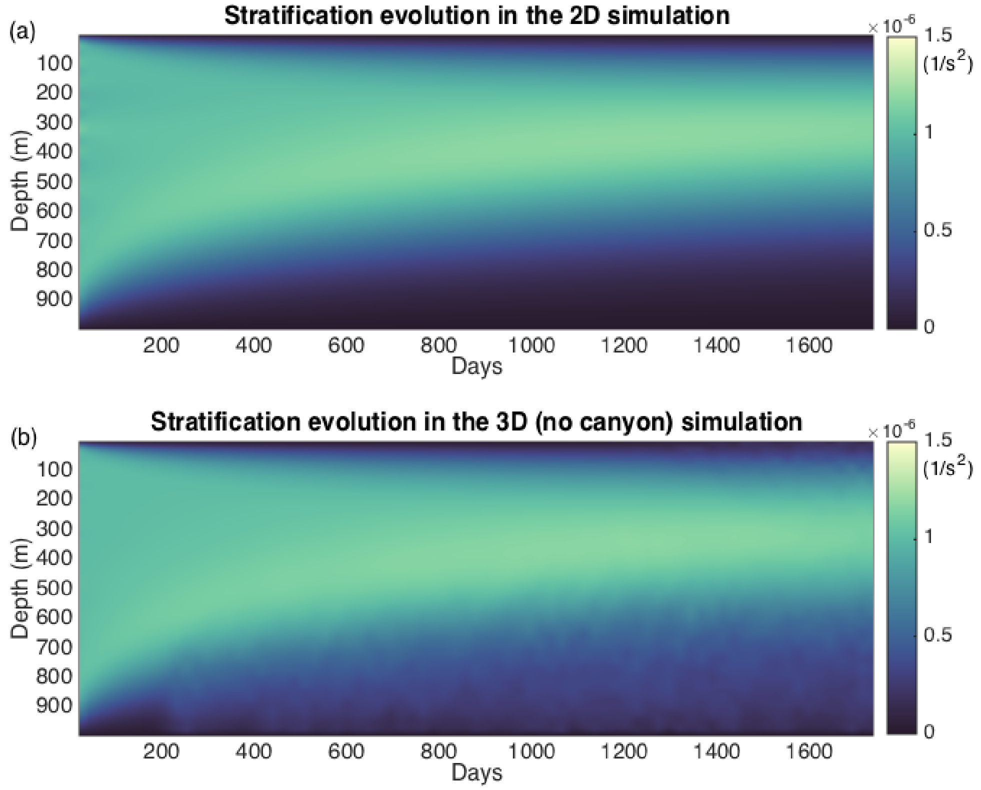

Figure 3.5: Submesoscale baroclinic eddies maintain the stratification over the ridge flanks. The evolution of stratification at the center of the ridge flank ($x = 0$) is shown for (a) the two-dimensional simulation and (b) the three-dimensional simulation without a canyon. In the three-dimensional case, the stratification is averaged over the along-ridge dimension.

system, as described by the equations below, produces a cross-slope flow that is too weak to re-stratify the near-bottom fluid (Callies, 2018):

$$\acute{u}_t - f\acute{v}\cos\theta = b\sin\theta + (\nu\acute{u}_{\acute{z}})_{\acute{z}}, \tag{3.7}$$

$$\acute{v}_t + f\acute{u}\cos\theta = (\nu\acute{v}_{\acute{z}})_{\acute{z}}, \tag{3.8}$$

$$p_{\acute{z}} = b\cos\theta, \tag{3.9}$$

$$b_t + \acute{u}N^2\sin\theta = [\kappa(N^2\cos\theta + b_{\acute{z}})]_{\acute{z}}. \tag{3.10}$$

The equations above are solved using Dedalus (Burns et al., 2016). The slope-normal direction is projected onto 256 Chebyshev modes. Time stepping is performed with an implicit third-order Runge-Kutta scheme. The domain height is 2500 m and a time step of 3 hours is applied. Here, $\theta = 2 \times 10^{-3}$ is the planar slope angle. The coordinate is rotated such that the $\acute{x}$-axis is along the up-slope direction and the $\acute{z}$-axis is the slope-normal direction.

Although the qualitative dipole structures look similar in this two-dimensional simulation compared with the one-dimensional evolution described by equations (3.7)-(3.10), differences in the flow magnitude appear later in the simulation (Fig. 3.4). The one-dimensional cross-slope velocity near the bottom is an order of magnitude stronger than that in the simulated two-dimensional ridge system (Fig. 3.4a, b). At the same time, the flow reversal in the along-slope velocity near the bottom in the one-dimensional system disappears in the two-dimensional simulation (Fig. 3.4c, d). Not only is the structure of the along-slope velocity different, its evolution is much faster in the two-dimensional system. The buoyancy distribution between the one-dimensional planar slope and two-dimensional ridge systems is very similar near the bottom, which also confirms the negligible role of the cross-ridge flow in re-distributing buoyancy across the slope (Fig. 3.4e, f). The discrepancy in the upper water column is due to the insulating boundary condition implemented at the upper boundary in the model, which is absent in the one-dimensional system.

We now explain the differences in both the magnitude and structures of the flow field between the one-dimensional and two-dimensional systems. First, the two-dimensional model topography helps re-distribute momentum in the interior due to the fast adjustment processes, e.g. geostrophic adjustment. The BBL then responds to the modification of the interior flows. This contradicts with the adjustment in the one-dimensional system where there is no sources of momentum from the interior. Momentum can only slowly diffuses from the boundary into the interior and sets up the far-field flow over a diffusive timescale. This is the so-called slow-diffusion process (MacCready and Rhines, 1991). Following Callies (2018), the abyssal mixing layer can be divided into an inner layer and an outer layer that feature a diapycnal upwelling and downwelling, respectively. The along- and cross-ridge velocities in the inner layer are related such that the magnitude of the along-ridge flow on top of the inner layer determines the magnitude of the cross-ridge flow, as in an Ekman layer. Thus, the weaker cross-ridge flow near the bottom in the two-dimensional system corresponds to a loss of the along-ridge flow on top of the inner layer.

This difference in the along-slope flow magnitude is due to a mass continuity requirement in the x direction inside the two-dimensional model domain. This can be further explained with the model along-slope momentum equation (3.2) integrated in the vertical direction:

$$\frac{\partial}{\partial t}\int_{-h}^{0} v dz + f\int_{-h}^{0} u dz = (-\nu v_z)\,|_{-h}. \tag{3.11}$$

Here $z = -h(x)$ is the solid bottom and free-slip (no-stress) boundary condition is applied at $z = 0$. Note that the depth-integrated transport should be the same in the x-direction due to the mass continuity constraint and so we have dropped the vertical integral of the biharmonic diffusion term. The pressure gradient and advection terms also disappear because of the symmetry in the along-slope direction and the integral across the BBL where turbulence is vigorous. While the integrated transport in the x direction being uniform, the transport should also be in opposite directions on two sides of the ridge crest (e.g. at $x = 100\,\text{km}$ and $x = 400\,\text{km}$ where the ridge crest is at $x = 250\,\text{km}$). These require that over a two-dimensional symmetric topography as in the case of a sinusoidal ridge simulation, the depth-integrated transport in the x direction has to be zero to satisfy both constraints as described above. As a result, only two terms are left in the integrated momentum equation in the along-ridge direction after the depth-integrated transport is removed:

$$\frac{\partial}{\partial t}\int_{-h}^{0} v dz = (-\nu v_z)\,|_{-h}. \tag{3.12}$$

This implies that the bottom stress determines the evolution of the depth-integrated transport in the along-slope direction. This is an additional constraint on the momentum evolution compared with the one-dimensional system. Consequently, the two-dimensional model features an evolution towards a state of no bottom stress in the along-slope direction as the steady state is approaching, as shown in Fig. 3.4d. We expect this constraint to be relaxed in a full three-dimensional environment or over asymmetric topography.

The three-dimensional ridge

We now allow for flow variations in a third dimension (the y-axis is in the meridional direction, with positive y pointing to the north), but retain a smooth ridge flank (Fig. 3.1a). We expect submesoscale baroclinic eddies to develop, as in the planar slope case, that can move dense water under light water horizontally and maintain stratification in abyssal mixing layers.

In the same transient experiment started from a uniform stratification as considered above, we again see isopycnals tilting down into the slope. No coherent mean flows are generated but now baroclinic instability can develop and utilize the available

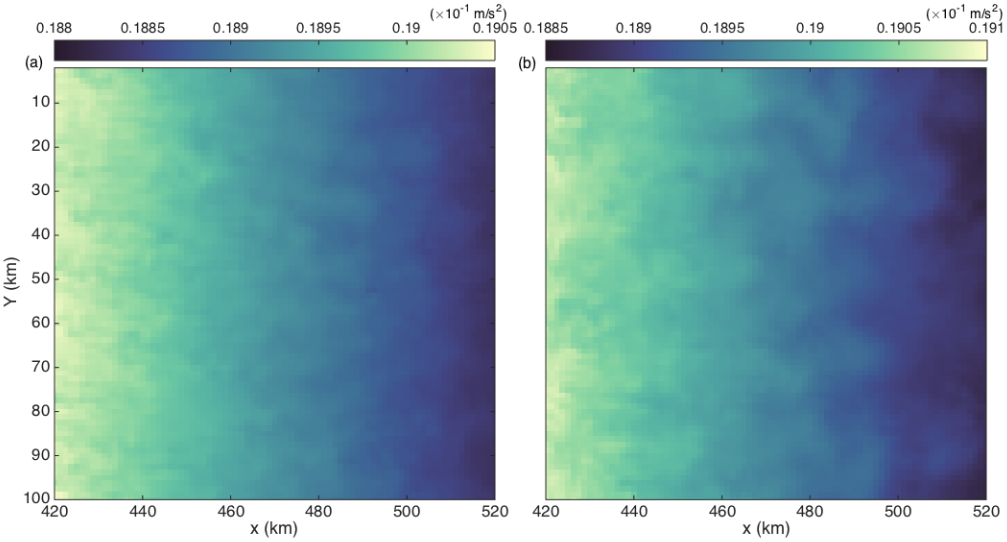

Figure 3.6: Development of submesoscale baroclinic eddies over the mid-ocean ridge flank in the three-dimensional simulation without a canyon. Shown is the buoyancy field on (a) day 926 and (b) day 1852 at $z = 800\,\mathrm{m}$.

potential energy associated with the tilting isopycnals. Submesoscale baroclinic eddies (with an eddy size around 10 km) are found in the mixing layer over the ridge flanks (Fig. 3.6).[2] As a result, the mixing layers over the ridge flanks remains more stratified than those in the two-dimensional case (Fig. 3.5). The sharp difference in the stratification emerges after day 200, when the baroclinic eddies start developing in the three-dimensional run. We thus confirm that submesoscale baroclinic instability plays an important role in maintaining the stratification over the flanks of a three-dimensional mid-ocean ridge. The phenomenology on the ridge flanks is consistent with the vigorous restratification by submesoscale eddies found on planar slopes (Callies, 2018). The submesoscale restratification is less strong over the crest and trough, where the slopes become more gentle (for more details see Fig. 3.12 and Section 3.6).

---

[2] For visualization purposes, the developed eddy field shown in Fig. 3.6 is from a run with double the horizontal resolution ($\Delta x = \Delta y = 1.25\,\mathrm{km}$). Computational constraints prevent us from running that simulation long enough to produce the diagnostics discussed below, but we have confirmed that the three-dimensional simulation with $\Delta x = \Delta y = 2.5\,\mathrm{km}$ we use throughout the rest of the paper produces similar baroclinic restratification tendencies as the higher-resolution run.

3.5 Circulation and restratification in ridge flank canyons

We now add to our large-scale ridge bathymetry a fracture zone canyon that runs across the flank of the ridge (Fig. 3.1b). One deep canyon is inserted along the x-direction and at $y = 50$ km. The domain is 100 km wide in the along-ridge direction, and the setup's periodicity means this corresponds to a canyon running across the ridge flank every 100 km. The canyon is given the shape of a Gaussian function shown below, and it is 400 m deep and 20 km wide:

$$h(y) = 400 \times \exp[-\frac{(y - 5 \times 10^4)^2}{2 \times (4.5 \times 10^3)^2}] \tag{3.13}$$

The model bathymetry is based on the real bathymetry of the South Atlantic Mid-Atlantic Ridge (Fig. 3.2b). Real fracture zone canyons are spaced at about the same along-ridge distance of order 100 km. The ridge flanks between canyons have abyssal-hill topography but no coherent incisions running across the ridge flank. Our setup thus captures only the most prominent features of the bathymetry—abyssal hills are included again only indirectly through their effect on mixing, which is parameterized as a bottom-enhanced diffusivity profile. Note also that our idealized canyon setup is a simplification because real canyons can be interrupted by abyssal-hill topography, whereas our canyon runs uninterrupted from the base of the ridge to its crest. Our model canyon is shallow compared to the canyon site studied in the Brazil Basin Tracer Release Experiment (Thurnherr et al., 2005; Toole, 2007) and Dynamics of Mid-Ocean Ridge Experiment (Clément et al., 2017), where the canyon is more than 1000 m deep. Despite these differences, we posit that out idealized model bathymetry captures the essential dynamics introduced by the presence of ridge flank canyons.

To better resolve the steep canyon walls, the model resolution is increased in the y-direction from $\Delta y = 2.5$ km to $\Delta y = 200$ m. The time step is reduced accordingly to 100 s. We perform the same transient mixing-driven experiment started from uniform stratification and rest as above. We run this experiment for 856 days.

We first compare the cross-ridge flows in the three-dimensional simulations with and without a canyon. The flow reaches a quasi-equilibrium in which the stratification at the ridge base and crest drift, but the flow and stratification on the ridge flanks changes relatively little. In the velocity fields averaged over the last 115 days of the simulation (days 741–856), it becomes apparent that no significant cross-ridge mean flows are generated in the simulation without a canyon (Fig. 3.7a). Instead, the cross-slope velocity field shows the eddying flow structures associated with the

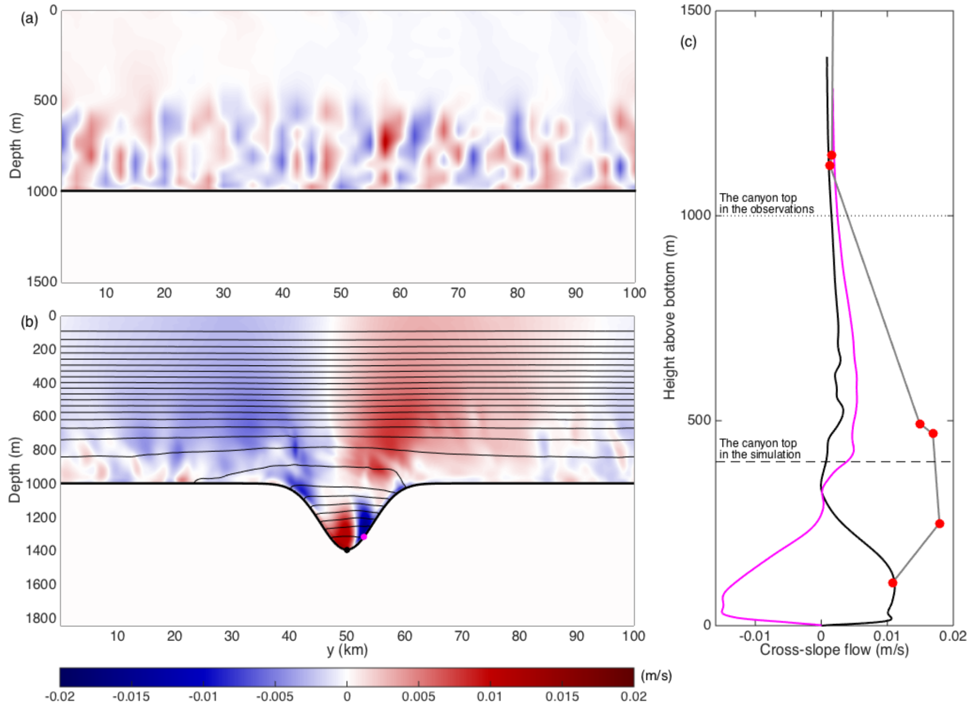

Figure 3.7: Comparison of the cross-ridge velocity between the simulations with and without a canyon and *in situ* observation from the Brazil Basin Tracer Release Experiment. (a) Cross-ridge velocity in the three-dimensional simulation without canyon averaged over days 741–856, (b) cross-ridge (i.e. along-canyon) velocity in the three-dimensional simulation with canyon averaged over days 741–856, (c) comparison of the along-canyon velocity profiles between the simulation and mooring observation. The black and magenta curves in (c) correspond to the sampling locations marked in (b). The red dots denote the record mean along-canyon velocity from the mooring. The dotted and dashed lines roughly represent the canyon tops in the observations and the simulation.

submesoscale baroclinic eddies discussed in the previous section. In the simulation with a canyon, in contrast, a strong flow with a maximum velocity of over 1 cm runs up the ridge inside the canyon (Fig. 3.7b). This large up-ridge flow is banked slighted against the southern wall of the canyon and is accompanied by a return flow on the northern side of the canyon. We will explain the locations of the up- and down-ridge flows below. The up-ridge flows extend along the canyon axis across the entire ridge flank (Fig. 3.8a). Above the canyon, two larger-scale geostrophically balanced flows ($\sim 0.005\,\mathrm{m\,s^{-1}}$) run in opposite directions. They are due to the prescribed mixing and the subsequent tilting of isopycnals on the canyon walls.

As part of the Brazil Basin Tracer Release Experiment in 1997, a mooring was

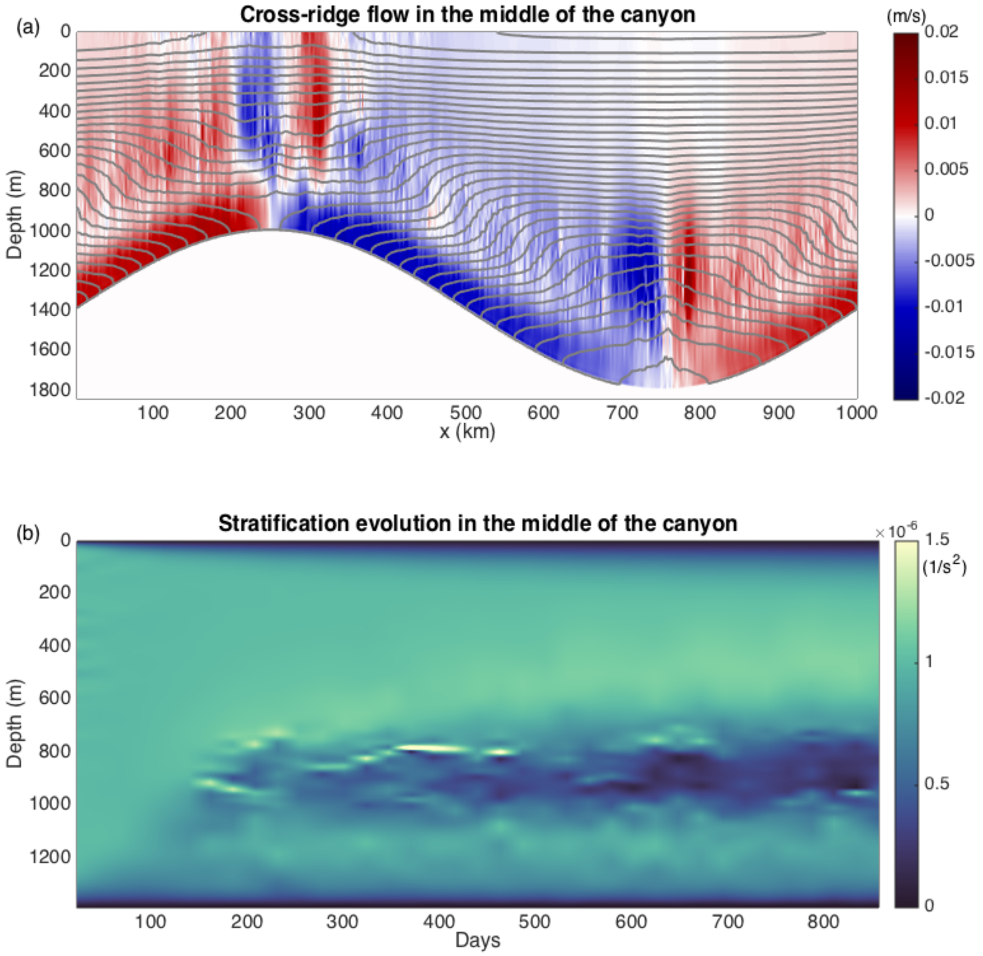

Figure 3.8: The cross-ridge flow and stratification evolution inside the canyon. (a) The cross-ridge velocity averaged over days 694–856 along the center axis of the canyon (y = 50 km). (b) Time evolution of stratification in the center of the ridge flank and in the center of the canyon (x = 0 and y = 50 km).

deployed in a deep canyon on the western flank of the Mid-Atlantic Ridge near 22°S (Thurnherr et al., 2005; Toole, 2007). Eight current meters recorded velocities at half-hour intervals for a little over two years. We compare the record mean *in situ* measurements with the simulated flow (again averaged over days 741–856) in the corresponding location in the middle of the ridge flank ($x = 0$) and inside our idealized canyon. Given the strong cross-canyon shear, we sample the simulated cross-ridge velocity with vertical profiles at two different locations: one in the center of the canyon ($y = 50\,\mathrm{km}$) and one located in the return flow ($y = 53\,\mathrm{km}$, Fig. 3.7b).

The simulated up-ridge flow qualitatively agrees with the measured velocity profile, both in magnitude and in vertical structure (Fig. 3.7c). The simulated flow is weaker and more confined in the vertical than the observed flow, as might be expected because the canyon in the simulation is shallower than the about 1000 m deep canyon the mooring was placed in. The difference in the magnitude of the cross-slope flow is also likely due to the difference in the canyon width such that the observed canyon (∼10km wide) is narrower than the idealized canyon (∼20km wide), which has a difference in the blocking effects of the cross-canyon flows (this is explained later). The presence of the strong return flow in the simulation warrants caution in inferring up-ridge transport from moored observations—the inferred transport in the canyon can depend sensitively on where exactly the mooring is placed.

The up-ridge flow inside the canyon is orders of magnitude larger than that in the simulations without a canyon (Section 3.4). As pointed out by Dell (2013), the canyon walls block along-ridge flow, preventing the across-ridge momentum that is generated by buoyancy forces from being deflected into the along-ridge direction. The cross-ridge flow in the canyon can be captured qualitatively by the one-dimensional system (3.7)–(3.10), modified by setting $v = 0$, or equivalently $f = 0$.

We here extend Dell's argument to the case with bottom-intensified mixing. We illustrate the impact of the blocking of the along-ridge flow by canyon walls by solving the one-dimensional system (3.7)–(3.10) for the steady-state flows and stratification with and without rotation. The equations are solved with the same procedures in Dedalus as in the temporal evolution case (section 3.4 and Fig. 3.4), with the time-dependent terms set to 0. The non-rotating solution represents a case in which the along-slope flow is blocked perfectly by the canyon walls; the rotating case is the same as that considered in Section 3.4a and corresponds to a planar slope. In the blocked case, an up-ridge flow spans the bottom 100 m and has a maximum in

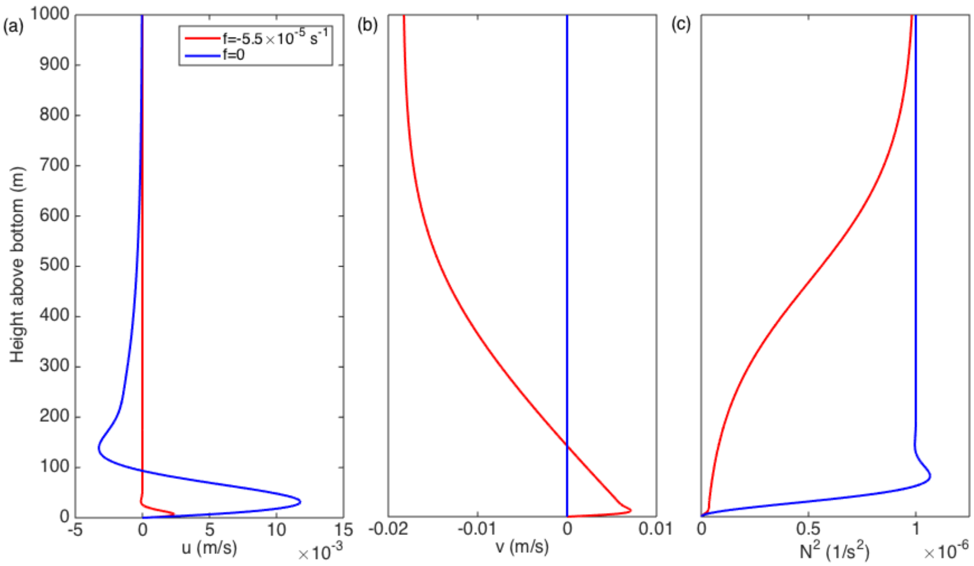

Figure 3.9: Comparison between the one-dimensional solutions of the unblocked (rotating, $f = -5 \times 10^{-5}\,\mathrm{s}^{-1}$) and blocked (non-rotating, $f = 0$) cases. (a) Cross-ridge velocity, (b) along-ridge velocity, and (c) stratification. All curves show the steady-state solutions.

excess of $1\,\mathrm{cm\,s^{-1}}$, i.e. it is much larger than any cross-ridge flow in the rotating case (Fig. 3.9a). The bottom-intensification of the mixing drives a return flow above 100 m, which has a magnitude only somewhat weaker than the up-ridge flow. The up-ridge flow in the blocked case is captured to leading order by the approximate analytical solution (Callies, 2018)

$$u = -\frac{\kappa_1 \cot\theta\, e^{-z/h}}{h} + 2q \cot\theta\,(\kappa_0 + \kappa_1) e^{-qz} \sin qz, \quad \text{where} \quad q^4 = \frac{N^2 \sin^2\theta}{4(\nu_0 + \nu_1)(\kappa_0 + \kappa_1)}. \tag{3.14}$$

The approximation leading to (3.14) is marginal because it requires $qh \gg 1$ while $qh = 4.4$ for the parameters used here, but it still qualitatively captures the numerical solution.

The strong cross-ridge flow allowed by the along-ridge blocking is strong enough to maintain strong stratification (Fig. 3.9c). The stratification in the outer layer (above $q^{-1} = 45\,\mathrm{m}$) is close to the far-field value. The stratification is reduced only in the inner layer. This is in stark contrast to the rotating case, where stratification is reduced throughout the outer layer extending to $h \log \kappa_1/\kappa_0 = 700\,\mathrm{m}$ (Fig. 3.9c).

Here in this one-dimensional system, it is clear that the canyon wall blocks the development of the along-ridge flow, and thus enhances the cross-ridge flows inside the canyons. This confirms the role of the canyon walls in developing the strong up-canyon flow in the three-dimensional simulation (Fig. 3.7). The return flow, as part of the dipole flow structure in response to bottom-enhanced mixing, has to sit on top of the strong up-slope flow since no other factors can break the symmetry in the cross-slope direction. We note that the shifted location of the return flow inside the canyon (Fig. 3.7b) is due to the turning of the cross-canyon flow in the local BBL system by Earth's rotation, as explained later in this section.

Similar to the three-dimensional simulation without a canyon, the local stratification inside the canyon gets maintained (Fig. 3.8b). Thus, within the ridge-flank canyon, a strong stratification is maintained due to the mean up-ridge buoyancy advection, implying that the canyon walls have effectively turned the local BBL system into a non-rotating system, thus providing a different re-stratification mechanism compared with the flanks of the large-scale ridge.

Notice that there exists a layer of weak stratification out of the local BBL and higher up inside the canyon, which seems inconsistent with the measured stratification (Fig. 3.8b). After careful examination, we find that the maximum growth rate associated with the submesoscale baroclinic instability (Stone, 1966) inside this weakly stratified layer (with $O(10)$ Richardson number) is $5.5 \times 10^{-6}\,\mathrm{s}^{-1}$. The corresponding wavenumber is about $3.85 \times 10^{-3}\,\mathrm{m}^{-1}$, dimensionalized using a characteristic velocity magnitude $U = 1\,\mathrm{m\,s}^{-1}$ inside the canyon and $f = 5.5 \times 10^{-5}\,\mathrm{s}^{-1}$. The damping rate from the hyperviscosity used in the model at this wavenumber is $6.9 \times 10^{-6}\,\mathrm{s}^{-1}$, of similar magnitude to the maximum growth rate. Thus, this layer of weak stratification is likely an artifact from the model such that the growth of submesoscale baroclinic eddies are damped by the hyperviscosity applied. We expect the layer to be more stratified once smaller scale baroclinic eddies are resolved. On the other hand, this seemingly unrealistic weak stratification manifests the role of baroclinic restratification from submesoscale eddies inside the canyon in maintaining the local stratification.

As shown in the one-dimensional BBL system in Fig. 3.9a, the return (or downslope) flow sits on top of the much stronger up-slope flow, unlike the shifted return flow inside the canyon (Fig. 3.7b). A similar shift of the return flow was found in a previous simulation over a planar slope bounded by purely vertical sidewalls (Dell, 2013). This was explained such that weak cross-canyon flows turn to the left in the southern hemisphere and form the downslope flow on the northern canyon wall. To confirm that this explanation holds with the current sloping canyon wall

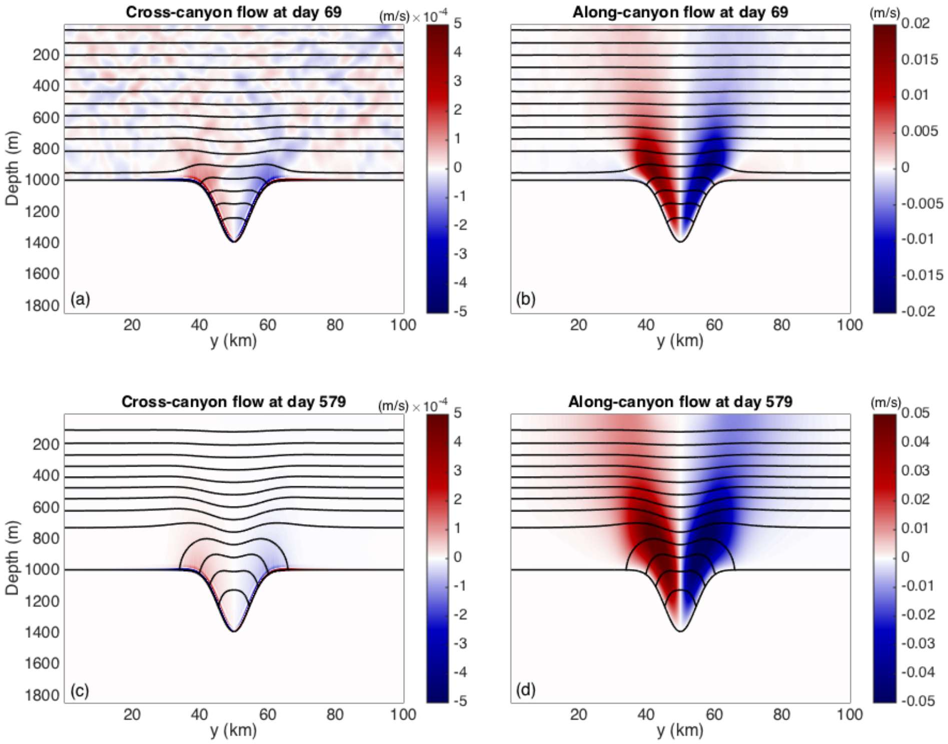

Figure 3.10: Flows in a two-dimensional canyon without the large-scale ridge. (a) Cross-canyon flow at day 69, (b) along-canyon flow at day 69, (c) cross-canyon flow at day 579, (d) along-canyon flow at day 579. The shading shows velocities, black contours are isopycnals.

set-up, we designed a series of simulations to isolate different components in the three-dimensional simulation that might break this symmetry. We first ran a two-dimensional simulation with the large-scale ridge removed, in order to ensure that the return flow is part of the solution in the large-scale ridge system. The simulation results are shown in Fig. 3.10, where there is only symmetric along-slope flows in the canyon. In this local one-dimensional BBL system inside the canyon, the up-slope flows across the sloping canyon walls turn into the along-slope direction due to the rotation. Outside of the canyon, isopycnals tilt downward as a result of the background mixing and much larger geostrophically-balanced along-slope flows can be seen near the canyon mouth. Throughout the simulation, the symmetry in the along-slope flows across the canyon is maintained. This implies that the shifted return flow is part of the BBL system associated with the large-scale ridge slope. However, there are still at least two candidates in the original three-dimensional

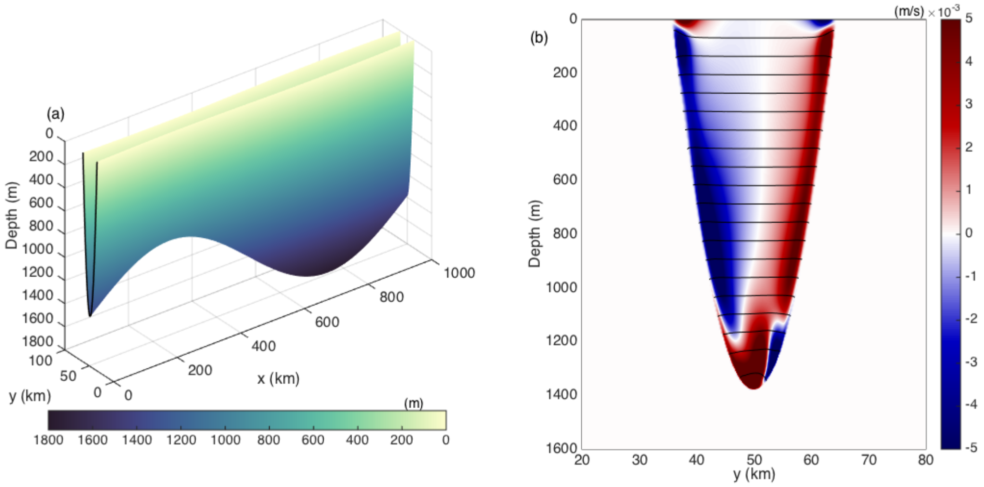

Figure 3.11: Simulation without the ridge flanks, which isolates the canyon effects. (a) model topography, (b) cross-ridge flow at day 35. The shading shows velocities, black contours are isopycnals.

simulation that can break the symmetry and cause the shift of the return flow. The first one is the ridge flank. The along-ridge flow over the ridge flanks can flow into the canyon and interact with the up-canyon flows in the local BBL system above the canyon walls. Mass divergence/convergence can result in vertical velocity and tilt the isopycnals locally and thus break the symmetry across the canyon. The second candidate is Earth's rotation that can deflect the up- and down-ridge flows. To isolate the impact from outside the canyon, we have extended the canyon walls all the way up to the top of the domain (Fig. 3.11a) such that there is no ridge flanks and thus no interaction between the flows from inside and outside the canyon. Upon checking on the distribution of the cross-ridge flow, we have found similar shift in the location of the return flow that is on the northern canyon wall (Fig. 3.11b). This confirms that the primary reason for the shift of the return flow is the Earth's rotation rather than the presence of the ridge flanks and their associated mean flows.

3.6 Water-mass transformation in the mid-ocean ridge system

Given the elevated mixing observed over the rough Mid-Atlantic Ridge flanks in the Brazil Basin Experiment (Polzin et al., 1997) and over rough topography more generally (Waterhouse et al., 2014), rough mid-ocean ridges are likely key locations for diabatic water mass transformation (WMT) and global upwelling pathways for AABW. In this section, we address how WMT is affected by the circulation patterns and restratification on mid-ocean ridges. Diagnosing WMT in our idealized numerical experiments allows us to disentangle what processes are key to maintaining large transformation rates.

We apply the WMT framework developed by Walin (1982). We diagnose the diabatic transformation following Marshall et al. (1999):

$$A(b,t) = -\frac{\partial}{\partial b}\iiint_{R(b,t)} \nabla \cdot \mathbf{F}_b \,\mathrm{d}V \approx \frac{\partial}{\partial b}\iiint_{R(b,t)} (\kappa b_z)_z \,\mathrm{d}V. \tag{3.15}$$

Here $A(b,t)$ is the diapycnal volume flux through a target isopycnal b, and $R(b,t)$ is the volume of fluid between the target isopycnal and the ocean bottom. The diabatic buoyancy flux $\mathbf{F}_b$ is dominated by its vertical component $F_b^z = -\kappa \partial b/\partial z$. Positive A represents the volume of water per unit time crossing to lighter density classes. For the two-dimensional simulation, we assume an along-ridge distance of 100 km to be consistent with the three-dimensional cases.

The effective restratification over the ridge flanks in the three-dimensional (no-canyon) simulation allows for strong buoyancy flux and thus buoyancy flux convergence/divergence, crucial for maintaining a large WMT rate. This is best illustrated in the direct comparison of the local stratification, buoyancy flux and buoyancy flux divergence between the two-dimensional and three-dimensional simulations (Fig. 3.12). When allowing for a third dimension, stratification is stronger over the slopes of the ridge at day 5000 (Fig. 3.12d) and the buoyancy flux in the three-dimensional simulation remains strong ($\sim -3 \times 10^{-10}$ m^{2}s^{-3}) but almost zero in the two-dimensional simulation (Fig. 3.12b, e). Consequently, when the buoyancy flux divergence is computed, strong convergence of buoyancy flux exists in a thin layer near the bottom where the insulating bottom boundary condition takes effect and on top of this strong upwelling layer is large downwelling due to the decay of buoyancy flux further away from the bottom (Fig. 3.12f). The appearance and maintenance of this upwelling and downwelling dipole is closely related to the abyssal horizontal circulation as argued by Callies and Ferrari (2018).

The WMT rates in the two-dimensional and three-dimensional (no canyon) cases are shown in Fig. 3.13. The evolution of the net WMT rate looks similar between these two cases during the adjustment. At the beginning of the simulations, around 0.2 Sv of the dense water upwells into lighter density classes near the bottom of the ridge (near the 0.0183 ms^{-2} isopycnal) due to the strong convergence of buoyancy flux before stratification is eroded. Similar amount of upwelling occurs near the top of the ridge (near the 0.0191 ms^{-2} isopycnal) with strong downwelling on top. As the waters move to lighter density classes near the ridge crest, they move into the region

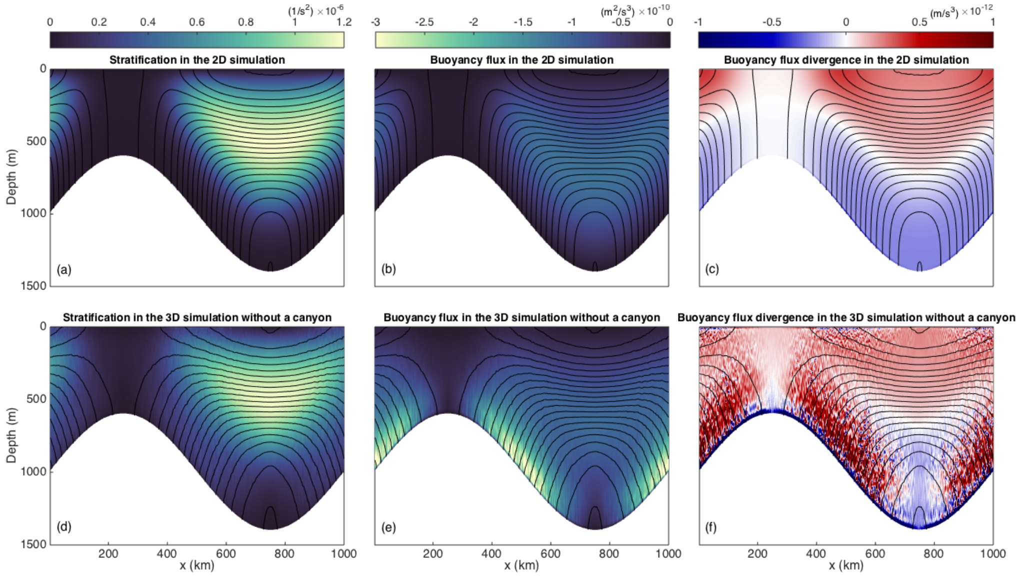

Figure 3.12: Comparison between the two-dimensional and three-dimensional simulations without a canyon. (a) Stratification in the two-dimensional simulation, (b) resulting vertical buoyancy fluxes F_b^z, and (c) their divergence; (d) stratification in the three-dimensional simulation, (e) resulting vertical buoyancy fluxes F_b^z, and (c) their divergence. All fields are shown for day 5000. The three-dimensional fields are averaged over the along-ridge dimension.

with bottom-enhanced diffusivity and thus strong buoyancy flux divergence and a large downwelling rate. As the diapycnal volume flux converges/diverges over the ridge flanks, adiabatic volume flux is induced such that water moves away/towards the mid-ocean ridge along isopycnals (McDougall, 1989). Such adiabatic circulation has been seen in the passive tracer experiment in the Brazil Basin (Hogg and Owens, 1999). Note that these WMT rates also correspond to studies that assume flat isopycnals outside the thin BBL where buoyancy flux converges without considering the erosion and maintenance of local stratification (Ferrari et al., 2016; Holmes et al., 2019). Later in the simulations, the upwelling near the top of the ridge vanishes as isopycnals bend down towards the crest and thus stratification and buoyancy flux become small (Fig. 3.12c). At the same time, the upwelling rates near the bottom of the ridge become smaller due to the weakened stratification and the location where this upwelling occurs shifts to lighter density class. This shift in the upwelling location is due to the fact there is no dense water supply in the model, so the whole system becomes lighter over a long diffusive timescale, but the simulations do reach a quasi-equilibrium state where the diapycnal volume flux A becomes stable.

The reason why the WMT rates are so similar between these two cases is primarily due to the fact that the simulations are not run long enough for the stratification in the two-dimensional case to erode away from the bottom where the mixing is strong and diffusivity is large. We have confirmed with one-dimensional simulation that at least within the first 10000 days, the total buoyancy flux integrated across an isopycnal surface (equivalent to the integral of WMT rates below the targeted isopycnal) only decays to about one-fourth of the total buoyancy flux with realistically-strong stratification (figure not shown).[3] However, with the steady state stratification in the one-dimensional system, the total buoyancy flux decays to about three percent of that with realistic stratification. This adjustment becomes computationally challenging to resolve in our simulations, but it is still highly relevant for abyssal ocean modeling.

The positive and negative contributions to the net WMT in these two cases experience vast difference in their evolution (Fig. 3.13b, d). It is obvious that in the two dimensional simulation, the positive and negative volume fluxes become negligibly small later in the simulation as stratification is eroded. In contrast, in the three-dimensional simulation, both the positive and negative volume fluxes stabilize at around 0.1 Sv over the ridge slopes (Fig. 3.13d) where baroclinic eddies help maintain the stratification. This implies that the local tracer experiences strong upwelling/downwelling dipole pathways over the flanks of the mid-ocean ridge where stratification is maintained.

For the case with a fracture zone canyon, we have to limit our discussion of WMT to the first 850 days, because the reduced grid spacing and time step prevent us from running this simulation as long as the cases without canyon. It appears, however, that the WMT rate has reached a quasi-equilibrium after this time, and we expect these transformation rates to remain stable, as in the three-dimensional case without canyon.

Surprisingly, the evolution of the total net WMT looks similar to the previous no canyon run (Fig. 3.14). Upon examining the contribution from inside and outside of the canyon, the net canyon contribution is almost negligible and only exists at the highest density class. Most of the contribution comes from outside of the canyon

---

[3] The realistically-strong straitification is obtained as described in section 4b of Callies (2018) with the background $N = 10^{-3}\ \mathrm{s}^{-1}$.

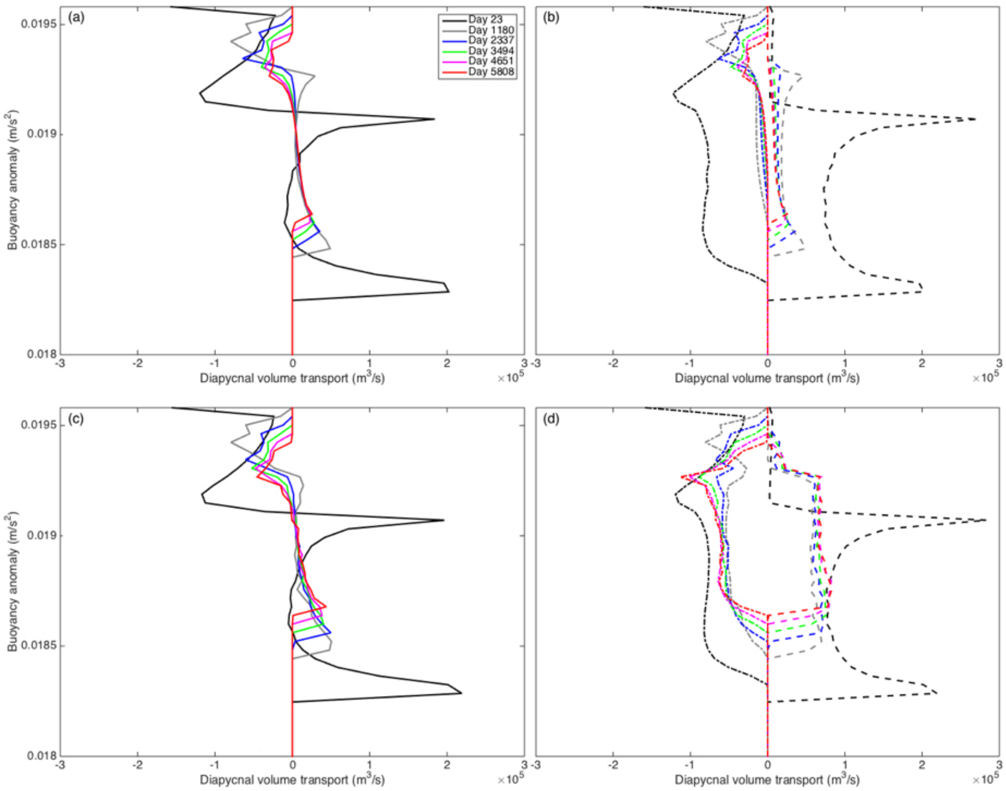

Figure 3.13: Comparison of water mass transformation rates between the two-dimensional and three-dimensional simulations without a canyon. (a) Evolution of WMT in the two-dimensional simulation, (b) decomposition of that WMT into positive and negative contributions, (c) evolution of WMT in the three-dimensional simulation, (d) decomposition of the WMT into positive and negative contributions.

(Fig. 3.14b, c). If we further decompose the contribution into positive and negative components at a developed stage (day 598), there is a large cancellation inside the canyon associated with the mean flow re-stratification (Fig. 3.14e) and the upwelling and downwelling dipole becomes even stronger (per unit width in the along-ridge direction) compared with outside of the canyon because of the larger stratification maintained. A similar comparison in the local stratification, buoyancy flux and buoyancy flux divergence is provided where the strong buoyancy flux and buoyancy flux divergence over the ridge slopes can be seen (Fig. 3.15 g-i). Compared with the three-dimensional run without a canyon, the upwelling/downwelling dipole is now higher in the water column on the flanks of the ridge with a broadened upwelling layer (Fig. 3.15f). This is because the presence of the canyon bends down the isopycnals, which thickens the weakly stratified BBL over the ridge flanks. As a

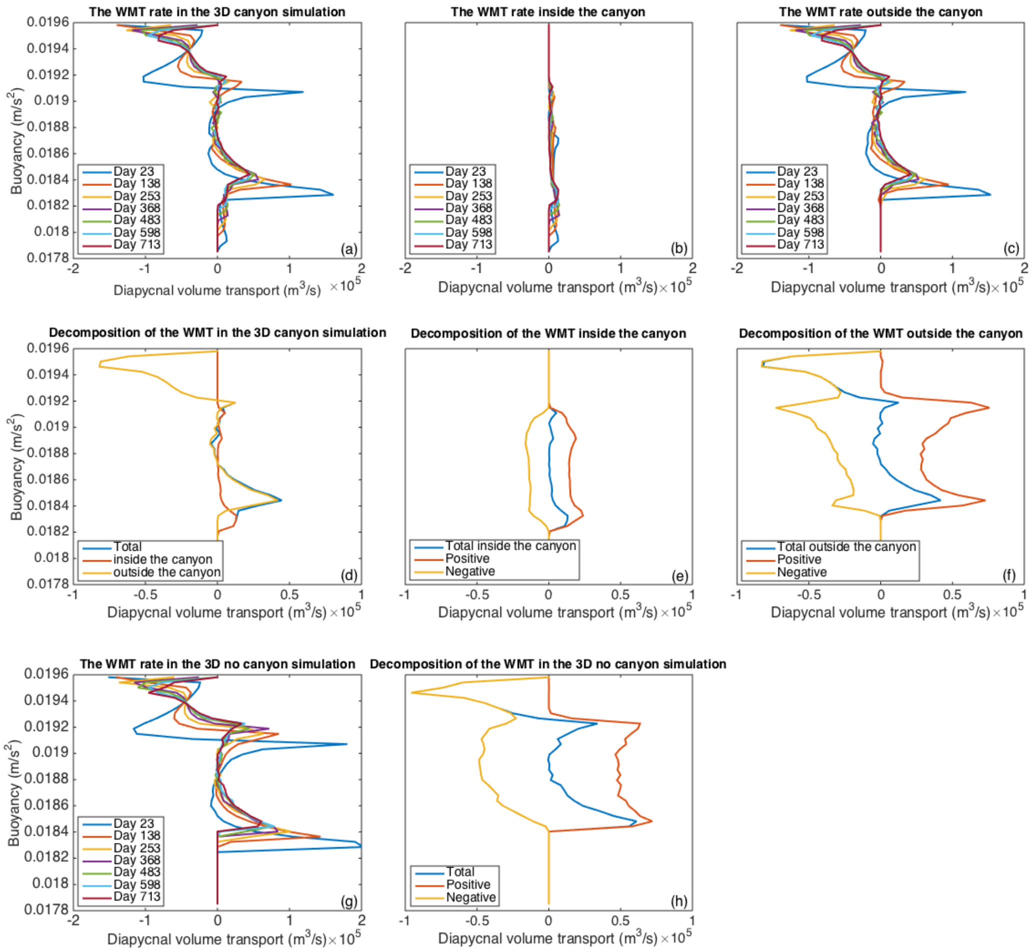

Figure 3.14: Evolution of water mass transformation in the three-dimensional simulation with and without canyon. (a) Evolution of the net WMT in the simulation with canyon, (b) contribution to the net WMT from inside the canyon, (c) contribution to the net WMT from outside the canyon, (d) decomposition of the net WMT in the simulation with canyon into positive and negative contributions, (e) decomposition of the canyon contribution, (f) decomposition of the contribution from outside the canyon, (g) evolution of the net WMT in the simulation without canyon and (h) decomposition of the net WMT in the simulation without canyon into positive and negative contributions

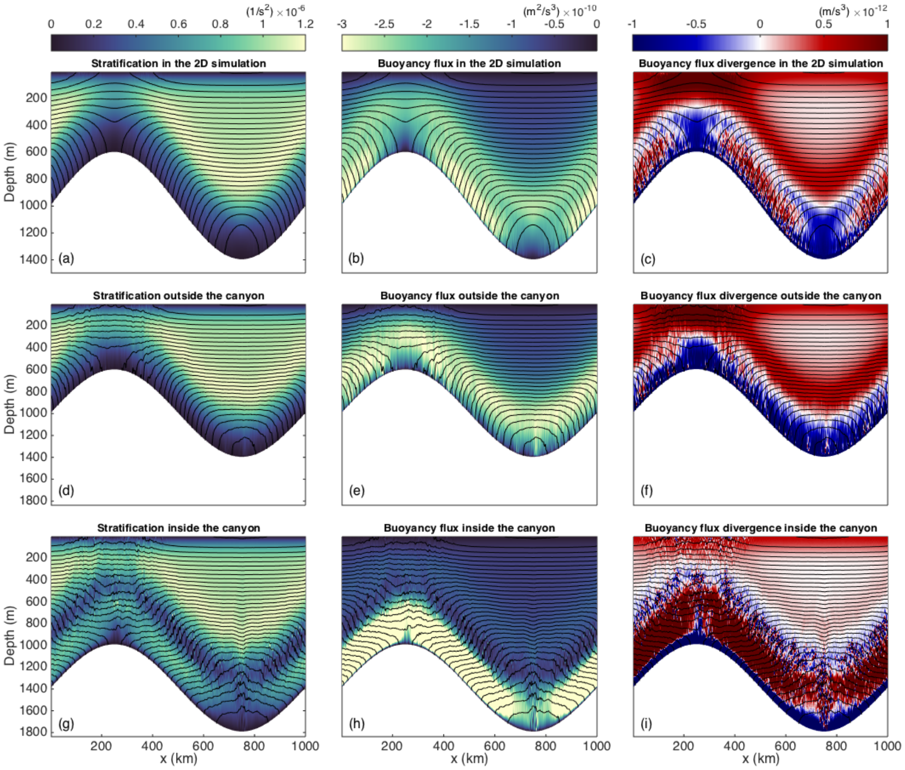

Figure 3.15: Comparison between the three-dimensional simulations with and without canyon. (a) Stratification in the simulation without a canyon (averaged over the along-ridge dimension), (b) resulting vertical buoyancy fluxes F_b^z, and (c) their divergence. The stratification, buoyancy fluxes, and their divergence are also shown for the simulation with canyon, both (d, e, f) outside the canyon ($x = 0$) and (g, h, i) inside the canyon ($x = 50\,\text{km}$).

result, the layer where buoyancy flux converges is thicker and the dipole diabatic pathway is shifted upward (figure not shown).

In summary, we conclude that the maintenance of stratification over the mid-ocean ridge flanks is crucial for effective bottom water consumption. The presence of the ridge-flank canyons helps maintain stratification inside the canyon, but the contribution to net WMT is relatively small due to the large cancellation associated with the dipole diabatic pathway. Note that we do not resolve the small-scale submesoscale baroclinic eddies inside the canyon, and hence the weakly stratified layer above the local BBL and within the canyon (see discussions in section 3.5

and Fig. 3.8b). However, we suspect that with enough resolution, the enhanced stratification in the currently weakly stratified layer would shift the dipole pathway inside the canyon, but the total contribution from inside the canyon to the WMT would not change dramatically, as this is determined by the buoyancy flux coming from outside the canyon. In fact, even if we neglect the cancellation effect from the local buoyancy flux divergence inside the canyon, the lightening volume flux is still smaller than the net contribution from outside the canyon (Fig. 3.14e, f).

Taking an estimated forty degrees of latitude over which mid-Atlantic ridge spans meridionally in the Brazil Basin ($\approx 4000\,\mathrm{km}$), the net lightening diapycnal volume flux of around $0.05\,\mathrm{Sv}$ at the quasi-equilibrium state (Figs. 3.13a, c and 3.14a) in the model domain of $100\,\mathrm{km}$ width sums up to a total $2\,\mathrm{Sv}$ of net bottom water consumption, of the same order of magnitude to previous estimate of $4\,\mathrm{Sv}$ (Hogg et al., 1982). Moreover, the actual upwelling and downwelling rates are stronger than the net such that the upwellling rate can reach around $0.1\,\mathrm{Sv}$ over the ridge flanks in our model domain and thus a total $4\,\mathrm{Sv}$ in the Brazil Basin. The strong dipole pattern is crucial for interpreting local tracer pathways both over the ridge flanks and inside the canyons, as tracers may experience large excursions within the upwelling/downwelling pathways.

3.7 Conclusions

Three sets of numerical simulations are performed in this paper to examine the flow patterns and restratification mechanisms associated with the mid-ocean ridge system: a two-dimensional mid-ocean ridge, a three-dimensional mid-ocean ridge without a canyon and a three-dimensional mid-ocean ridge with a canyon. Similar to the previous findings over a planar slope (Callies, 2018), the restratification with a mean up-slope buoyancy advection over a two-dimensional ridge is too weak to maintain local stratification. Thus, the diapycnal mixing and effective WMT cannot be sustained over time.

In the three-dimensional simulations, two different restratification mechanisms have been found. Over the flanks of the mid-ocean ridge, submesoscale baroclinic eddies develop in response to the isopycnal tilting and they subsequently re-stratify the near-bottom fluid by releasing the available potential energy via buoyancy flux. This is consistent with the submesoscale baroclinic restratification by Callies (2018) and Wenegrat et al. (2018). Inside the ridge-flank canyons, however, a stronger stratification is maintained due to a large up-ridge mean flow that reaches more than 1 cm/s. The vertical structure of this up-ridge flow agrees with that in *in situ* observations. We propose the presence of submesoscale baroclinic eddies and their associated restratification outside of the BBL within the canyon, but they cannot be resolved due to the computational limitation in the current set-up. Lastly, a downwelling return flow is found to shift toward the canyon wall, instead of on top of the up-ridge flow, due to Earth's rotation.

As a consequence of the restratification in the three-dimensional simulations, turbulent buoyancy flux is sustained and thus a persistent convergence near the bottom of the ridge, resulting in a net lightening of the dense bottom water. WMT rates reach a quasi-equilibrium compared with the two-dimensional run. The net consumption of the densest bottom water over the 100 km wide mid-ocean ridge system is around 0.05 Sv, mounting to around 2 Sv in the entire Brazil Basin covering forty degrees in latitude. Surprisingly, the net contribution to bottom water consumption from inside the ridge-flank canyons is relatively small, due to the large cancellation in the strong upwelling and downwelling dipole.

We conclude that, in order to simulate the bottom water transformation in global numerical models and close the abyssal meridional overturning circulation, submesoscale baroclinic eddies in the abyss need to be better represented either with enhanced model resolution or with parameterizations, similar to those in the surface boundary layers. Although the ridge-flank canyons contribute little to the net bottom water consumption, they need to be included as local tracer (e.g. carbon and nutrient) pathways, as the upwelling and downwelling velocities are crucial for their advection and export.

Chapter 4

THE EVOLUTION AND ARREST OF A TURBULENT STRATIFIED OCEANIC BOTTOM BOUNDARY LAYER OVER A SLOPE: DOWNSLOPE REGIME

Ruan, Xiaozhou, Andrew F Thompson, and John R Taylor (2019). "The evolution and arrest of a turbulent stratified oceanic bottom boundary layer over a slope: Downslope regime". In: *Journal of Physical Oceanography* 49.2, pp. 469–487. DOI: `10.1175/JPO-D-18-0079.1`.

4.1 Abstract

The dynamics of a stratified oceanic bottom boundary layer (BBL) over an insulating, sloping surface depend critically on the intersection of density surfaces with the bottom. For an imposed along-slope flow, the cross-slope Ekman transport advects density surfaces and generates a near-bottom geostrophic thermal wind shear that opposes the background flow. A limiting case occurs when a momentum balance is achieved between the Coriolis force and a restoring buoyancy force in response to the displacement of stratified fluid over the slope: this is known as Ekman arrest. However, the turbulent characteristics that accompany this adjustment have received less attention. We present two estimates to characterize the state of the BBL based on the mixed layer thickness, H_a and H_L. The former characterizes the steady Ekman arrested state, and the latter characterizes a re-laminarized state. The derivation of H_L makes use of a newly-defined slope Obukhov length, L_s that characterizes the relative importance of shear production and cross-slope buoyancy advection. The value of H_a can be combined with the temporally-evolving depth of the mixed layer H to form a non-dimensional variable H/H_a, that provides a similarity prediction of the BBL evolution across different turbulent regimes. The length scale L_s can also be used to obtain an expression for the wall stress when the BBL re-laminarizes. We validate these relationships using output from a suite of three-dimensional large-eddy simulations. We conclude that the BBL reaches the re-laminarized state before the steady Ekman arrested state. Calculating H/H_a and H/H_L from measurements will provide information on the stage of oceanic BBL development being observed. These diagnostics may also help to improve numerical parameterizations of stratified BBL dynamics over sloping topography.

4.2 Introduction

In the abyssal ocean, enhanced shear and turbulence occurs in a thin region near the seafloor known as the oceanic bottom boundary layer (BBL). The BBL is an important source of drag on mean ocean currents and eddies, and plays a key role in global oceanic energy budgets (Wunsch and Ferrari, 2004). However, significant disagreement exists in estimates of the global energy dissipation in the BBL. Previous studies have estimated that energy dissipated in the BBL can range from 0.2 TW to as large as 0.83 TW (Wunsch and Ferrari, 2004; Sen et al., 2008; Arbic et al., 2009; Wright et al., 2013), which can be compared with the 0.8-0.9 TW of energy input from the wind into the geostrophic circulation (Wunsch and Ferrari, 2004; Scott and Xu, 2009). In addition to sparse observations, additional uncertainty in dissipation rates arises from a poor understanding of how stratification and bottom slopes combine to modify ocean flows over the seafloor.

Flow-topography interactions in the ocean may lead to the generation of meso-/submesoscale energetic turbulence (Gula et al., 2016) and internal gravity waves (Nikurashin and Ferrari, 2011). The BBL can thus be a site of enhanced dissipation and water mass transformation (Armi, 1978; Ruan et al., 2017). Contrary to classical arguments, e.g. Munk (1966), recent studies have suggested that BBLs over sloping topography are the primary locations for the upwelling of deep water needed to close the global overturning circulation (De Lavergne et al., 2016; Ferrari et al., 2016; De Lavergne et al., 2017). These arguments point to the BBL being the primary site of a convergent turbulent buoyancy flux needed to support diabatic upwelling.

However, due to the relatively small spatial scale of the BBL and practical difficulties associated with deep-sea observations, accurate representation of the oceanic BBL in large-scale general circulation models (GCM) remains challenging.

Stratified BBLs over a flat bottom have been extensively studied in both non-rotating and rotating systems, the latter known as the bottom Ekman layer (BEL). Direct numerical simulations (DNS) and large-eddy simulations (LES) have been carried out at different Reynolds numbers to study the structures of the BEL, Ekman transport, Ekman veering angle and their dependence on the external stratification. As external stratification increases, turbulence is suppressed and the BEL becomes thinner with a relatively unchanged depth-integrated transport (Coleman et al., 1990; Shingai and Kawamura, 2002; Taylor and Sarkar, 2008). The Ekman veering angle is reduced as compared with laminar theory, but the veering angle tends to increase with increasing external stratification in the lower part of the BEL (Taylor and Sarkar, 2008; Deusebio et al., 2014).

A sloping bottom boundary introduces additional dynamics. In a stratified BBL, the insulating bottom boundary condition causes density surfaces, or isopycnals, to tilt downslope in the absence of an along-slope mean flow. In steady state, an upslope convective flux is induced to balance the vertical buoyancy diffusion, as shown by Phillips (1970) and Wunsch (1970). In a rotating system, the tilting isopycnals also induce an along-slope geostrophic flow due to the thermal wind relation. When rotation is combined with an imposed along-slope mean flow, the near-bottom cross-slope Ekman transport is always smaller than in the flat bottom case. This is due to the opposing buoyancy force in the cross-slope direction. Isopycnals tilt either up- or down-slope depending on the orientation of the along-slope mean flow; in this study we only consider along-slope flows that induce down-slope Ekman transport. If the buoyancy force is sufficiently large to balance the Coriolis force in the cross-slope direction, the system arrives at a steady state with negligible Ekman transport. This is the so-called Ekman arrest (MacCready and Rhines, 1991), where the near-bottom velocity shear and thus the wall stress τ_w are also reduced compared to flat bottom cases. Here the wall stress is defined as:

$$\tau_w = \rho_0 \nu \left.\frac{\partial u}{\partial z}\right|_{z=0} = \rho_0 u_*^2, \tag{4.1}$$

where ρ_0 is a reference density, ν is the molecular viscosity, $u(z)$ is velocity parallel to the bottom, and u_* is the friction velocity. Critically, the steady Ekman-arrested state has not been observed in the ocean, despite efforts aimed at closing the integrated momentum and buoyancy budget in the BBL (Trowbridge and Lentz, 1998). Our results provide some insight into why observations of a steady Ekman arrest have been elusive.

Besides the steady state solutions introduced above, process studies have examined the time-dependent adjustment towards Ekman arrest. For studies that have not explicitly resolved turbulence in the BBL, typically one of two parameterizations is used. The first invokes a constant turbulent viscosity and diffusivity, which encapsulates the enhanced turbulent diffusion of momentum and buoyancy. Following early numerical studies by Weatherly and Martin (1978), MacCready and Rhines (1991) solved for an approximate Ekman arrest time scale τ_{laminar} for a laminar system and found τ_{laminar} depends on the slope Burger number Bu:

$$\tau_{\text{laminar}} = \frac{1}{S^2 f \cos\alpha}\left(\frac{1/\sigma + S}{1 + S}\right). \tag{4.2}$$

Here $S = Bu^2 = (N \sin\alpha / f \cos\alpha)^2$, where N and f are the buoyancy and Coriolis frequencies respectively, α is the slope angle and σ is the turbulent Prandtl number. The scale τ_{laminar} represents the time required for the cross-slope Ekman transport to arrive at the negligible steady state value $M_{\text{Thorpe}} = \kappa_\infty \cot\alpha$ derived by Thorpe (1987). Here, κ_∞ is the far-field diapycnal diffusivity, which is generally smaller than the BBL diffusivity where vigorous mixing takes place. During Ekman arrest, the stratified BBL over a slope becomes thicker than the BEL thickness, due to the diffusion of buoyancy into the interior. The analytical solutions in the case of constant viscosity and diffusivity pose a curious conclusion: the interior mean flow depends on background parameters, such as N and α. In other words, the interior velocity field is a part of the solution of the BBL system and cannot be viewed as a background forcing independent of BBL processes. By shaping the background mean flow, at least close to the ocean bottom, BBL dynamics may influence the interior circulation beyond classic Ekman spin-up and spin-down processes (Thomas and Rhines, 2002; Benthuysen and Thomas, 2013; Ruan and Thompson, 2016).

As an alternative to a constant turbulent viscosity and diffusivity, various parameterizations have been applied as closures of turbulent momentum and buoyancy fluxes, for example the simple bulk Richardson number R_b-dependent and higher order closure schemes. The latter includes the Mellor-Yamada schemes and the second-order closure implemented in a recent study examining the energy pathways in the Ekman arrest process (Umlauf et al., 2015). Trowbridge and Lentz (1991) have shown that a simple R_b-dependent parameterization is able to capture the general thickness evolution of the BBL as compared to the Mellor-Yamada level-two turbulence closure used in Weatherly and Martin (1978). Brink and Lentz (2010a) (hereafter BL10) have tested different turbulent closure schemes and provided more accurate empirical expressions for the time scales associated with the Ekman arrest process. However, the turbulent characteristics associated with the BBL evolution have not been examined closely in the two approaches introduced above. This has motivated us to carry out LES simulations, which directly resolve the largest turbulent motions that were parameterized in BL10. We will show that the BBL reaches a re-laminarized state in which turbulence is suppressed, before evolving to the final arrested state.

Describing the Ekman arrest process as a function of time is useful; however, ocean observations often do not fit neatly into this “initial value” approach. Determining the BBL’s time history, or the stage of the BBL’s turbulent evolution as it approaches the arrested state, remains difficult. Here, we provide a framework that both classifies and identifies various BBL stages, spanning fully-turbulent flat-bottom cases to Ekman arrested states, based on instantaneous bulk structures. A key motivation is that this framework will allow for more accurate parameterizations of BBL processes in GCMs. Our theoretical derivation, described in section 4.3, suggests that different BBL stages are associated with transitions in turbulent characteristics. Therefore, we use a suite of LES (section 4.4) to simulate a stratified oceanic BBL over a slope with a downwelling-favorable mean flow (Fig. 4.1) in order to explore these regime transitions and to validate the theoretical predictions (section 4.5). The mean momentum and buoyancy budgets are diagnosed in section 4.6; discussions and conclusions are provided in section 4.7. The goals of this study are threefold: (i) to quantify the effects of topographic slope and stratification on the BBL turbulent characteristics, as well as the wall stress, BBL thickness and Ekman transport; (ii) to describe the detailed structure of stratified BBL over a slope; and (iii) to propose a unified description of the evolution of stratified BBL over a slope throughout all stages towards full arrest.

4.3 Theoretical predictions

We begin by introducing two expressions for the height of the bottom mixed layer (BML), H_a and H_L, or the "arrest height" and "re-laminarization height," which can be determined from external parameters. In this study, the BML refers to the region of weak vertical stratification, whereas the BBL describes the region with enhanced dissipation, e.g. a *mixing* layer. We first re-visit a scaling for H_a proposed by Trowbridge and Lentz (1991). The second definition H_L is, to our knowledge, new and based on Monin-Obukhov similarity theory. These values of the arrest height will prove to be critical for describing not only the arrested state, but for classifying the approach to arrest, as shown in sections 4.5 and 4.6.

Momentum balance and arrest height

As shown in Fig. 4.1, the coordinate system is rotated such that x, y and z denote the down-slope, along-slope and slope-normal directions, respectively, and u, v and w are the corresponding velocity components. To leading order, the boundary layer momentum equation in the cross-slope direction is given by

$$\frac{\partial u}{\partial t} - f(v_{\text{total}} - \overline{v}) = -\alpha b - \frac{1}{\rho_0}\frac{\partial \tau^x}{\partial z}, \tag{4.3}$$

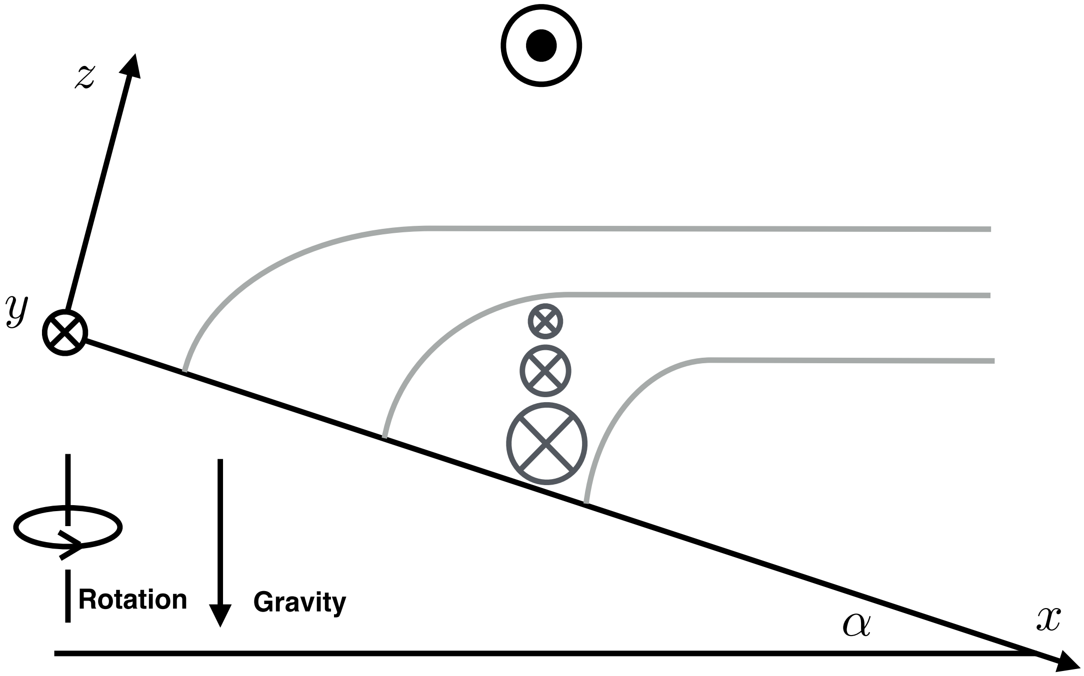

Figure 4.1: Schematic of the bottom boundary layer over a slope; gray curves indicated density surfaces. The coordinate is rotated by a slope angle α. The barotropic mean flow is associated with a downslope Ekman transport. The thermal wind shear generated due to the tilting isopycnals is in the positive y direction, opposite to the mean flow. The near-bottom velocity is the sum of the barotropic mean flow and the opposing thermal wind shear.

where v_{total} and $\overline{v}$ (with magnitude V_∞) are the total and far-field along-slope velocities and τ^x is the total stress (molecular and Reynolds). Scalings for the near-seafloor Coriolis force (per unit mass) F_C and buoyancy force (per unit mass) F_B that balance during Ekman arrest are

$$F_C \sim fV, \qquad F_B \sim \alpha b \sim \alpha^2 N_\infty^2 \Delta x \sim \alpha N_\infty^2 H, \tag{4.4}$$

where V is the magnitude of the boundary layer along-slope velocity. The buoyancy force is proportional to the displacement of the stratification. For a uniform slope, this is approximated using the cross-slope isopycnal displacement length scale Δx (Fig. 4.2), where $\Delta x \approx H/\alpha$ and H is the height of the BML where stratification is smaller than 30% of the background stratification N_∞^2. The extra slope angle α in the expression for F_B in (4.4) denotes the projection of an upward pointing buoyancy force onto the cross-slope direction. In the arrested state where the total near-bottom flow is weak, F_C and F_B balance and can be expressed as:

$$F_C^{\text{arrest}} = fV_\infty, \qquad F_B^{\text{arrest}} \approx \alpha N_\infty^2 H_a. \tag{4.5}$$

This yields an expression for the arrest height H_a:

$$H_a \approx fV_\infty/(\alpha N_\infty^2). \tag{4.6}$$

The same expression was proposed by Trowbridge and Lentz (1991) by assuming that the thermal wind shear $v_z = -\alpha N_\infty^2/f$ brings the total flow magnitude from the far-field value V_∞ to zero near the bottom. This indicates that increasing the slope angle and stratification and/or reducing the mean flow magnitude leads to a reduction in the cross-slope displacement of the stratified fluid required to achieve Ekman arrest, or equivalently a reduction in H_a. Using $f = 10^{-4}$ s^{-1} and typical abyssal oceanic parameters: $V_\infty = 0.05$ m s^{-1}, $N_\infty^2 = 10^{-6}$ s^{-2} and $\alpha = 0.005$, H_a must be roughly 1000 m to generate a sufficiently large buoyancy force to balance the Coriolis force. This large value may partially explain why Ekman arrest is rarely observed in the abyssal ocean. However, for typical values over the continental slope where the pycnocline intersects topography: $V_\infty = 0.05$ m s^{-1}, $N_\infty^2 = 10^{-5}$ s^{-2} and $\alpha = 0.01$, an $H_a \approx 50$ m may be sufficient to achieve Ekman arrest.

Predictions for H_a vary by four orders of magnitude across typical oceanic parameters (Fig. 4.3 a-c). The nonlinear dependence of H_a on different parameters warrants careful examination of BBL structures in different regimes, which is the focus of section 4.5.

Turbulent characteristics and re-laminarization height

An alternative definition of an arrest height begins by assuming that a complete balance between buoyancy and Coriolis forces requires the suppression of turbulence and turbulent stress. The competition between shear production and buoyancy flux can be characterized by the Obukhov length scale, which is defined by:

$$L \equiv \frac{-u_*^3}{kB}, \tag{4.7}$$

where $k = 0.41$ is the von Karman constant and B is the surface buoyancy flux. For an unstable BBL where the buoyancy flux is upward ($B > 0$), the Obukhov length scale L is negative, and it characterizes the relative importance of surface stress and convection in the production of turbulence. For a stable BBL, where the buoyancy

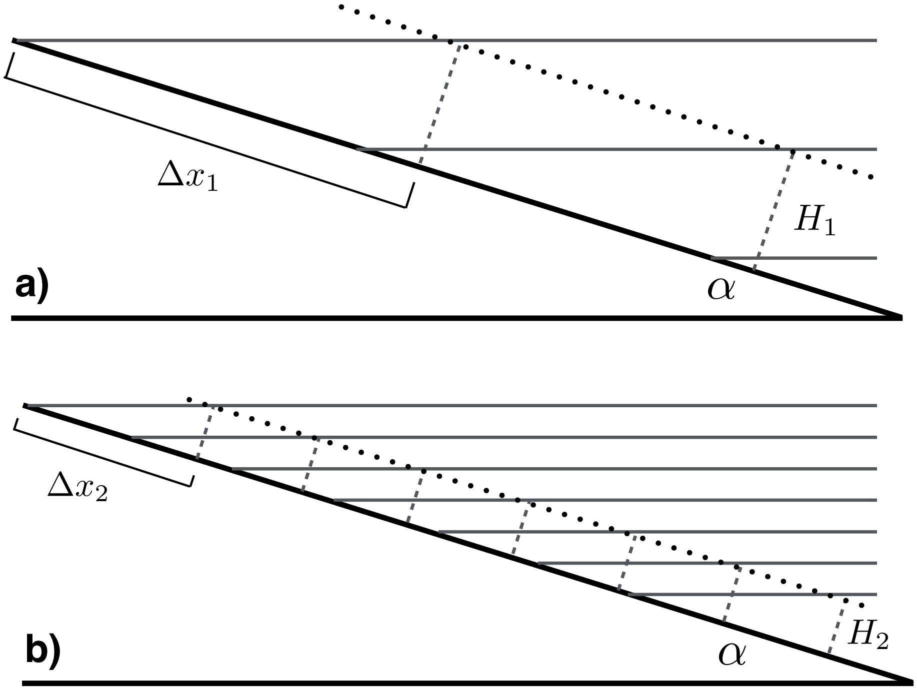

Figure 4.2: Schematic of the arrest height H_a in sloping BBLs with different stratifications. The dashed lines represent the isopycnals in the BML after they are advected downslope. The dotted lines denote the top of the BML. For the same slope angle α and mean flow magnitude V_∞, fluid with stronger stratification N_∞^2 requires a smaller H_a to generate a buoyancy force to balance the Coriolis force (fV_∞) in the cross-slope direction. Here, $\Delta x_1 N_1^2 = \Delta x_2 N_2^2$, so $H_1/H_2 = N_2^2/N_1^2$. N^2 and H are the background stratification and arrest height associated with a weakly and a strongly stratified BBL (subscripts 1 and 2, respectively).

flux is downward ($B < 0$), L is positive, and it corresponds to the transition depth (height above bottom) at which the stabilizing influence of stratification begins to suppress turbulence.

In the absence of a buoyancy flux at the wall in the oceanic BBL, (4.7) can be revised by replacing B with the depth-integrated cross-slope buoyancy advection, which results in a new length scale, here called the "slope Obukhov length":

$$L_s \equiv \frac{u_*^3}{kUN_\infty^2\alpha}, \tag{4.8}$$

where $U = \int_0^\infty u dz$ is the depth-integrated cross-slope transport. We show, using LES simulations, that the ratio of H to L_S captures the transition of the BBL from

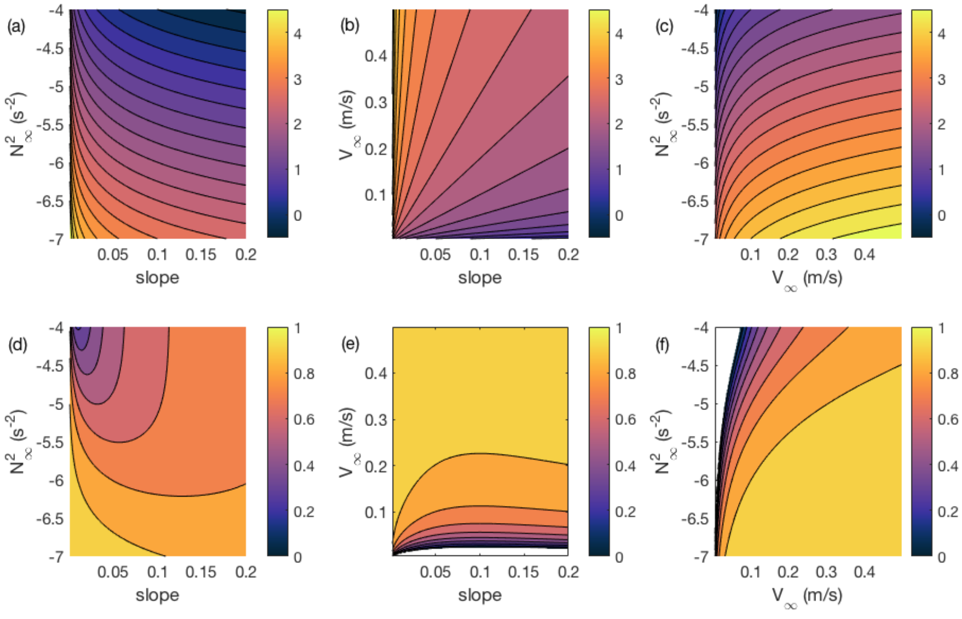

Figure 4.3: The predicted arrest height H_a (m) (panel a-c, logarithmic scale, e.g. 1 = 10 m for H_a) and the ratio H_L/H_a (panel d-f) as a function of slope angle α, background stratification N^2_∞ and mean flow magnitude V_∞. Estimates of H_a and H_L are based on the mean momentum balance (4.6) and turbulent characteristics (4.14 with $C_d = 2 \times 10^{-3}$), respectively. The parameters that are held fixed for different cases are: (a,d) $V_\infty = 0.01$ m s^{-1}; (b,e) $N^2_\infty = 10^{-6}$ s^{-2}; (c,f) $\alpha = 0.01$.

unstable to stable states and finally to an Ekman arrested state (section 4.5). The dependence of L_s on U can be removed by relating the steady state Ekman transport over a slope to the friction velocity (Brink and Lentz, 2010a):

$$U = u_*^2/f(1 + Bu^2), \tag{4.9}$$

such that

$$L_s = (1 + Bu^2)\frac{f u_*}{k\alpha N^2_\infty}. \tag{4.10}$$

It has been shown that the non-dimensional viscous Obukhov length $L^+ = Lu_*/\nu$ controls the turbulent state in stratified atmospheric boundary layers, such that for $L^+ < 100$ turbulence collapses and the boundary layer re-laminarizes (Flores and Riley, 2011). The Obukohv length, L characterizes the depth over which turbulence generation is unaffected by stratification and $100\nu/u_*$ roughly denotes the upper limit of the viscous wall region (including both the viscous sublayer, the buffer layer and part of the lower log-law layer). Thus, $L < 100\nu/u_*$ implies that turbulence suppression by stratification has penetrated into the viscous wall region, which results in turbulence collapse.

The physical interpretation of the slope Obukhov length L_s is the same as the Obukhov length L. Assuming that turbulence in the oceanic BBL also collapses when the viscous slope Obukhov length,

$$L_s^+ = L_s u_*/\nu = (1 + Bu^2) f {u_*}^2 / (\nu k \alpha N_\infty^2), \tag{4.11}$$

falls below a critical value C, the squared friction velocity associated with the transition from a turbulent to a re-laminarized state is:

$$(u_*)^2 = C \frac{\nu k \alpha N_\infty^2}{f\left(1 + Bu^2\right)}. \tag{4.12}$$

When the friction velocity becomes smaller than the value predicted in (4.12), the BBL will transition to a laminar state. In section 4.5 we show that the critical value for the constant C in these simulations is also around 100. Accounting for the reduction in the near-bottom, along-slope velocity due to the thermal wind shear, the revised expression for the wall stress using the quadratic law is

$$\tau_w^y/\rho_0 = C_d V_b^2 = C_d (V_\infty - \alpha N_\infty^2 H/f)^2, \tag{4.13}$$

where C_d is the drag coefficient and V_b is the near-bottom flow magnitude. An expression for the re-laminarization height is then given by

$$H_L = \frac{f V_\infty}{\alpha N_\infty^2} - \left(\frac{C k \nu f}{\alpha N_\infty^2 C_d (1 + Bu^2)}\right)^{1/2}, \tag{4.14}$$

a threshold for the BML thickness above which the BBL re-laminarizes.

The scaling for H_a in (4.6) is recovered when the second term in (4.14) is small, e.g. when the wall stress is negligible. When the BBL reaches the re-laminarized state, the BML thickness H_L is always smaller than the predicted H_a for steady Ekman arrest. The scales H_a and H_L become more similar for small α, weak N^2 and strong V_∞ (Fig. 4.3 d-f). Once the BBL is re-laminarized, the only mechanism for further evolution to the final arrested state is via molecular diffusion. However, ubiquitous background perturbations are likely to make the re-laminarized state difficult to sustain, providing another explanation for why a steady Ekman arrested state has not been observed.

In our LES simulations, we focus on BBL re-laminarization, which, we believe, is of more oceanic relevance than the Ekman arrested state. We also note that both H_a

and H_L are likely underestimated compared with the true BML thickness because of two assumptions. First, we assume that the tilted isopycnals can be represented by straight lines (Fig. 4.2). In reality, the isopycnals tilt smoothly towards the bottom, which yields a larger H_a at steady state. Second, V_b is defined at the bottom of the thermal layer rather than at $z = 0$. Thus, we do not account for the thickness of the viscous layer in H_a, including the viscous sublayer, the buffer layer and the lower part of the log layer.

4.4 Numerical methods

In the remainder of the paper, we show that the ratio of the mixed layer depth H to H_L is an important parameter for predicting re-laminarization of the BBL over a slope, whereas the ratio of H to H_a describes the evolution of the BBL across a range of turbulent regimes towards complete arrest. The dependence of H_L on small-scale turbulent properties of the BBL motivates the use of LES simulations, described below.

Governing equations

The LES-filtered Navier-Stokes equations under the Boussinesq approximation in a rotating frame can be written in dimensional form as:

$$\frac{\partial u}{\partial t} + \mathbf{u}\cdot\nabla u - fv\cos\alpha = -\frac{1}{\rho_0}\frac{\partial p'_d}{\partial x} - b\cdot\sin\alpha + \nu\nabla^2 u - \partial_j \tau^d_{1j}, \tag{4.15}$$

$$\frac{\partial v}{\partial t} + \mathbf{u}\cdot\nabla v + f(u\cos\alpha - w\sin\alpha) = -\frac{1}{\rho_0}\frac{\partial p'_d}{\partial y} + \nu\nabla^2 v - \partial_j \tau^d_{2j}, \tag{4.16}$$

$$\frac{\partial w}{\partial t} + \mathbf{u}\cdot\nabla w + fv\sin\alpha = -\frac{1}{\rho_0}\frac{\partial p'_d}{\partial z} + b\cdot\cos\alpha + \nu\nabla^2 w - \partial_j \tau^d_{3j}, \tag{4.17}$$

$$\frac{\partial b}{\partial t} + \mathbf{u}\cdot\nabla b - N_\infty^2(u\sin\alpha + w\cos\alpha) = \kappa\nabla^2 b - \nabla\cdot\lambda^d, \tag{4.18}$$

$$\nabla\cdot\mathbf{u} = 0. \tag{4.19}$$

Here ν and κ are the molecular viscosity and diffusivity, respectively; $N_\infty^2 = -\frac{g}{\rho_0}\frac{d\rho}{dz}$ is the background (non-evolving) stratification; $b = -g\rho'/\rho_0$ is buoyancy where ρ' is the density deviation from the background stratification; p'_d denotes the pressure deviation from the background hydrostatic balance, which has been removed from (4.17); τ^d and λ^d are the subgrid-scale (SGS) stress (with 1, 2 and 3 representing the x, y and z directions) and buoyancy flux, respectively, which require SGS models for closure. The equations of motion are in a reference frame moving with the along-slope mean flow $\overline{v}$, with magnitude V_∞. Therefore (4.16) gives the evolution of the perturbation velocity v where $v = v_{\text{total}} - \overline{v}$, and $\overline{v} = -V_\infty$ for downslope Ekman transport conditions.

The dimensional variables are non-dimensionalized using:

$$(u, v, w) = u_*(u', v', w'), \qquad (x, y, z) = \delta(x', y', z') = u_*/f(x', y', z'), \tag{4.20}$$

$$p'_d = \rho_0 u_*^2 p', \qquad b = N_\infty^2 \delta\, b', \qquad t = \delta/u_* t'. \tag{4.21}$$

The resulting non-dimensional equations (with primes dropped except for the pressure deviation) are:

$$\tfrac{\partial u}{\partial t} + \mathbf{u} \cdot \nabla u - v \cos\alpha = -\tfrac{\partial p'}{\partial x} + Ri_* b \sin\alpha + Re_*^{-1} \nabla^2 u - \partial_j \tau_{1j}, \tag{4.22}$$

$$\tfrac{\partial v}{\partial t} + \mathbf{u} \cdot \nabla v + (u \cos\alpha - w \sin\alpha) = -\tfrac{\partial p'}{\partial y} + Re_*^{-1} \nabla^2 v - \partial_j \tau_{2j}, \tag{4.23}$$

$$\tfrac{\partial w}{\partial t} + \mathbf{u} \cdot \nabla w + v \sin\alpha = -\tfrac{\partial p'}{\partial z} + Ri_* b \cos\alpha + Re_*^{-1} \nabla^2 w - \partial_j \tau_{3j}, \tag{4.24}$$

$$\tfrac{\partial b}{\partial t} + \mathbf{u} \cdot \nabla b - (u \sin\alpha + w \cos\alpha) = Re_*^{-1} Pr^{-1} \nabla^2 b - \nabla \cdot \lambda, \tag{4.25}$$

$$\nabla \cdot \mathbf{u} = 0. \tag{4.26}$$

Three non-dimensional parameters govern the system: the friction Reynolds number Re_*, friction Richardson number Ri_* and Prandtl number Pr, where,

$$Re_* = \frac{u_* \delta}{\nu} = \frac{u_*^2}{f\nu}, \qquad Ri_* = \frac{N_\infty^2 \delta^2}{u_*^2} = \frac{N_\infty^2}{f^2}, \qquad Pr = \frac{\nu}{\kappa}. \tag{4.27}$$

Relevant non-dimensional parameters used in the experiments are listed in Table 1. The parameters are chosen to explore their controls on the Ekman arrest process, ranging from a near flat-bottom and unstratified limit to an experiment with the fastest arrest allowed in the model. The friction velocity u_* that appears in the non-dimensional parameters does not include the effects of stratification, i.e. u_* is the friction velocity before stratification is introduced (see discussion in section 4.4). The equations are solved subject to no-slip and insulating boundary conditions:

$$v = V_\infty, \qquad z = 0, \tag{4.28}$$

$$u = w = 0, \qquad z = 0, \tag{4.29}$$

$$\frac{\partial b}{\partial z} + N_\infty^2 = 0, \qquad z = 0. \tag{4.30}$$

The far-field boundary conditions are free-slip and insulating for the momentum and buoyancy equations. Again, the bottom boundary condition is set to ensure $v_{\text{total}} = 0$. Throughout, the small angle approximation ($\sin\alpha \approx \alpha$ and $\cos\alpha \approx 1$) is applied.

Numerical details

The simulations are performed using the computational fluid dynamics solver, DIABLO. Details of the numerical method can be found in Taylor (2008) and Bewley (2012). The background cross-slope density gradient remains constant ($M_\infty^2 = -\alpha N_\infty^2$) throughout the adjustment, determined by the sloping topography cutting through the vertically-stratified fluid; there is no along-slope density gradient. The model solves for density perturbations to the background stratification. Thus, periodic boundary conditions are used in the x and y directions with uniform grid spacing and the derivatives in these two directions are computed with a pseudospectral method (de-aliased using the 2/3 rule). Staggered and stretched grids are used in the slope-normal direction with finer grid spacing close to the upper and lower boundaries. Derivatives in the slope-normal direction are treated with second-order finite differences. The time-stepping algorithm uses a mixed third-order Runge-Kutta/Crank-Nicolson method.

In order to examine the impact of finite stratification on the dynamics close to the wall, the LES experiments performed here are run with near-wall resolution (LES-NWR), also called a resolved LES, which resolves at least 80% of the energy in the flow (Pope, 2001; Sagaut, 2006). Near the wall, turbulent motions scale with the viscous length $\delta_\nu = \nu/u_*$, which places strong constraints on the model resolution. We placed the first two grid points in the viscous layer $z^+ < 5$ and the minimum resolution in the slope-normal direction is $\Delta_z^+ = 2$; in dimensional units $\Delta_z = 2\nu/u_*$. The uniform grid spacing in the slope-parallel directions are $\Delta_x^+ = \Delta_y^+ \sim 20$. The domain size is 30 m (L_x) × 30 m (L_y) × 60 m (L_z), respectively. A sponge layer of thickness 10 m is placed at the top of the domain to avoid reflection of internal gravity waves generated from the interaction of BBL turbulence with the pycnocline.

The background stratification can suppress the initialization of a turbulent BEL. To focus on the turbulent state, as opposed to the transition to a turbulent state, the simulations are spun up in multiple stages. First, an unstratified simulation is conducted with linear damping added to the momentum equations in the x and y directions until the system reaches quasi-equilibrium; the uniform damping rate is half of the inertial frequency f. This stabilizes the flow and reduces inertial oscillations. The linear damping is then removed, allowing the flow to adjust to the background environment. Finally, a stable background stratification is incorporated into the simulation with a thin BML (2-3 m) near the bottom to ensure the viscous sublayer is unaffected by the stratification at the start (see an example initial stratification profile for $N_\infty^2 = 10^{-5}\mathrm{s}^{-2}$ in Fig. 4.4). The strongest stratification used in these experiments is $N_\infty^2 = 10^{-5}\mathrm{s}^{-2}$.

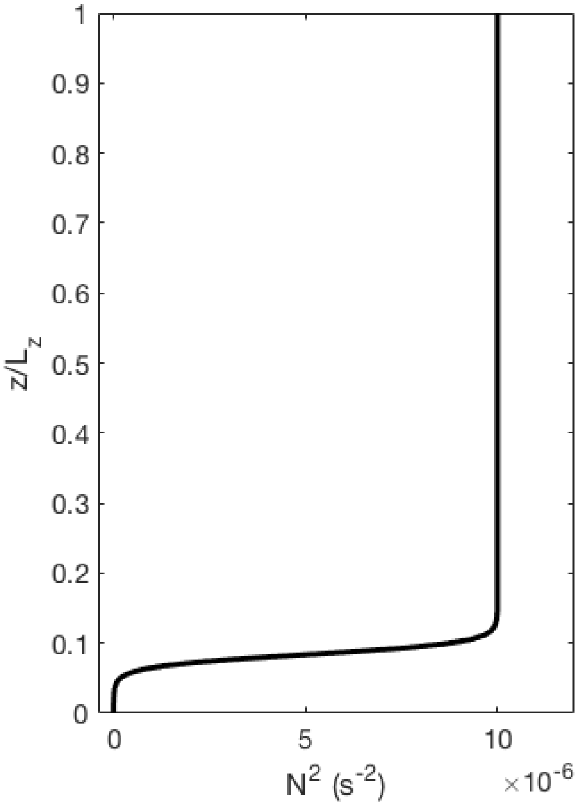

Figure 4.4: An example initial stratification profile for $N_\infty^2 = 10^{-5}\mathrm{s}^{-2}$; $L_z = 60$ m is the height of the domain. A thin mixed layer (~ 2 m) is constructed to avoid the direct impact of stable stratification on the transition to turbulence in the BBL.

The LES-filtered governing equations are essentially a low-pass filtered version of the Navier-Stokes equations with the resolved velocity field used to determine the SGS stress tensor $\tau_{i,j}^{SGS}$. Similar to the SGS model used by Taylor and Ferrari (2010), a constant Smagorinsky model was used in the simulations,

$$\tau_{i,j}^{SGS} = -2C^2\overline{\Delta}^2|\overline{S}|\overline{S}_{i,j}. \tag{4.31}$$

Here $C = 0.13$ is the Smagorinsky coefficient, $\overline{\Delta} = (\Delta_x\Delta_y\Delta_z)^{1/3}$ is the implicit LES filter width and $S_{i,j}$ is the rate of strain tensor. The overbar denotes the filtered (or resolved) field. The SGS eddy viscosity from the Smargorinsky model is calculated as $\nu_{SGS} = C^2\overline{\Delta}^2|\overline{S}|$ with the constant molecular viscosity explicitly used in the resolved field. A constant SGS Prandtl number $Pr_{SGS} = \nu_{SGS}/\kappa_{SGS} = 1$ is used to calculate the SGS eddy diffusivity.

4.5 Identification of turbulent regimes from large-eddy simulations

A series of experiments were conducted to examine how topographic slope (α), stratification (N_∞) and background flow (V_∞) impact the evolution and bulk structures of the BBL. Table 4.1 provides the slope Burger number Bu, initial friction Reynolds number Re_* and friction Richardson number Ri_*, and the Prandtl number Pr. The ratios, H/H_a and H/H_L, at the end of each simulation, are also given. These experiments span a range of turbulent states, including some that are far from re-laminarization.

Table 4.1: Summary of the simulation parameters. The slope Burger number $Bu = N \sin\alpha / f \cos\alpha$, and other non-dimensional parameters Re_*, Ri_* and Pr are defined in (4.27). The values for E_a and E_L are given for the end of each experiment, $t_{\text{end}}f$.

Expt.	α	$\log_{10} N_\infty^2(\text{s}^{-2})$	$V_\infty(\text{ms}^{-1})$	Bu	Re_*	Ri_*	Pr	E_a	E_L	$t_{\text{end}}f$
A	0.005	-7	0.1	0.016	4232	10	5	0.002	0.002	53.84
B	0.01	-6.5	0.1	0.056	4232	31.6	5	0.014	0.015	48.16
C	0.01	-6	0.1	0.1	4232	100	5	0.041	0.046	40.73
D	0.01	-5.5	0.1	0.178	4232	316	5	0.130	0.157	43.95
E	0.01	-5	0.1	0.316	4232	1000	5	0.349	0.492	40.08
F	0.02	-5	0.1	0.632	4232	1000	5	0.772	1.215	55.14
G	0.01	-6	0.05	0.1	1352	100	5	0.058	0.070	65.95
H	0.01	-5	0.05	0.316	1352	1000	5	0.503	1.060	116.59

Given sufficient time and water column depth, the adjustment of a stratified fluid over sloping topography is always towards the steady Ekman arrested state; the time to reach this state depends on external parameters. For experiments across a wide range of conditions, the non-dimensional parameters $E_a = H/H_a$ and $E_L = H/H_L$, which represent the extent to which the BBL has approached the arrested and re-laminarized states, can be used to classify different BBL dynamical regimes. Indeed, E_a is equivalent to the ratio between the buoyancy and Coriolis force,

$$E_a = H/H_a = \alpha N_\infty / f \cdot N_\infty H / V_\infty = Bu/Fr \approx F_B/F_C, \tag{4.32}$$

where $Fr = V_\infty/(N_\infty H)$ is the Froude number. Thus, the magnitude of E_a serves as a measure of the extent towards Ekman arrest, *e.g.* when $E_a \ll 1$, the BBL is far from the arrested state. Since the slope Burger number Bu in the ocean rarely exceeds unity, (4.32) implies that supercritical flows ($Fr > 1$) are almost alway far from arrest. Similarly, we can define

$$E_L = H/H_L, \tag{4.33}$$

where H_L is defined based on the critical viscous slope Obukhov length. Thus $E_L = 1$ and $L_s^+ = 100$ will be used interchangeably later to indicate a re-laminarized state. Below we discuss four sequential stages as the BBL evolves towards the steady arrested state: (i) weakly buoyant regime ($E_a \approx 0$ and $E_L \approx 0$); (ii) buoyant regime ($0 < E_a < 1$ and $0 < E_L < 1$); (iii) re-laminarized regime ($0 < E_a < 1$ and $E_L = 1$) and (iv) Ekman arrested regime ($E_a = 1$ and $E_L > 1$). A summary of the different regimes can be found in Fig. 4.5.

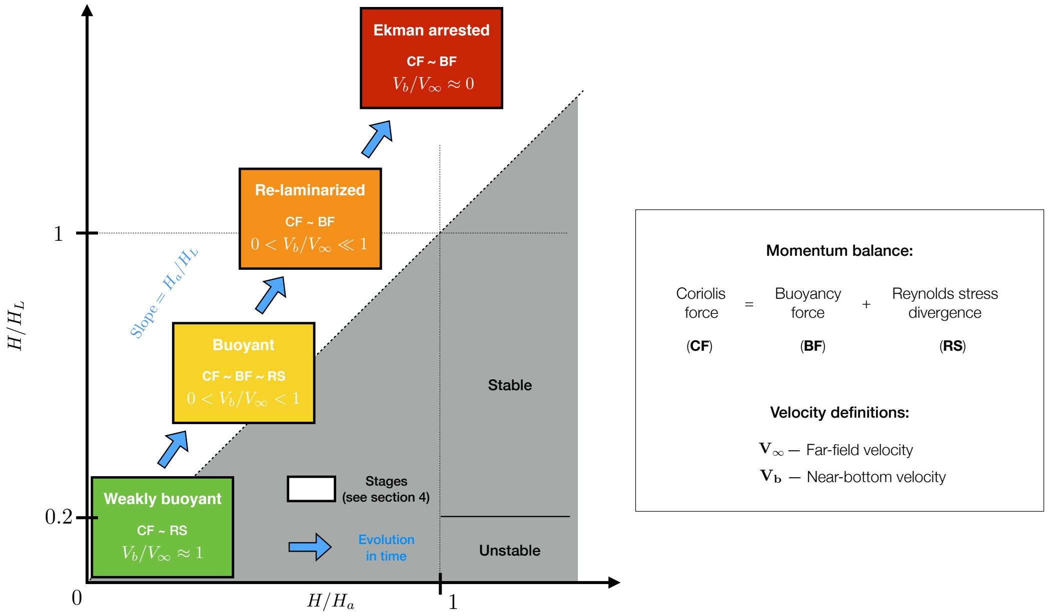

Figure 4.5: Schematic representing the stages (boxes) in the approach to Ekman arrest; see discussion in section 4.5. The axes are the non-dimensional numbers $E_a = H/H_a$ and $E_L = H/H_L$ defined in section 4.5. Each box summarizes the leading order terms in the momentum balance and the ratio of far-field to near-bottom velocities, following the legend to the right.

To highlight differences between these stages, we focus on the following properties: vertical stratification, the vertical velocity profiles within the BBL, cross-slope transport and the friction velocity used to determine the wall stress. We discuss the connection between the newly-proposed non-dimensional parameters and turbulent characteristics in the BBL through the classic Monin-Obukhov similarity theory in section 4.5.

During all of these experiments, H is continuously changing with time. The growth rates of the BML are well described by power law relationships $H \sim t^b$, although the exponent b varies between different simulations (Fig. 4.6). The exponents fall between two limits. For the smallest initial Bu, the convection is weak and BML growth follows a 2/9 power law, consistent with stress-driven mixed layer growth

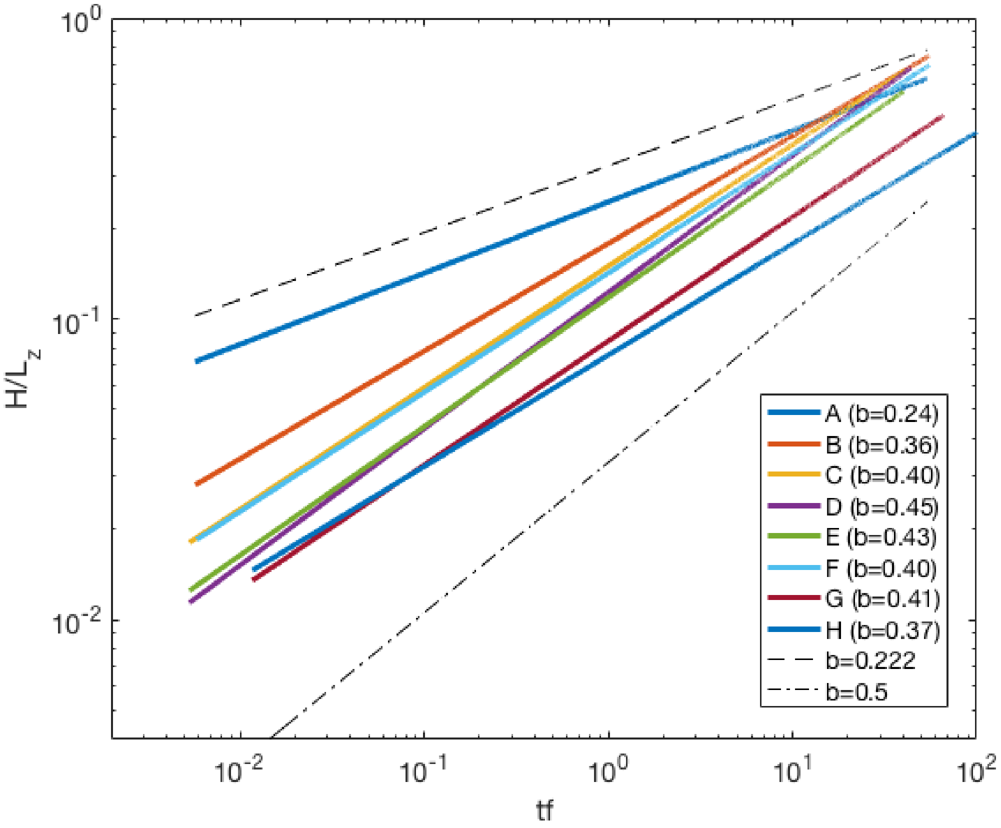

Figure 4.6: The growth of the BML with time: $H/L_z \sim (tf)^b$. Different colors represent different simulations given in Table 4.1. The dashed and dash-dot lines represent the reference power laws of the stress ($b = 2/9$) and upright convection-driven ($b = 1/2$) BBL growth rates, respectively.

(Manucharyan and Caulfield, 2015). For larger values of Bu, BML growth follows a $1/2$ power law, consistent with a classic upright convection-driven mixed layer development (Deardorff et al., 1969). For the large Bu experiments, the sloping topography allows for larger downslope advection of buoyant fluid under heavier fluid that leads to the transition to stronger convective mixing. The simulated BML thickness is, overall, comparable to those in models that have used one-dimensional turbulence closure techniques. However, one-dimensional turbulence closure models largely account for turbulence production due to gravitational or Kelvin–Helmholtz instabilities in the bulk BBL and do not represent shear production at the wall (in the viscous sublayer). Additional analysis is needed to evaluate one-dimensional turbulence closures in simulating the Ekman arrest process.

Finally, to diagnose the vertical structure of velocity and other variables in the LES, a time average is applied over one near-inertial period to remove the effect of near-inertial oscillations. The centers of the averaging windows are labeled in Fig. 4.8 and indicated in Fig. 4.9 by the vertical dashed lines; the same average is applied in the figures shown below unless otherwise noted.

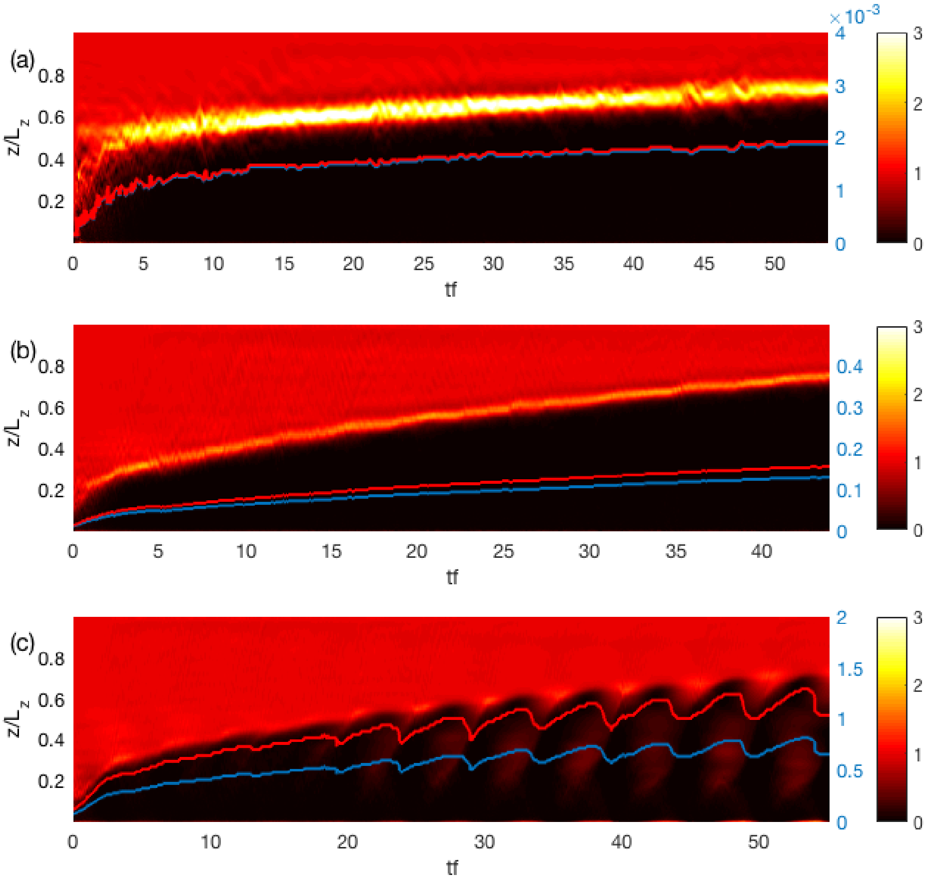

Figure 4.7: Temporal evolution of the plane-averaged stratification N^2/N_∞^2 in experiments A (a), D (b) and F (c), corresponding to initial values of Bu of 0.016, 0.178 and 0.632, respectively. The evolution of the non-dimensional parameters E_a and E_L are given by the blue and red curves, with the corresponding axis on the right in blue.

Weakly buoyant regime, $E_a \approx 0$ and $E_L \approx 0$

When the thickness of the BBL is small, *i.e.*, $E_a \approx 0$ and $E_L \approx 0$, the dynamics of the BBL are similar to those described in studies of stratified BBL over a flat bottom (Taylor and Sarkar, 2008; Deusebio et al., 2014). In this regime, the buoyancy force F_B is weak in the cross-slope momentum balance (4.3). Experiments with a gentle slope, a weak stratification or a large mean flow all have large values of H_a and H_L, and our LES experiments remain in the $E_a \approx 0$ and $E_L \approx 0$ regime throughout their duration (table 4.1). Note, though, that all simulations pass through this stage at early times since $H \approx 0$ when the simulations are initialized.

In this stage, a strongly-stratified pycnocline caps the BML. For instance, in Experiment A, the stratification in the pycnocline is three times larger than the background value (Fig. 4.7a). Furthermore, the vertical structure of the horizontal velocity and veering angle through the BBL agree with flat bottom Ekman layer dynamics (Figs. 4.8 and 4.9a). After an initial adjustment, the cross-slope transport and friction velocity are relatively steady over the course of the simulations (Figs. 4.9b and 4.10a); both U and u_* decrease as E_a increases (Figs. 4.10b and 4.11).

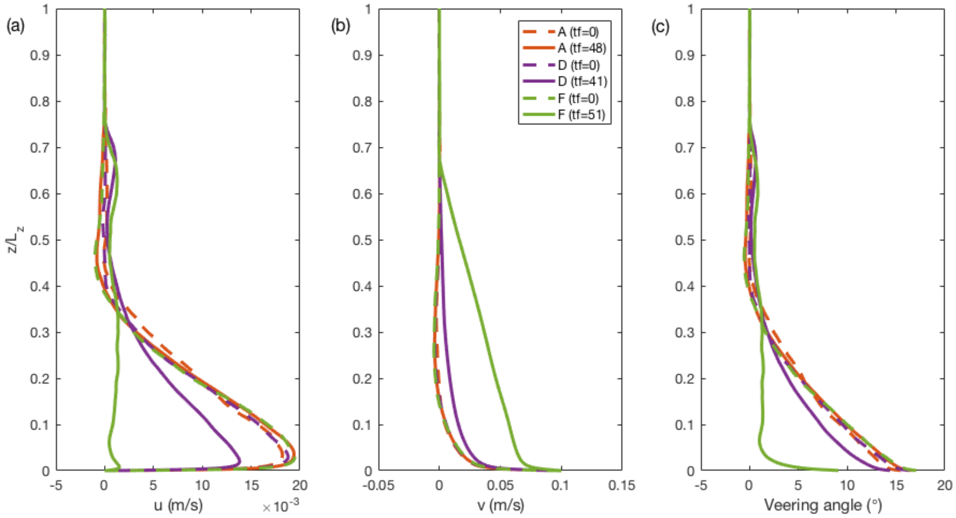

Figure 4.8: The plane-averaged (a) cross-slope velocity, (b) along-slope velocity, and (c) Ekman veering angle at the beginning (dashed) and late stage (solid) of experiments A, D and F. The centers of the averaging windows are provided in panel (b), and correspond to the vertical dotted lines in Fig. 4.9 (a, c, e). The along-slope velocity satisfies the no-slip boundary condition with the addition of $\overline{v} = -V_\infty = -0.1 \text{ m s}^{-1}$.

Buoyant regime, $0 < E_a < 1$ **and** $0 < E_L < 1$

As H grows, the importance of the buoyancy force F_B in the cross-slope momentum equation begins to modify the characteristics of the BBL. In experiments with larger (initial) values of Bu, the stratification in the pycnocline at the top of the BML is weaker (Fig. 4.7b) during this stage. This occurs because a more steeply-sloping

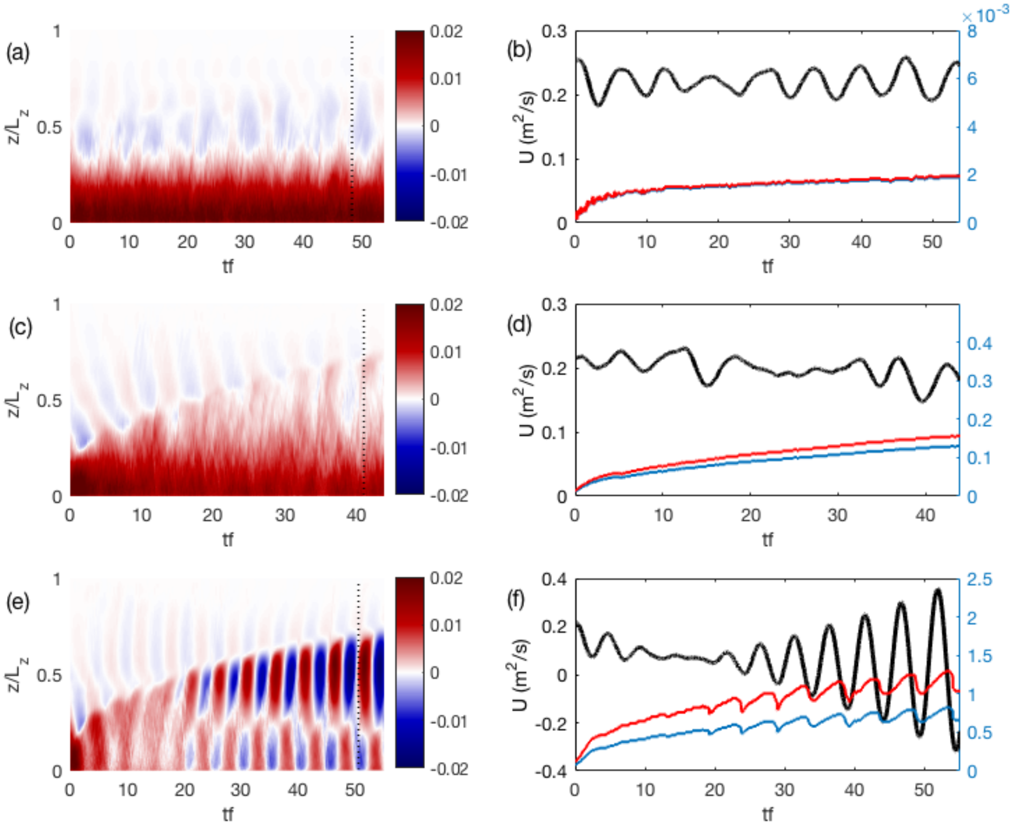

Figure 4.9: The evolution of cross-slope velocity (m s^{-1}) (a,c,e) and depth-integrated transport U (m^2 s^{-1}) (b,d,f) for simulations A (a,b), D (c,d) and F (e,f). The corresponding E_a and E_L for each simulation are shown in blue and red curves in the transport panels, respectively, with the corresponding axis on the right in blue. The vertical dotted lines in the cross-slope velocity panels represent the centers of the time-averaging windows (of a near-inertial period) used to generate the vertical structures of the velocity variables and other components in the momentum and buoyancy budgets.

bottom or a stronger stratification causes buoyancy transfer to transition from being in the vertical direction to being primarily in the cross-slope direction. This weakens the tendency to form a pycnocline (see also the buoyancy budget in section 4.6). This behavior may partially explain why the top of the BML in the ocean is not typically associated with a strong pycnocline (Armi, 1978; Ruan et al., 2017).

As E_a and E_L become larger than 0.1, the cross-slope velocity profile penetrates deeper into the water column (Figs. 4.8a and 4.9c), the cross-slope transport decays (Fig. 4.9d), and the friction velocity decreases (Fig. 4.10a), all as compared to the

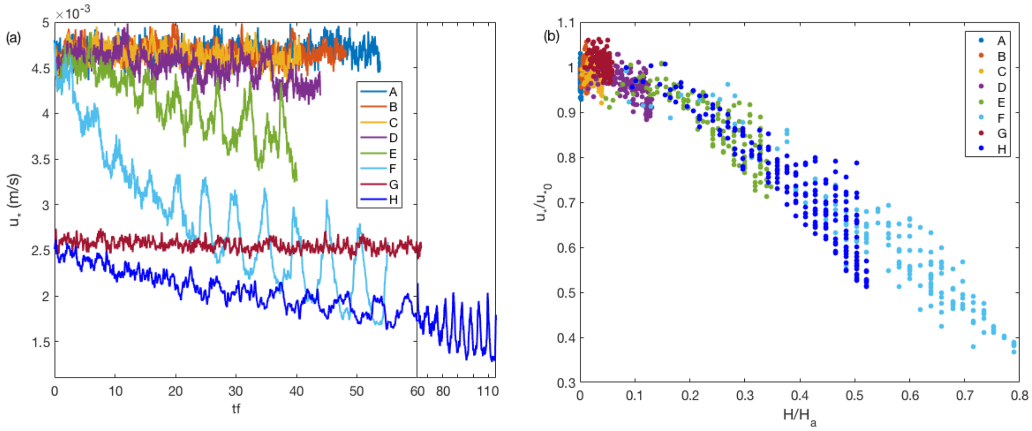

Figure 4.10: (a) The evolution of friction velocity u^* (m s^{-1}) as a function of time. (b) The evolution of friction velocity u_*, non-dimensionalized by the initial friction velocity u_{*0}, as a function of $E_a \equiv H/H_a$. Different colors represent different simulations in Table 4.1.

weakly buoyant regime (section 4.5). In this regime, the deflection of isopycnals in the Ekman layer generates a thermal wind shear that opposes the along-slope velocity (Fig. 4.8b). This in turn reduces the velocity shear at the bottom, which leads to a smaller wall stress and friction velocity. Finally, the veering angle near the bottom decreases in response to the reduced wall stress, resulting in a smaller degree of turning of the along-slope flow, consistent with a weaker Ekman transport (Fig. 4.8c). While the veering angle is reduced, the thickness of the "veering layer" increases. This occurs because the thermal wind shear penetrates deeper than the Ekman layer. The Coriolis force F_C then deflects the along-slope momentum into the cross-slope direction. This penetration of along-slope momentum is not entirely due to turbulent diffusion, but involves the build-up of the thermal wind shear—this is the "slow diffusion" process discussed by MacCready and Rhines (1991).

For all simulations, both u_* and U collapse onto a single curve when plotted against E_a (Figs. 4.10b and 4.11). As F_B strengthens as compared to F_C, u_* decreases linearly with E_a. While U also decreases with increasing E_a, this modification is not linear in E_a due to the quadratic relationship given in (4.9).

Re-laminarized regime, $0 < E_a < 1$ **and** $E_L = 1$

For experiments where E_a approaches 1 but $E_L \approx 1$, the BBL dynamics enter a state that we refer to as a re-laminarized stage; the distinction between this state and the arrested state has not previously been documented. The re-laminarized stage can be

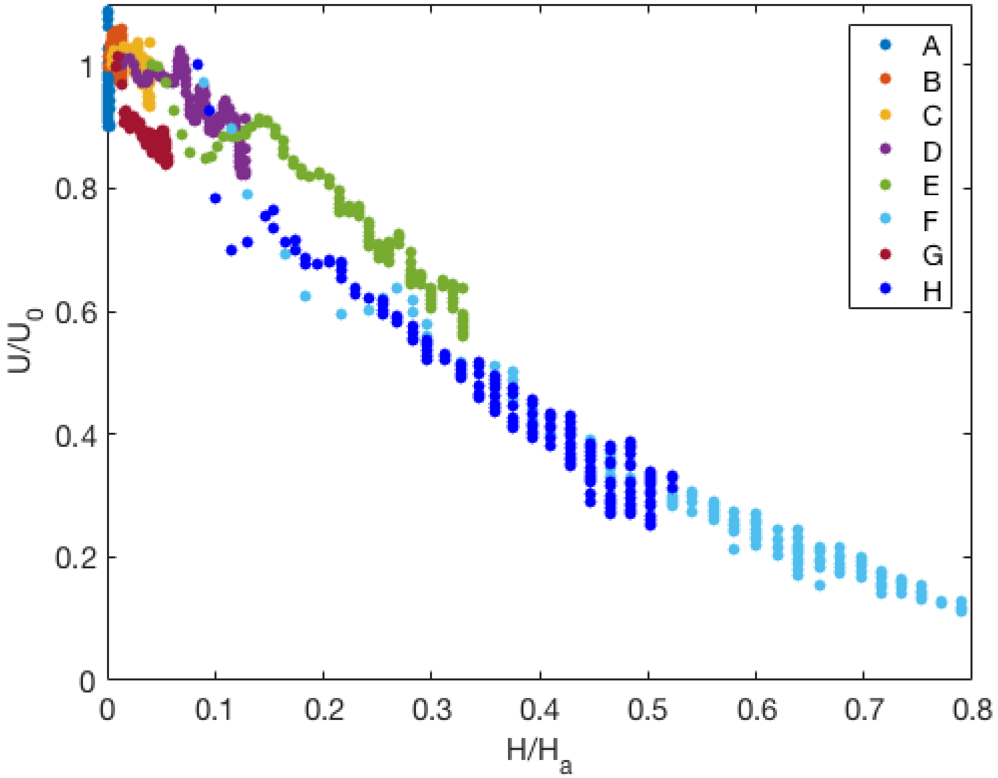

Figure 4.11: Plane-averaged cross-slope transport U, non-dimensionalized by the initial transport U_0, as a function of $E_a \equiv H/H_a$. A running mean filter is applied with an averaging window of $5/f$ to remove the large near-inertial oscillations in U. Different colors correspond to the experiments listed in Table 4.1.

identified when properties are averaged over a time comparable to the inertial period. However, at sub-inertial time scales, the simulations exhibit strong oscillations in all turbulent properties. Earlier studies have shown similar results, e.g. Umlauf et al. (2015), although these features were not discussed. We begin by summarizing the time-averaged characteristics of this stage, and then provide further details on the near-inertial resonant behavior.

For cases where the buoyancy force is of leading order, the pycnocline does not sharpen noticeably during the evolution of the BML – the ratio of pycnocline stratification to background stratification is roughly 1 (Fig. 4.7c). Not only does the pycnocline remain weak, but the background stratification penetrates from the top of the BML downward when E_L approaches 1 (Fig. 4.7c). This re-stratification is related to the viscous slope Obukhov length L_s^+, and is discussed further below. The total cross-slope transport arrives at a negligible, but non-zero value; for example in

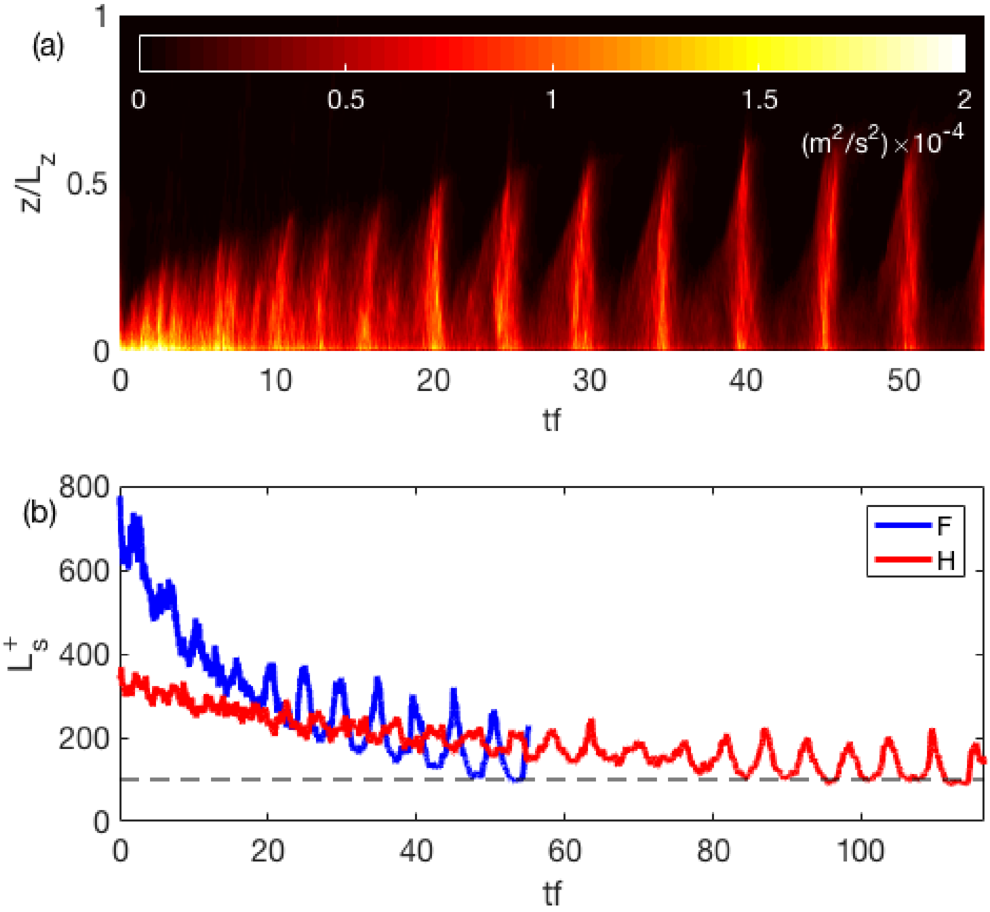

Figure 4.12: The evolution of (a) turbulent kinetic energy (TKE, $\mathrm{m}^2\ \mathrm{s}^{-2}$) for simulation F and (b) viscous slope Obukhov length, L_s^+, (4.11) for simulations F (blue) and H (red). The dashed line represents $L_s^+ = 100$.

Experiment F, this occurs after $tf = 20$ (Fig. 4.9f). The friction velocity continues to decrease linearly with E_a, but remains finite even when L_s^+ approaches 100 (Fig. 4.10a and 4.12b), as predicted in section 4.3. In Experiment F, when L_s^+ approaches 100, the near-bottom velocity V_b is smaller than 0.05 ms^{-1} which is half of the along-slope mean flow magnitude $V_\infty = 0.1\ \mathrm{ms}^{-1}$ (Fig. 4.8b). A reduction in the near-bottom velocity by a factor of 2 results in a reduction of the wall stress by a factor of 4 (4.13), and a reduction in the bottom dissipation rate by a factor of 8, as compared with the predictions using the far-field mean flow V_∞.

From the mean momentum budget (4.6), the predicted arrest height for Experiment F is $H_a \approx 50$ m. This value is larger than the simulated BML thickness in the re-laminarized stage, ~30 m, consistent with $E_a < 1$. The use of (4.14), however, requires an estimate of the drag coefficient C_d. We evaluate $C_d = 2.2 \times 10^{-3}$ at the beginning of Experiment F before stratification is introduced, using

$$C_d = {u_*}^2/{V_b}^2. \tag{4.34}$$

Plugging in the value of C_d and the re-laminarization constant C diagnosed earlier, the predicted H_L is 31.7 m which matches the simulated height well. This demonstrates that the BBL re-laminarization condition is met before the traditional complete Ekman arrested state.

As Experiments F and H reach $E_L \approx 1$, the boundary layer re-laminarizes with negligible turbulent kinetic energy (TKE), e.g. at $tf = 50$ in Experiment F (Fig. 4.12a). The value of L_s^+ that corresponds to this re-laminarization is roughly 100 in both cases, which is the same value reported by Flores and Riley (2011) using the viscous Obukhov length scale Lu_*/ν (Fig. 4.12b). With $C = 100$, the predicted friction velocities in the arrested boundary layer from (4.12), using parameters from Experiments F and H, are $u_* = 1.71 \times 10^{-3}$ m s^{-1} and $u_* = 1.37 \times 10^{-3}$ m s^{-1}, respectively, which agree with the simulated values of u_* in Fig. 4.10a. The arrested wall stress and friction velocity remain finite as predicted from section 4.3.

Another prominent feature of the large E_L regime is the appearance and growth of strong oscillations and resonant behavior. These appear in almost all of the properties discussed above. For instance, both cross-slope transport and TKE oscillate, and the amplitude of these oscillations grows with time (Figs. 4.9f and 4.12a). The friction velocity oscillates at a near-inertial frequency, but the amplitude does not grow with time. These growing oscillations in cross-slope transport give rise to bursts in TKE (Figs. 4.9f and 4.12a). Even though the cross-slope transport averaged over each near-inertial cycle is decaying towards the arrested value, the maximum amplitude of U continues to grow. This indicates an underlying resonant interaction between the stratification and turbulent motions. Analysis of the phase relation between the stratification, TKE and turbulent momentum flux, shows that each time the isopycnals tilt downslope, the stabilizing effect from the stratification vanishes, resulting in a burst of TKE and turbulent momentum flux convergence in the BML. This then advects the isopycnals further downslope. When the near-inertial oscillation advects the isopycnals upslope, turbulence becomes suppressed at the same time that the stratification strengthens, which results in negligible TKE. The intrinsic frequency can be identified as

$$\omega = (f^2 + \alpha^2 N_\infty^2)^{1/2}; \tag{4.35}$$

the inertial frequency is modified by the slope angle and background stratification (Brink and Lentz, 2010a). In the re-laminarized stage, background turbulence becomes weak, such that all of the key properties that influence the BBL, e.g. thermal wind shear, cross-slope transport and wall stress, all oscillate at the same frequency ω (Figs. 7c, 9f and 10a), and resonance is likely to occur. In the ocean, resonant behavior may be disrupted or suppressed by temporal variability in the mean flow arising from surface forcing, tides or internal waves, or by background dissipation associated with wave breaking.

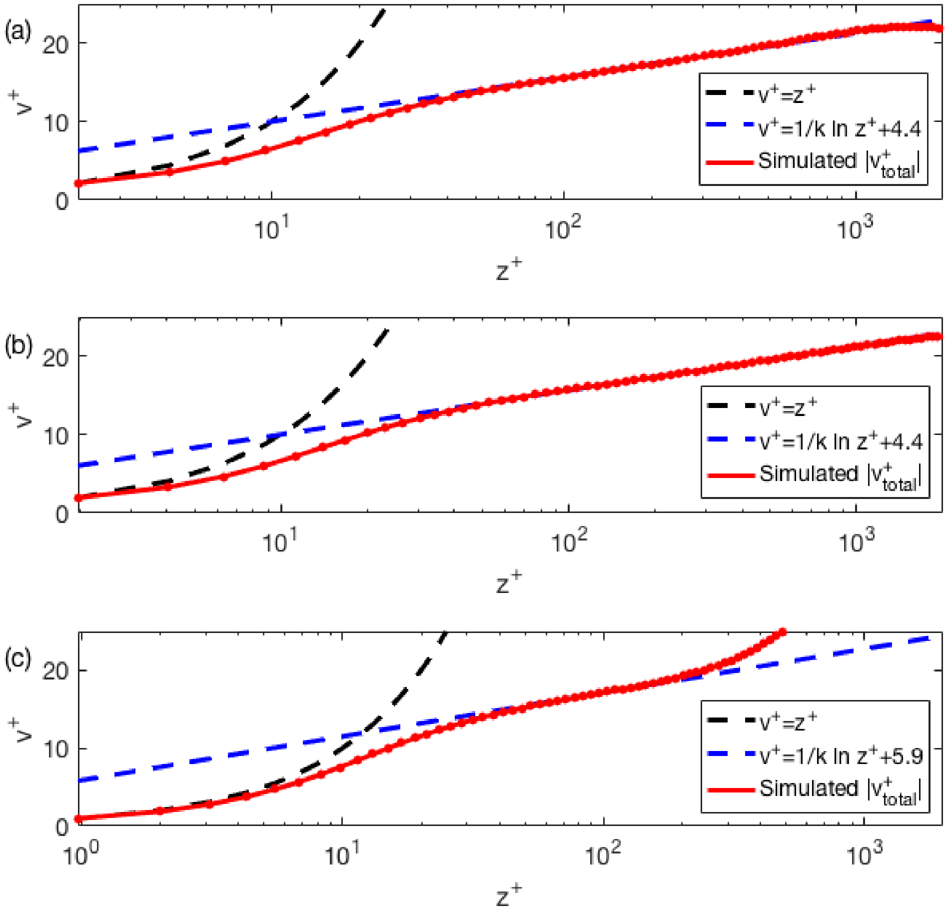

Figure 4.13: The magnitude of the non-dimensional total along-slope velocity $|v^+_{\text{total}}| = (V_\infty - v)/u_*$, as a function of the non-dimensional height above the bottom $z^+ = zu_*/\nu$, in simulations A (a), D (b) and F (c). The dashed black and blue curves denote the linear and logarithmic velocity profiles. The red curve is the simulated $|v^+_{\text{total}}|$ with each dot representing a grid point.

Although u_* decreases as E_a increases, leading to a larger viscous length scale ν/u_*, the near-bottom log-law layer, in fact, becomes shallower (Fig. 4.13). The log-law layer disappears when $z^+ = zu_*/\nu$ reaches 150 in the arrested BBL, whereas it remains intact to at least $z^+ = 2000$ in other stages. These values of z^+ correspond to 4.4 m and 21.6 m in dimensional units with the updated viscous length scale. This places constraints on the first grid point in the near-wall modeling when wall-models are applied.

Ekman arrested regime, $E_a = 1$ and $E_L > 1$

Simulations presented in this study did not achieve steady Ekman arrest because of the long adjustment by molecular diffusion needed to reach this state. This regime transition was not identified in studies that parameterized BBL turbulence. Also, although the averaged quantities over a near-inertial period (e.g. U, u_* and TKE) continue to decay slowly, the oscillations appear to grow stronger, especially for U and TKE (Figs. 4.9 and 4.12). It is unknown if these large oscillations will interrupt the Ekman arrested state. Finally, the fully arrested state has been shown to be susceptible to instabilities, e.g. symmetric instability (Allen and Newberger, 1998), that may also generate turbulent motions and drive the BBL away from the arrested state.

BBL turbulence

As discussed in section 4.3, the Monin-Obukhov length scale L (4.7) describes the evolution of turbulent characteristics in the BBL under both stable and unstable conditions. Previous work has shown that for $H/L < 0$, the boundary layer is unstable; for $0 < H/L < 1$, the boundary layer remains neutral; for $1 < H/L < 10$, the boundary layer is stable; and for $H/L > 10$, the boundary layer turbulence becomes intermittent (Holtslag and Nieuwstadt, 1986).

In these LES, we find that E_L $(= H/H_L)$ is directly related to H/L_s, where the latter non-dimensional parameter is defined using the new slope Obukhov length L_s (Fig. 4.14). The BBL is unstable from the start of the simulation where an upward buoyancy flux is generated by the downslope advection of light fluid (Fig. 4.15a). The buoyancy flux becomes intermittent later in the experiment with positive pulses only evident in the downslope phase of the growing near-inertial oscillations (Fig. 4.15b). The oscillations feature periods with a stablized BBL; the transition occurs near $E_L \sim 0.2$ and $H/L_s \sim 1$. This is different from the classic Monin-Obukhov scaling since H/L_s does not change sign between unstable and stable

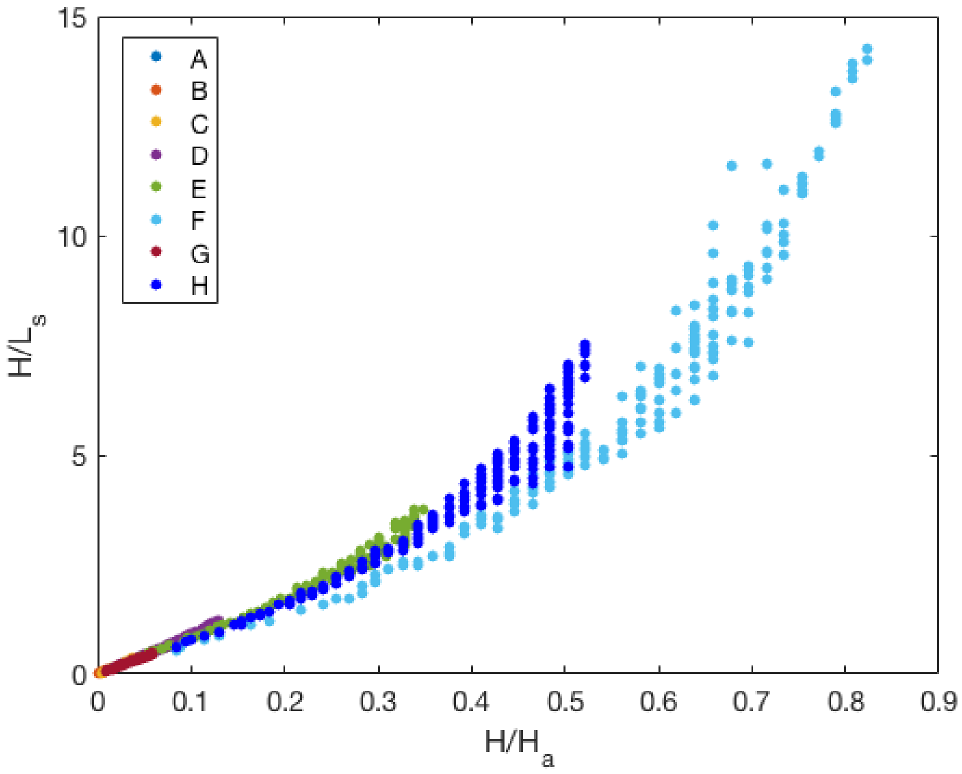

Figure 4.14: The relationship between $E_a \equiv H/H_a$ and H/L_s. Different colors represent different simulations in Table 4.1.

BBLs. The impact of H/L_s on the BBL evolution will be the focus of future studies. We conclude this section by summarizing the various stages in the Ekman arrest process based on non-dimensional parameters (E_a and E_L), the momentum balance, and the near-bottom velocity magnitude V_b (Fig. 4.5).

4.6 Momentum and buoyancy budgets

We now present plane-averaged budgets of momentum and buoyancy to further illustrate the transition in BBL evolution across the weakly buoyant, buoyant and the re-laminarized regimes. The same time average window over a near-inertial period is applied as in section 4.5 unless otherwise noted.

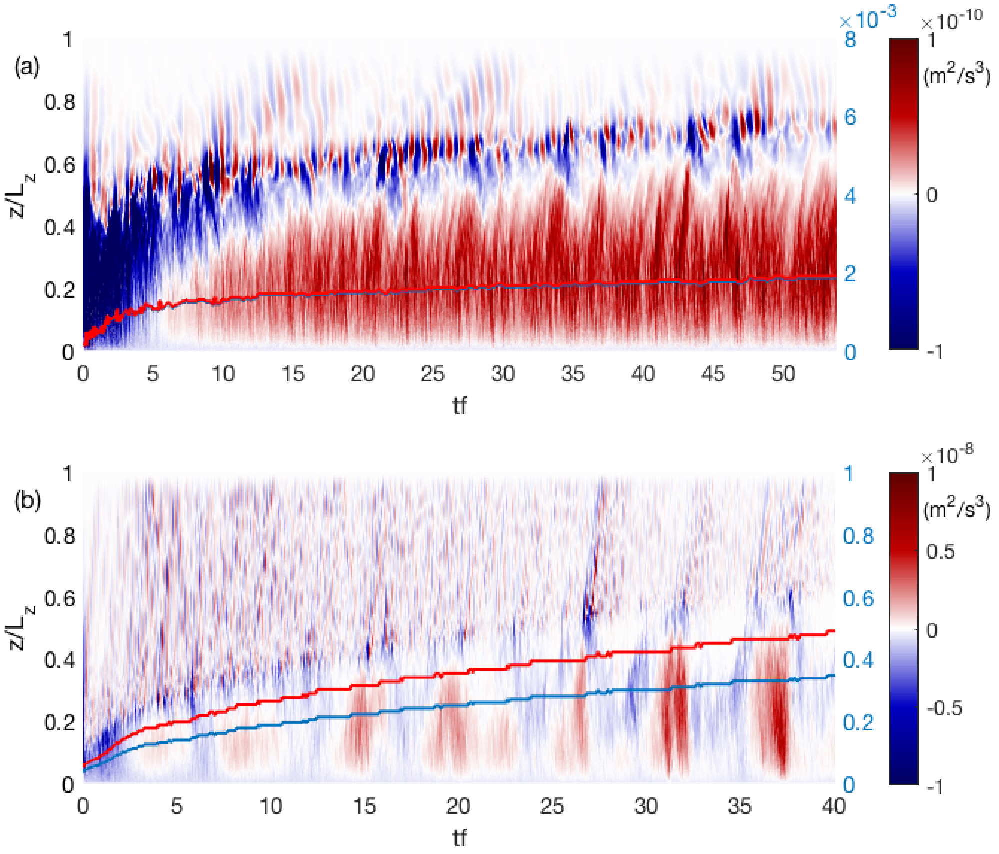

Figure 4.15: The evolution of the vertical buoyancy flux as a function of time in simulations A (a) and E (b). The evolution of the non-dimensional parameter E_a and E_L are given by the blue and red curves, respectively, with the corresponding axis on the right in blue. The BBL is unstable with small E_L in simulation A and transitions from unstable to stable in simulation E around $tf = 5$ when E_L exceeds 0.2.

Momentum budget

The plane-averaged horizontal momentum equations in the boundary layer can be written as

$$\begin{aligned} \frac{\partial \langle u \rangle}{\partial t} - f \langle v \rangle &= -b\alpha + \nu \nabla^2 \langle u \rangle - \frac{\partial \langle u'w' \rangle}{\partial z}, && (4.36) \\ \frac{\partial \langle v \rangle}{\partial t} + f \langle u \rangle &= \nu \nabla^2 \langle v \rangle - \frac{\partial \langle v'w' \rangle}{\partial z}, && (4.37) \end{aligned}$$

where angle brackets denote an average along x and y directions, and $\langle u'w' \rangle$ and $\langle v'w' \rangle$ are the vertical turbulent fluxes of horizontal momentum, or the Reynolds stresses. The tendency terms in the momentum equations are small, indicating that the simulations are in quasi-equilibrium even as the BML grows diffusively, and the viscous terms only become important in the viscous sublayer.

For the cross-slope momentum equation (4.36), three terms may contribute based on the magnitude of E_L: the Coriolis force, the buoyancy force and the Reynolds stress convergence. For small E_L, the buoyancy force is negligible, and the classic flat-bottom Ekman balance dominates with the Coriolis force balancing the Reynolds stress convergence (Fig. 4.16a). As E_L transitions to $O(0.1)$, the Coriolis, buoyancy and Reynolds stress convergence terms are all of leading order (Fig. 4.16b). Since the BML is, by definition, relatively well mixed, the buoyancy force decays roughly linearly with height above bottom (Fig. 4.16b). Compared to the small E_L case, the magnitude and vertical structure of the Reynolds stress convergence term remains largely unchanged, but the Coriolis force has a non-negligible contribution further away from the bottom. This is consistent with the penetration of the thermal wind shear away from the boundary and further into the interior. Throughout the BML, F_C and F_B have the same sign. In this case, the BML remains turbulent, and the cross-slope transport and friction velocity are reduced. The momentum balance changes dramatically as E_L approaches one and the boundary layer reaches a re-laminarized state (Fig. 4.16c). Now, F_C and F_B approximately balance in the BML, outside of the thin viscous layer near $z = 0$. Turbulence and turbulent fluxes are suppressed in the re-laminarized state.

A buoyancy force equivalent to F_B does not appear in the along-slope momentum equation (4.37). Thus, the leading order balance between Coriolis and Reynolds stress convergence is independent of E_L (figure not shown). However, the magnitude of these terms varies significantly both across experiments and during individual experiments. As E_L increases, the suppression of turbulence and the reduction in cross-slope Ekman velocity reduces the magnitude of both terms.

Buoyancy budget

The evolution of the plane-averaged buoyancy is described by

$$\frac{\partial \langle b \rangle}{\partial t} = \langle u \rangle \alpha N_\infty^2 + \kappa \nabla^2 \langle b \rangle - \frac{\partial \langle w'b' \rangle}{\partial z}, \tag{4.38}$$

where $\langle w'b' \rangle$ is the plane-averaged vertical turbulent buoyancy flux. Outside of the viscous sublayer, all terms contribute to the buoyancy budget other than the molecular diffusion term. The cross-slope buoyancy advection occurs mainly in the Ekman layer, which is thinner than the BML (Fig. 4.17a and b). For these downslope favorable conditions, cross-slope advection generates a local tendency to

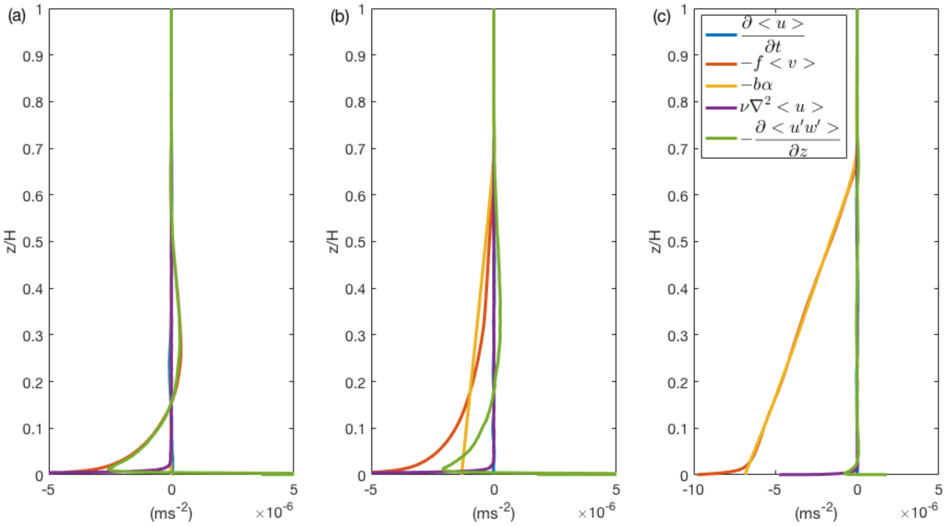

Figure 4.16: The momentum balance in the cross-slope direction given in (4.36) for experiments A (a), D (b) and F (c). The same averaging window is used here as in Fig. 4.9. The blue curve is the momentum tendency, red curve the Coriolis force, orange curve the buoyancy force, purple curve the molecular friction, and green curve the Reynolds stress convergence.

increase buoyancy. The vertical turbulent buoyancy flux diverges in the lower part of the BBL, opposing the cross-slope advection. However, the turbulent buoyancy flux converges in the upper part of the BBL, and without a contribution from the cross-slope advection, produces a positive buoyancy tendency. Finally there is a narrow region of divergence of the turbulent buoyancy flux in the pycnocline.

Within a single experiment, the magnitude of buoyancy advection decreases as E_L increases, although the advection also penetrates deeper into the interior. However, the buoyancy advection term also depends on the background cross-slope buoyancy gradient $M_\infty^2 = -\alpha N_\infty^2$, which is related to the initial Bu. Thus from experiments A to D, the magnitude of the buoyancy advection terms become larger (Fig. 4.17a and b). When re-laminarization occurs in the boundary layer, the cross-slope velocity and total cross-slope buoyancy advection are significantly reduced, although they remain finite (Figs. 4.8a and 4.17c). As E_L approaches 1, the turbulent buoyancy flux convergence becomes negligible in the buoyancy budget due to the suppression of turbulence.

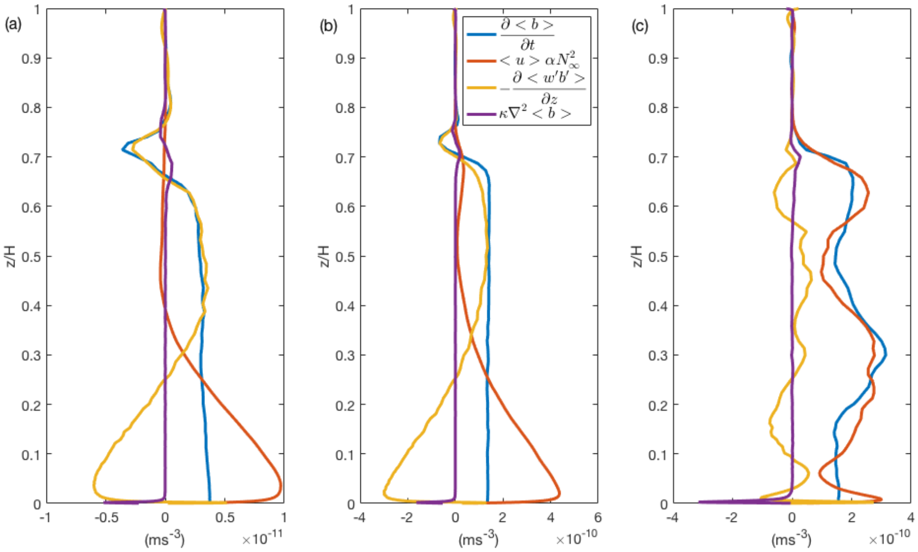

Figure 4.17: The buoyancy budget given in (4.38) for experiments A (a), D (b) and F (c). The same averaging window is used here as in Fig. 4.9. The blue curve is the buoyancy tendency, red curve the cross-slope buoyancy advection, orange curve the turbulent diffusion, and purple curve the molecular diffusion.

4.7 Discussion and conclusions

The bulk structure of a stratified oceanic BBL over a smooth slope is explored using both scaling analyses and LES simulations. The key conclusions include:

1. We provide expressions that predict the height of the bottom mixed layer (BML), H, in a state of Ekman arrest based on the momentum budget, $H_a \approx fV_\infty/(\alpha N_\infty^2)$ (see also Trowbridge and Lentz (1991)), and on the re-laminarization condition, $H_L = \frac{fV_\infty}{\alpha N_\infty^2} - (\frac{Ck\nu f}{\alpha N_\infty^2 C_d (1+Bu^2)})^{1/2}$. We find that H_L is always less than H_a. Two non-dimensional parameters $E_a = H/H_a$ (4.32) and $E_L = H/H_L$ (4.33) can be used to determine the sequential stages of the BBL as it approaches full Ekman arrest.

2. We present a new length scale, the slope Obukhov length L_s, which characterizes the relative importance of turbulence production and cross-slope buoyancy advection (4.10). Its non-dimensional form, the viscous slope Obukhov length L_s^+, can be used to predict the re-laminarization condition for the turbulent BBL ($L_s^+ \approx 100$).

3. We predict the wall stress and friction velocity (4.12) when the BBL becomes

laminar and the turbulence is suppressed. This can be used to estimate the integrated BBL energy dissipation rate at the re-laminarized state.

4. We argue that the complete Ekman arrested state is unlikely to be observed in the real ocean because: i) H_a and H_L are expected to be large based on typical deep ocean parameters, which inevitably leads to a long adjustment timescale; ii) the BBL re-laminarization is always achieved before the steady arrested state, and the subsequent molecular adjustment is prone to external perturbations; iii) in the rare event of full Ekman arrest, the steady arrested BBL is unstable to symmetric instability (see Allen and Newberger (1998)).

5. We show that the non-dimensional parameter E_a describes the evolution of the cross-slope transport and wall stress across different regimes in a suite of simulations that vary several parameters, including the slope angle α, the background vertical stratification N_∞^2, and the mean flow magnitude V_∞. The re-laminarization stage is determined from E_L. The parameters E_a and E_L are closely related to the BBL turbulence through the classic Monin-Obukhov similarity theory (H/L_s), and this framework is used to analyze changes in the momentum and buoyancy budgets across different stages towards the arrested state. The potential vorticity evolution will be discussed in a future study.

As E_L increases, the BML differs from the flat-bottom case in the following ways: (i) the pycnocline at the top of the BML weakens; (ii) the cross-slope velocity penetrates deeper due to the thermal wind shear near the bottom; and (iii) the velocity shear near the wall, and thus the wall stress, weakens, resulting in a decay of the friction velocity, cross-slope transport and the Ekman veering angle near the bottom. When the BBL re-laminarizes, the mean velocity departs from the log-law closer to the bottom.

These results suggest that the interaction between stratification and sloping topography could reduce the contribution of bottom friction to the dissipation of kinetic energy in the ocean. Global quantification of the bottom dissipation rate, using either observations from deep ocean current meters or from numerical models (that typically apply uniform drag coefficients), have not accounted for the modification of near-bottom flows due to the presence of stratification and topographic slopes (Wunsch and Ferrari, 2004; Sen et al., 2008; Arbic et al., 2009; Wright et al., 2013). Additionally, recent work has suggested that the ocean's abyssal circulation may be influenced by the thermal wind shear associated with tilting isopycnals at the seafloor

(Callies and Ferrari, 2018). However, this work typically assumes that the global BBL is largely in the Ekman arrested state. Determining the spatial distribution of E_a and E_L, which can be calculated from observable ocean properties, could shed additional light on the BBL's influence over global dissipation rates and the abyssal circulation.

The BBL over topographic slopes has recently been highlighted as the key region where dense waters can be transformed to lighter density classes to close the overturning circulation (De Lavergne et al., 2016; Ferrari et al., 2016; De Lavergne et al., 2017). Water must also be exchanged between the ocean interior and the boundary layer in order to maintain stratification and sustain this water mass modification. Earlier studies have not accounted for dynamics that will affect mixing rates and BBL-interior exchange. The Ekman arrest process, for instance, could act as a barrier for such exchange via mass flux out of and in to the BBL due to mass convergence/divergence, when strong near-bottom mean flows or (sub)mesoscale eddies are present. Finally, Ekman arrest characteristics may be sensitive to along-isobath variations that are not considered in this study (Brink, 2012). Other factors, such as the level of background turbulence or temporal variability associated with tidal fluctuations in the abyssal ocean, need to be addressed in future studies to estimate the extent to which Ekman arrest is achieved in the ocean.

Chapter 5

BOTTOM BOUNDARY POTENTIAL VORTICITY INJECTION FROM AN OSCILLATING FLOW: A PV PUMP

Ruan, Xiaozhou and Andrew F Thompson (2016). “Bottom boundary potential vorticity injection from an oscillating flow: A PV pump”. In: *Journal of Physical Oceanography* 46.11, pp. 3509–3526. DOI: `10.1175/JPO-D-15-0222.1`.

5.1 Abstract

Oceanic boundary currents over the continental slope exhibit variability with a range of time scales. Numerical studies of steady, along-slope currents over a sloping bathymetry have shown that cross-slope Ekman transport can advect buoyancy surfaces in a bottom boundary layer (BBL) so as to produce vertically-sheared geostrophic flows that bring the total flow to rest: a process known as buoyancy shutdown of Ekman transport or Ekman arrest. This study considers the generation and evolution of near-bottom flows due to a barotropic, oscillating and laterally-sheared flow over a slope. We explore the sensitivity of the boundary circulation to changes in oscillation frequency ω, background flow amplitude, bottom slope and background stratification. When $\omega/f \ll 1$, where f is the Coriolis frequency, oscillations allow the system to escape from the steady buoyancy shutdown scenario. The BBL is responsible for generating a secondary overturning circulation that produces vertical velocities that, combined with the PV anomalies of the imposed barotropic flow, give rise to a time-mean, rectified, vertical eddy PV flux into the ocean interior, a ‘PV pump’. In these idealized simulations, the PV anomalies in the BBL, make a secondary contribution to the time-averaged PV flux. Numerical results show the domain-averaged eddy PV flux increases nonlinearly with ω with a peak near the inertial frequency, followed by a sharp decay for $\omega/f > 1$. We discuss different physical mechanisms that could give rise to the temporal variability of boundary currents.

5.2 Introduction

Boundary processes exert a strong influence over large-scale circulation patterns and energy budgets in both the ocean and the atmosphere (Wunsch, 1970; Schneider et al., 2003). In the ocean, boundary currents over continental shelves and slopes can influence water mass modification (Whitworth et al., 1998; Orsi et al., 2002; Flexas et al., 2015), eddy formation (Molemaker et al., 2015; Gula et al., 2015) and the generation of potential vorticity (PV) anomalies (Williams and Roussenov, 2003). In coastal regions, interactions between ocean boundaries and mean flows influence the distribution of nutrients and other biogeochemical tracers (Gruber et al., 2006; Dulaiova et al., 2009).

The variability associated with these boundary currents are also critical for modifying both buoyancy distributions and turbulent properties in the ocean's bottom boundary layer (BBL). Moum et al. (2004) showed, off the coast of Oregon, that as the orientation (sign) of the along-slope flow changes, the advection of buoyancy surfaces related to either Ekman upwelling or Ekman downwelling can result in quite different turbulent kinetic energy states in the bottom boundary layer. These transitions indicate that there is a coupling between along-slope mean flows and boundary layer circulations over sloping bottom boundaries. Additionally, numerical studies have shown that flow separation over sloping bottom boundaries can be responsible for the generation of mesoscale eddies and their transport into the ocean gyres, (e.g., Molemaker et al., 2015). Thus, the dynamics of boundary layers are likely to impact various aspects of the ocean circulation, such as the along-slope front variability, eddy generation, water mass modification and ventilation near continental slopes and shelves.

Part of the motivation for this study comes from recent observations of high-latitude boundary currents in both the Arctic and the Antarctic. Spall et al. (2008) showed that narrow, bottom-intensified currents in the Beaufort Gyre give rise to PV anomalies over a limited vertical extent above the continental slope. In numerical simulations, these anomalies are shown to be stirred into the interior leading to a banded structure in PV anomalies far from the boundary. During a glider field experiment in the western Weddell Sea, Thompson et al. (2014) observed similar banded PV distributions over the continental slope believed to come from interactions of a predominantly barotropic mean flow, generated by the surface wind stress, and the sloping boundary. These PV gradients are linked to the Antarctic marginal overturning circulation which helps to bring the warm mid-depth water over the shelf break towards ice shelf grounding line. In another numerical experiment, tidal forcing is shown to be critical in reproducing the cross-slope structure and time variability of the Antarctic Slope Front (ASF) and Antarctic Slope Current (ASC) along the South Scotia Ridge (Flexas et al., 2015). This study showed that even without atmospheric forcing, tides can generate the observed structure and variability of the ASF and ASC through tidal rectification over the continental slope. This study suggests that oscillating boundary currents impact the large-scale background density and PV fields.

While there exists a substantial literature on BBL dynamics, understanding of the physical processes that dominate the BBL evolution remains incomplete due to the difficulty of observing and simulating these turbulent processes. This has also led to diverse approaches in representing BBL turbulence. One approach has been direct numerical simulation or large eddy simulations of the boundary layer (Gayen et al., 2010; Gayen and Sarkar, 2011). These simulations are typically limited to relatively small domains that are unable to capture the mechanisms that are the focus of this paper, associated with a jet of width ∼10 km, and will not be discussed further here. Two other approaches have commonly been used to treat the boundary layer turbulence: (i) a "laminar" relationship where the stress is related to a viscosity and a velocity shear, noting that this is an eddy viscosity, which encapsulates the turbulent dynamics (MacCready and Rhines, 1991); and (ii) a turbulent quadratic parameterization (Brink and Lentz, 2010a).

A major result of the first, laminar path has been the mechanistic identification and explanation of Ekman arrest or the buoyancy shutdown of Ekman transport. Thorpe (1987) first developed an analytical model of the adjustment of density surfaces in response to a mean flow over a sloping bottom, which provided steady-state solutions for along-slope and cross-slope velocities. Subsequently, a series of studies showed that the influence of the boundary layer on the interior could be reduced due to Ekman arrest (MacCready and Rhines, 1991; Trowbridge and Lentz, 1991; Chapman, 2002). As a background mean flow interacts with a sloping bottom, a frictional Ekman boundary layer will develop within an inertial time scale. These Ekman velocities advect buoyancy surfaces and produce horizontal buoyancy gradients that balance vertically-sheared geostrophic velocities (thermal wind balance) that oppose the mean flow (Fig. 5.1a). This adjustment mainly happens in a thermal boundary layer defined by the influence of buoyancy diffusion. The result of this Ekman arrest is that both the bottom stress and cross-slope Ekman transport are weakened. Even in the absence of a background flow, isopycnals tend to tilt downslope to meet the no-flux boundary condition and the resulting horizontal buoyancy gradient generates along-slope velocities and a corresponding cross-slope Ekman transport. This is called the buoyancy generation of Ekman transport. The timescale for buoyancy shutdown and buoyancy generation processes are similar; a scaling is provided below.

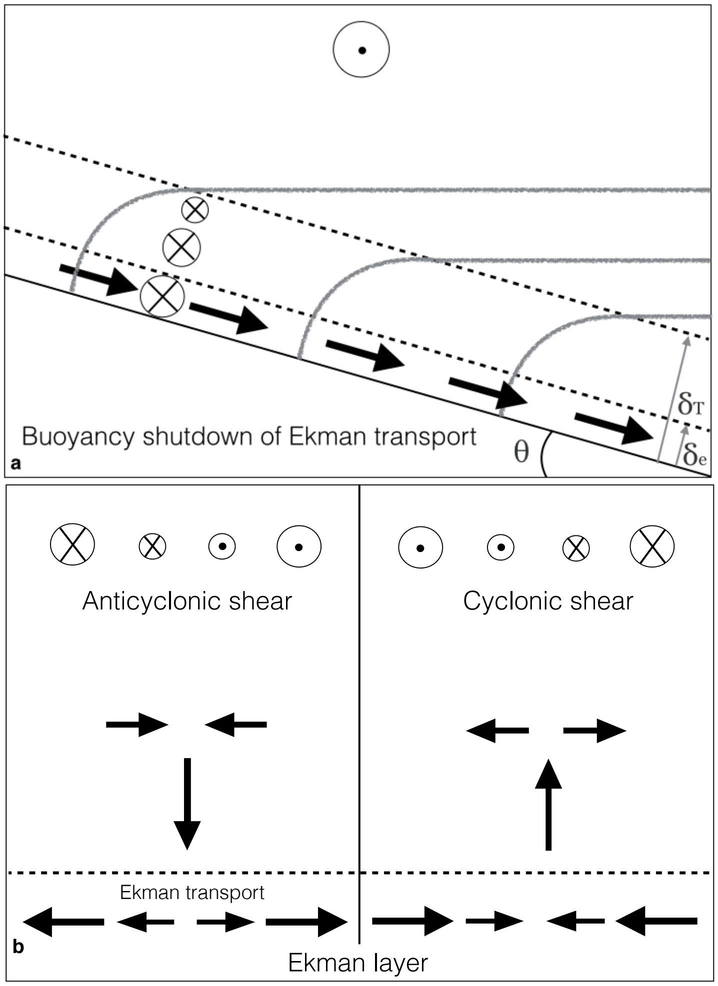

Figure 5.1: Schematic representation of bottom boundary layer processes considering in this study: (a) buoyancy shutdown and (b) frictional spin-down. Arrows as well as dotted- and crossed-circles indicate mean flow direction; gray contours are density surfaces and $f > 0$. In panel (a), a laterally-uniform mean flow generates an Ekman transport in a boundary layer δ_e that tilts isopycnals, which also diffuse in a boundary layer δ_T. The resulting horizontal buoyancy gradient balances a vertically sheared along-slope flow that opposes the interior flow until Ekman transport and buoyancy advection ceases; buoyancy shutdown occurs independent of background flow orientation. In panel (b), a cyclonic (anticyclonic) circulation over a flat bottom induces Ekman pumping (suction) related to Ekman convergence (divergence). This results in a secondary overturning circulation in opposition to the interior pressure gradient, which depletes the kinetic energy of the background flow.

The second, turbulent parameterization path has mostly followed the work by Trowbridge and Lentz (1991). Following this line, Brink and Lentz examined the buoyancy arrest in a turbulent boundary layer in response to a steady mean flow (2010a) and a 1D oscillatory flow (2010b). Differences in the arrest timescale between bottom Ekman upwelling and downwelling cases were identified; these arise from the turbulent mixing parameterization. This study also showed that in the upwelling case, the boundary layer has a more complicated vertical structure, which may include a “transition” layer between the boundary layer and the ocean interior. These cases were referred to as the ’smooth upwelling’ and ’capped upwelling’. While Ekman arrest has also been studied and confirmed using the turbulent parameterization, the mechanism by which the interior flow is damped is not as clearly identified in the momentum equation.

Despite the apparently robust Ekman arrest behavior in numerical simulations, there is limited direct observational evidence of buoyancy shutdown. Furthermore, oceanic observations of the BBL show characteristics of both the laminar and turbulent models. Measurements from moored arrays, in the BBL, collected near the California coast (Trowbridge and Lentz, 1998) and the Oregon coast (Perlin et al., 2005), indicate that Ekman arrest is not fully achieved in the ocean. Yet, these studies also confirmed that the leading order momentum balance, as predicted by analytical models like Trowbridge and Lentz (1991), holds in both the along-slope and cross-slope directions. Perlin et al. (2005) also showed that the vertical stratification may contain multiple layers, including “remnant” turbulent layers outside of the BBL. These outer layers evolve on time scales longer than the bottom mixed layer, similar to a thermal diffusive layer, and are likely to influence the interaction between the BBL and the open ocean.

There are many reasons why Ekman arrest may be absent or weak in the ocean. Most simulations predicting Ekman arrest assume two-dimensional dynamics (as we do here); the impact of along-slope variations on BBL evolution remain relatively unexplored. Our goal in this study is to understand how a time-dependent mean flow influences Ekman arrest and the general characteristics of the BBL. With a view towards elucidating the physical mechanisms that control this evolution, we adopt an idealized process modeling approach following the eddy viscosity representation of MacCready and Rhines (1991). We acknowledge that verification of the physics discussed here in more complex models is an important next step.

Our approach also follows a series of recent studies that have considered bottom boundary processes in the framework of potential vorticity (PV), which is especially useful in eventually assessing the impact of these dynamics on the larger-scale ocean circulation (Rhines, 1986). Benthuysen and Thomas (2012) (BT12 hereafter) developed a one-dimensional analytical model that predicts the time-evolution of buoyancy and along-isobath velocity in response to a steady mean flow. The results show that the change in the vertically-integrated PV depends not only on the mean flow direction, but also on the ratio of the initial mean flow speed to its equilibrated speed. Additionally, the change in the PV is asymmetric: for along-slope currents with the same magnitude but different orientations, removal of PV is more efficient than the injection of PV. A laterally-sheared mean flow was introduced by Benthuysen and Thomas (2013) (BT13 hereafter) and a two-dimensional analytical model was developed. In this case, along-slope flow induces convergence and divergence of the Ekman transport near the boundary, which drives a vertical secondary circulation that depletes the kinetic energy from the interior via the Coriolis force and lateral momentum advection at both leading order and higher order and decelerates the mean flow (See Fig. 5.1b). This process is known as nonlinear frictional spin-down. Both buoyancy shutdown and frictional spin-down may be important if they occur over similar time scales. We adopt the basic setup in BT13 in our study with the addition of a time-dependent far-field velocity forcing.

In this study, we explain how a time-dependent barotropic mean flow reduces the efficiency of the buoyancy shutdown state and produces a rectified injection of PV from the BBL into the ocean interior. The vertical PV flux arises from the generation of a secondary overturning circulation in the depth-cross-slope plane. In section 5.3, we introduce the governing equations that give rise to both buoyancy shutdown and frictional spin-down. Important parameters and expressions for boundary layer thicknesses are provided. In section 5.4, we perform non-dimensionalization and scaling analyses on the governing equations and identify three physical regimes based on the oscillation frequency: (i) the low-frequency or buoyancy shutdown regime, (ii) the near-inertial regime and (iii) the high-frequency regime. The dynamics of each regime is described in section 5.5. In section 5.6, we address controls on PV anomalies and the flux of PV into the ocean interior. We also explore the sensitivity of the PV flux as a function of oscillation frequency, mean flow amplitude, bottom slope angle, and the background stratification. Discussion of results and conclusions are in section 5.7.

5.3 The horizontally sheared and oscillating mean flow model

The equations of motion forced by an oscillating, laterally-sheared barotropic flow over a sloping bottom capture both buoyancy shutdown and an interior frictional spin-down. Our choice of a barotropic background flow is motivated primarily by observations of strong, narrow (width comparable to the deformation radius) shelf-break currents found in many regions (Thompson et al., 2014; Woodgate et al., 2001) . Critically, the boundary currents are observed to vary over a range of frequencies, as evidenced in Fig. 10 of Thorpe (1987), for example. While these currents may have both barotropic and baroclinic structure, they are largely forced by surface winds that generate sea surface height anomalies through surface Ekman transport. While this forcing will not produce variability with a single frequency, we choose to apply an oscillatory mean flow in order to systematically explore parameter space.

It is important to recognize that this form of the externally-forced background barotropic system introduces PV anomalies into the system, due to the relative vorticity associated with the current's lateral shear. These PV anomalies integrate to zero over a full oscillation period, and it is only through the interaction with the vertical velocity generated by the secondary circulation that a non-zero PV flux is produced. The generation of the secondary circulation is dependent on the bottom boundary layer dynamics alone. We explored other background flows that do not generate PV anomalies, such as inertial-gravity, Kelvin and topographic Rossby waves, but the dispersion relations for these motions do not reproduce the observed boundary current properties. Our choice of background flow is motivated by choosing a simple system that provides insight into bottom boundary-interior exchange, but acknowledge that the results presented here need to be explored in more realistic models, especially those that permit feedbacks between the boundary layer-induced circulation and the interior flow.

The Cartesian coordinate system is rotated with an angle θ so that the z axis is normal to the slope (Fig. 5.2). The cross-slope direction y increases off shore, while the along-slope direction x increases with the shallower water to the right. The flow is symmetric in the along-slope direction. The angle of rotation is small ($\theta \leqslant 0.03$) so that the small angle approximation $\cos\theta \approx 1$ and $\sin\theta \approx \theta$ can be applied; this approximation is valid for most oceanic continental slopes. Buoyancy b here represents the density perturbation to the constant background stratification $\rho = \rho_0 + \bar{\rho}(\hat{z}) - (\rho_0/g)b$, where the hat represents the local vertical direction. Viscosity ν and diffusivity κ are assumed to be constant and to have the same

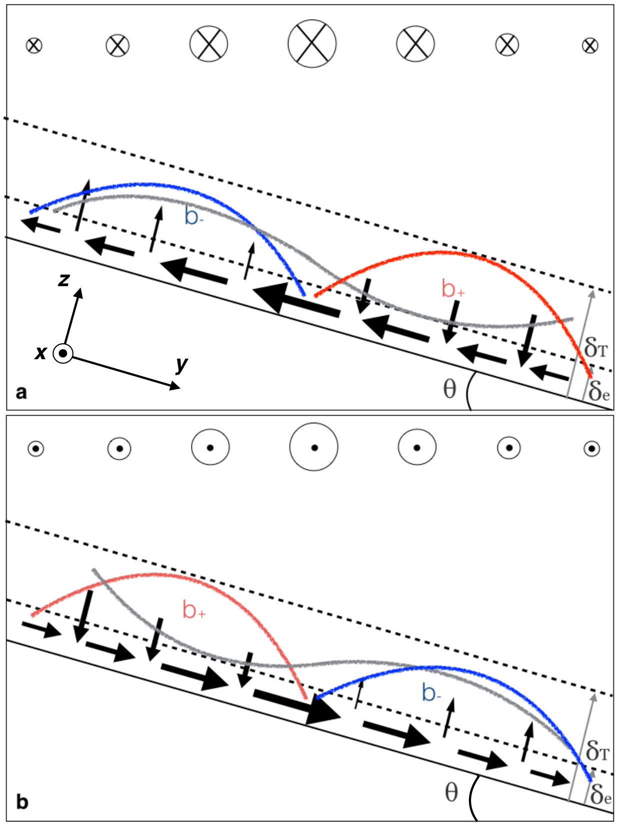

Figure 5.2: Schematic of the coupling between buoyancy shutdown and frictional spin-down over a sloping bottom. A secondary circulation arises from the convergence and divergence of the Ekman transport corresponding to the laterally sheared mean flow ($f > 0$). The dashed lines represent the upper limits of the Ekman layer (δ_e) and the thermal boundary layer (δ_T); gray lines denote buoyancy contours in the thermal boundary layer. Ekman suction advects buoyant fluid toward the bottom boundary and Ekman pumping injects dense fluid upward. Ekman suction is stronger than Ekman pumping due to the higher order nonlinear vertical buoyancy advection (BT13). The asymmetry in vertical buoyancy advection produces steeper isopycnal tilting on the anti-cyclonic flank of the along-slope jet.

magnitude, so the Prandtl number $\sigma = \nu/\kappa = 1$. The basic system is described by the following equations:

$$\frac{\partial u}{\partial t} + v\frac{\partial u}{\partial y} + w\frac{\partial u}{\partial z} - f(v + w\theta) = \nu\left(\frac{\partial^2 u}{\partial y^2} + \frac{\partial^2 u}{\partial z^2}\right), \tag{5.1}$$

$$\frac{\partial v}{\partial t} + v\frac{\partial v}{\partial y} + w\frac{\partial v}{\partial z} + fu = -\frac{1}{\rho_0}\frac{\partial p}{\partial y} - \theta b + \nu\left(\frac{\partial^2 v}{\partial y^2} + \frac{\partial^2 v}{\partial z^2}\right) \tag{5.2}$$

$$\frac{\partial w}{\partial t} + v\frac{\partial w}{\partial y} + w\frac{\partial w}{\partial z} + fu\theta = -\frac{1}{\rho_0}\frac{\partial p}{\partial z} + b + \nu\left(\frac{\partial^2 w}{\partial y^2} + \frac{\partial^2 w}{\partial z^2}\right), \tag{5.3}$$

$$\frac{\partial b}{\partial t} + v(\frac{\partial b}{\partial y} - N^2\theta) + w(\frac{\partial b}{\partial z} + N^2) = \kappa(\frac{\partial^2 b}{\partial y^2} + \frac{\partial^2 b}{\partial z^2}), \tag{5.4}$$

$$\frac{\partial v}{\partial y} + \frac{\partial w}{\partial z} = 0. \tag{5.5}$$

Here $\mathbf{u} = (u, v, w)$ is the velocity vector and $N^2 = -g\rho_0^{-1}\partial\bar{\rho}/\partial\hat{z}$.

The boundary conditions for the semi-infinite vertical domain are no slip, no normal flow and no normal buoyancy flux at the bottom boundary, written as:

$$\begin{cases} u = v = w = 0, & z = 0, \\ \frac{\partial b}{\partial z} + N^2 = 0, & z = 0. \end{cases} \tag{5.6}$$

The far-field boundary conditions are:

$$\begin{cases} u \longrightarrow u_\infty(t, y), & z \longrightarrow \infty, \\ v, w, b \longrightarrow 0, & z \longrightarrow \infty. \end{cases} \tag{5.7}$$

The along-slope mean flow $u(t, y)$ is assumed to oscillate following

$$u_\infty(t, y) = U\cos(\omega t)\left(\frac{1 + \cos(y/L)}{2}\right), \qquad -\pi L < y < \pi L, \tag{5.8}$$

where ω is the oscillation frequency.

There are a number of important timescales in this problem. These include the buoyancy shutdown timescale $\mathcal{T}_{\text{shutdown}} = \sigma^{-1}S^{-2}f^{-1}$, which is valid for $\sigma \sim O(1)$ and $S \ll 1$ (Benthuysen and Thomas, 2012), where $S = (N\tan\theta/f)^2$ is the slope Burger number (MacCready and Rhines, 1991), or using the small angle approximation, $S \approx (N\theta/f)^2$. The stratified spin-down timescale is given by $\mathcal{T}_{\text{spindown}} = E^{-1/2}f^{-1}$, where $E = 2\nu/f{H_p}^2$ is the Ekman number, $H_p = fL/N$ is the Prandtl depth and δ_e is the Ekman depth, defined below. The inertial and diffusive timescales are expressed as $\mathcal{T}_{\text{inertial}} = 2\pi f^{-1}$ and $\mathcal{T}_{\text{diffusive}} = E^{-1}f^{-1}$. The Ekman layer and the diffusive thermal boundary layer have thicknesses that can be expressed as $\delta_e = (2\nu\mathcal{T})^{1/2}$ and $\delta_T = (2\kappa\mathcal{T})^{1/2}$, respectively, where $\mathcal{T}$ is the appropriate characteristic timescale. This timescale need not be the same for δ_e and δ_T. Our choice of timescales in determining the boundary layer thicknesses is dependent on the forcing frequency, ω/f, as discussed in section 5.4.

The other non-dimensional parameters that are relevant for this study include the Rossby number $Ro = U/fL$ and β, which is defined by the ratio of the spin-down timescale to the buoyancy shutdown timescale (BT13),

$$\beta = \frac{\mathcal{T}_{\text{spindown}}}{\mathcal{T}_{\text{shutdown}}} = S^2 E^{-1/2}, \tag{5.9}$$

such that when $\beta \longrightarrow 0$, buoyancy shutdown occurs over a longer time compared to the frictional spin-down. Note that $\beta = 0$ for the case of a flat bottom. The regime in which our simulations sit corresponds to

$$\mathcal{T}_{\text{diffusive}} \gg \mathcal{T}_{\text{shutdown}} \sim \mathcal{T}_{\text{spindown}} \gg f^{-1}. \tag{5.10}$$

The equivalence between $\mathcal{T}_{\text{shutdown}}$ and $\mathcal{T}_{\text{spindown}}$ is a result of our choice of $\beta = \mathcal{O}(1)$, which is consistent with typical ocean parameters (we relax this constraint in our parameter exploration section). To these timescales we add the forcing timescale ω^{-1}.

5.4 Frequency regimes

Our analysis of the boundary layer response to an oscillating mean flow is separated into three regimes based on ω. The regimes are distinguished by the characteristic timescale used to non-dimensionalize (5.1) - (5.8). The length, velocity, buoyancy and pressure scales remain unchanged across the regimes and are given by:

$$y = Ly', \qquad z = H_p z', \tag{5.11}$$

$$u = Uu', \qquad v = Uv', \qquad w = U\Gamma w', \tag{5.12}$$

$$b = N^2 H_p b', \qquad p = \rho_0 N^2 {H_p}^2 p', \tag{5.13}$$

where L and U are the characteristic lateral length scale and the along-slope velocity scale. The Prandtl depth H_p characterizes the height above bottom to which the secondary circulation can penetrate in a stratified fluid. The background mean density is ρ_0 and $\Gamma = H_p/L$ is the aspect ratio. Based on these scales, the no buoyancy flux boundary condition and the along-slope mean flow $u(t, y)$ are non-dimensionalized as (primes dropped):

$$\frac{\partial b}{\partial z} + 1 = 0, \qquad z = 0. \tag{5.14}$$

$$u_\infty(t, y) = \cos(\omega t)\left(\frac{1 + \cos(y)}{2}\right), \qquad -\pi < y < \pi. \tag{5.15}$$

The rest of the boundary conditions retain the same form.

In this study, we find that the time-variable mean flow has the greatest impact in the frictional Ekman layer and variations here propagate into the thermal boundary layer and the interior via the secondary circulation. To illustrate the importance of the forcing frequency on the Ekman velocities, we solve the linear one-dimensional, time-dependent Ekman system with an oscillating far-field boundary condition and a no slip condition at the bottom:

$$\frac{\partial u_e}{\partial t} - f v_e = \nu \frac{\partial^2 u_e}{\partial z^2}; \qquad \frac{\partial v_e}{\partial t} + f u_e = \nu \frac{\partial^2 v_e}{\partial z^2}; \tag{5.16}$$

These solutions are provided primarily to contrast with BT12 in which the Ekman layer reaches a steady state. These solutions are solved using a flat bottom, but in section 5.5 our full simulations are all carried out over a sloping bottom. When the forcing frequency ω is small compared to f, a bottom Ekman layer develops (Fig. 5.3, black curve) with the classic Ekman spiral in the vertical. The boundary layer thickness scales as $\delta_e = \sqrt{2\nu/f}$. Thus in the low-frequency regime, $\omega/f \ll 1$, we assume the Ekman layer is always fully developed, even though it evolves in time. At higher frequencies, and particularly for $\omega/f \gg 1$, rotation is not important and the boundary layer scales as $\sqrt{2\nu/\omega} < \delta_e$ (Fig. 5.3, red curve).

The following subsections show, for completeness, the non-dimensionalization and decomposition of the equations of motion in the different frequency regimes. Readers primarily interested in the main results may prefer to skip to section 5.5.

a. The buoyancy shutdown regime: $\omega/f \ll 1$

If the oscillation frequency is small compared to the inertial frequency ($\omega/f \ll 1$), the characteristic timescale of the system is the frictional spin-down timescale so that $t = \mathcal{T}_{\text{spindown}} t'$. The Ekman layer thickness δ_e is given by $\sqrt{2\nu/f} = E^{1/2} H_p$. The expression for δ_e does not involve $\mathcal{T}_{\text{spindown}}$ because the diffusion of momentum through the Ekman layer is arrested by Earth's rotation before the spin-down timescale. However, the diffusive adjustment of buoyancy is not confined by rotation and the thermal boundary layer thickness is given by $\delta_T = (2\kappa \mathcal{T}_{\text{spindown}})^{1/2} = E^{1/4} H_p > \delta_e$.

The nondimensionalized governing equations, with primes dropped for the dimensionless variables, are as in BT13:

$$E^{1/2}\frac{\partial u}{\partial t} + Ro\left(v\frac{\partial u}{\partial y} + w\frac{\partial u}{\partial z}\right) - (v + w\Gamma\theta) = \frac{E}{2}\left(\Gamma^2\frac{\partial^2 u}{\partial y^2} + \frac{\partial^2 u}{\partial z^2}\right), \tag{5.17}$$

$$E^{1/2}\frac{\partial v}{\partial t} + Ro\left(v\frac{\partial v}{\partial y} + w\frac{\partial v}{\partial z}\right) + u = -Ro^{-1}\frac{\partial p}{\partial y} - Ro^{-1}S^{1/2}b + \frac{E}{2}\left(\Gamma^2\frac{\partial^2 v}{\partial y^2} + \frac{\partial^2 v}{\partial z^2}\right), \tag{5.18}$$

$$Ro\Gamma E^{1/2}\frac{\partial w}{\partial t} + Ro^2\Gamma^2\left(v\frac{\partial w}{\partial y} + w\frac{\partial w}{\partial z}\right) + RoS^{1/2}\Gamma^2 u = -\frac{\partial p}{\partial z} + b + \frac{E}{2}Ro\Gamma^2\left(\Gamma^2\frac{\partial^2 w}{\partial y^2} + \frac{\partial^2 w}{\partial z^2}\right), \tag{5.19}$$

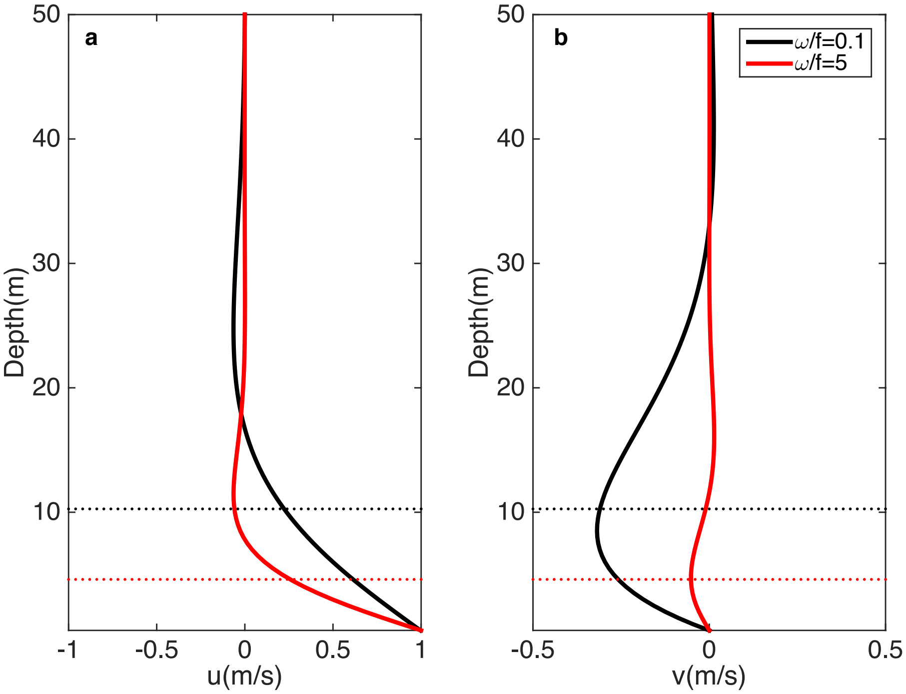

Figure 5.3: Snapshots of (a) along-slope and (b) cross-slope Ekman velocities (m s^{-1}) for a far-field boundary condition that oscillates as $\cos(\omega t)$ over a flat bottom with $\omega/f = 0.1$ (black) and $\omega/f = 5$ (red). f and ν used in this simulation are $1 \times 10^{-4}\ s^{-1}$ and $5.27 \times 10^{-3}\ m^2 s^{-1}$ respectively. The dashed lines denote the boundary layer depth defined as $\delta = \sqrt{2\nu/f}$ (black) and $\delta = \sqrt{2\nu/\omega}$ (red). For $\omega/f \ll 1$, the boundary layer is arrested by the Earth's rotation. For $\omega/f > 1$, the Ekman layer is not well developed and cross-slope velocities are weak.

$$E^{1/2}\frac{\partial b}{\partial t} + Ro(v\frac{\partial b}{\partial y} - vS^{1/2}) + Ro(w\frac{\partial b}{\partial z} + w) = \frac{E}{2}(\Gamma^2\frac{\partial^2 b}{\partial y^2} + \frac{\partial^2 b}{\partial z^2}), \tag{5.20}$$

$$\frac{\partial v}{\partial y} + \frac{\partial w}{\partial z} = 0. \tag{5.21}$$

Following BT13, the non-dimensionalized velocities, buoyancy and pressure can be decomposed into three components representing the interior, thermal boundary layer and Ekman layer, decorated by subscripts i, T and e, respectively,

$$u = u_i + \beta^{1/2}u_T + u_e, \tag{5.22}$$

$$v = E^{1/2}v_i + \beta^{1/2}E^{1/2}v_T + v_e, \tag{5.23}$$

$$w = E^{1/2}w_i + \beta^{1/2}E^{3/4}w_T + E^{1/2}w_e, \tag{5.24}$$

$$b = Rob_i + Ro\beta^{1/2}S^{-1/2}b_T + RoS^{1/2}b_e, \tag{5.25}$$

$$p = Rop_i + RoS^{1/2}p_T + RoS^{1/2}E^{1/2}p_e, \tag{5.26}$$

We also use a perturbation approach to solving (5.17) through (5.21), expanding to $O(E^{-1/4}Ro)$. A key result of this previous study is that there is a coupling between the buoyancy shutdown mechanism and the interior spindown process, which causes the region of vertical Ekman suction (downwelling) to have a larger amplitude than the region of Ekman pumping (upwelling). This result is achieved by considering both leading and higher order terms in the expansion.

b. The near inertial regime: $\omega/f \sim O(1)$

For the low-frequency regime discussed in the previous section, the Ekman layer is in a quasi-steady state and the time tendency term in (5.17) through (5.20) is neglected. However, when ω is comparable to the inertial frequency ($\omega/f \approx 1$), the quasi-steady state Ekman velocities are no longer valid. Furthermore, in this near-inertial regime, the response of velocities in the interior, thermal and frictional boundary layers may exhibit different phase lags, as compared to the low-frequency regime.

Instead of the spin-down timescale that characterizes the low-frequency regime, the system now responds to the shorter timescale associated with the mean flow oscillation. This modifies our previous non-dimensionalization by introducing $t = t'/\omega$, which requires the introduction of a new parameter that represents the ratio of the mean flow oscillation frequency ω and the inertial frequency, $\alpha = \omega/f$. Note that the Prandtl depth remains as the vertical length scale in the non-dimensionalization, as in the low-frequency regime. The Ekman and thermal boundary layer scalings also remain unmodified.

The new non-dimensionalized equations are given by (primes dropped):

$$\alpha\frac{\partial u}{\partial t} + Ro(v\frac{\partial u}{\partial y} + w\frac{\partial u}{\partial z}) - (v + w\Gamma\theta) = \frac{E}{2}(\Gamma^2\frac{\partial^2 u}{\partial y^2} + \frac{\partial^2 u}{\partial z^2}), \tag{5.27}$$

$$\alpha\frac{\partial v}{\partial t} + Ro(v\frac{\partial v}{\partial y} + w\frac{\partial v}{\partial z}) + u = -Ro^{-1}\frac{\partial p}{\partial y} - Ro^{-1}S^{1/2}b + \frac{E}{2}(\Gamma^2\frac{\partial^2 v}{\partial y^2} + \frac{\partial^2 v}{\partial z^2}), \tag{5.28}$$

$$Ro\Gamma^2\alpha\frac{\partial w}{\partial t} + Ro^2\Gamma^2(v\frac{\partial w}{\partial y} + w\frac{\partial w}{\partial z}) + RoS^{1/2}\Gamma^2 u = -\frac{\partial p}{\partial z} + b + \frac{E}{2}Ro\Gamma^2(\Gamma^2\frac{\partial^2 w}{\partial y^2} + \frac{\partial^2 w}{\partial z^2}), \tag{5.29}$$

$$\alpha\frac{\partial b}{\partial t} + Ro(v\frac{\partial b}{\partial y} - vS^{1/2}) + Ro(w\frac{\partial b}{\partial z} + w) = \frac{E}{2}(\Gamma^2\frac{\partial^2 b}{\partial y^2} + \frac{\partial^2 b}{\partial z^2}), \tag{5.30}$$

$$\frac{\partial v}{\partial y} + \frac{\partial w}{\partial z} = 0. \tag{5.31}$$

These equations differ from (5.17)-(5.21) in the tendency term where α replaces $E^{1/2}$. In the near-inertial regime, α is $\mathcal{O}(1)$, which primiarly impacts the Ekman layer as discussed below. In the thermal boundary layer, the leading order balance takes the form

$$\alpha \frac{\partial b_T}{\partial t} \approx \frac{E}{2}\left(\frac{\partial^2 b_T}{\partial z^2}\right). \tag{5.32}$$

We apply a multiple scale solution of the form $b_T(t,\tau)$, where $\tau = \epsilon t$ and $\epsilon = \left(\omega \mathcal{T}_{\text{spindown}}\right)^{-1}$. Removing the secular term at leading order results in a solution for the leading order b_T that adjust diffusively on the slow time scale (as opposed to $1/\omega$) with the same boundary layer thickness as in the low-frequency regime.

Following a similar procedure to BT13, the variable decompositions, with the new parameter α, now become:

$$u = u_i + \alpha^{-1/2} S E^{-1/4} u_T + u_e, \tag{5.33}$$

$$v = \alpha^{-1/2} E^{1/2} v_i + \alpha^{-1/2} S E^{1/4} v_T + v_e, \tag{5.34}$$

$$w = \alpha^{-1/2} E^{1/2} w_i + \alpha^{-1/2} S E^{1/2} w_T + \alpha^{-1/2} E^{1/2} w_e, \tag{5.35}$$

$$b = Rob_i + \alpha^{-1/2} Ro S^{1/2} E^{-1/4} b_T + \alpha^{-1} Ro S^{1/2} b_e, \tag{5.36}$$

$$p = Rop_i + \alpha^{-1/2} Ro S^{1/2} p_T + \alpha^{-3/2} Ro S^{1/2} E^{1/2} p_e, \tag{5.37}$$

With the new scalings, and assuming $\alpha \approx 1$, the horizontal momentum equations in the Ekman layer are:

$$\frac{\partial u_e}{\partial t} - v_e = \frac{1}{2}\frac{\partial^2 u_e}{\partial \eta^2} \tag{5.38}$$

$$\frac{\partial v_e}{\partial t} + u_e = \frac{1}{2}\frac{\partial^2 v_e}{\partial \eta^2} \tag{5.39}$$

where $z = E^{1/2}\eta$ is the scaling for the vertical distance in the Ekman layer. These are the non-dimensional forms of (5.16). A time-dependent initial-boundary-value problem for a viscous incompressible fluid in a rotating co-ordinate was first solved by Greenspan and Howard (1963), while Brink and Lentz (2010b) showed that this system can give rise to enhanced velocities when the forcing frequency is near the inertial frequency, a resonant interaction. For this reason, the Ekman layer velocity structure in the near-inertial region differs from that depicted in Fig. 5.3. This resonant interaction between the adjusting Ekman layer and the background forcing can be seen in the Ekman transport (Fig. 5.4), and this confirms an empirically-determined velocity-stress relation discussed by Brink and Lentz (2010b).

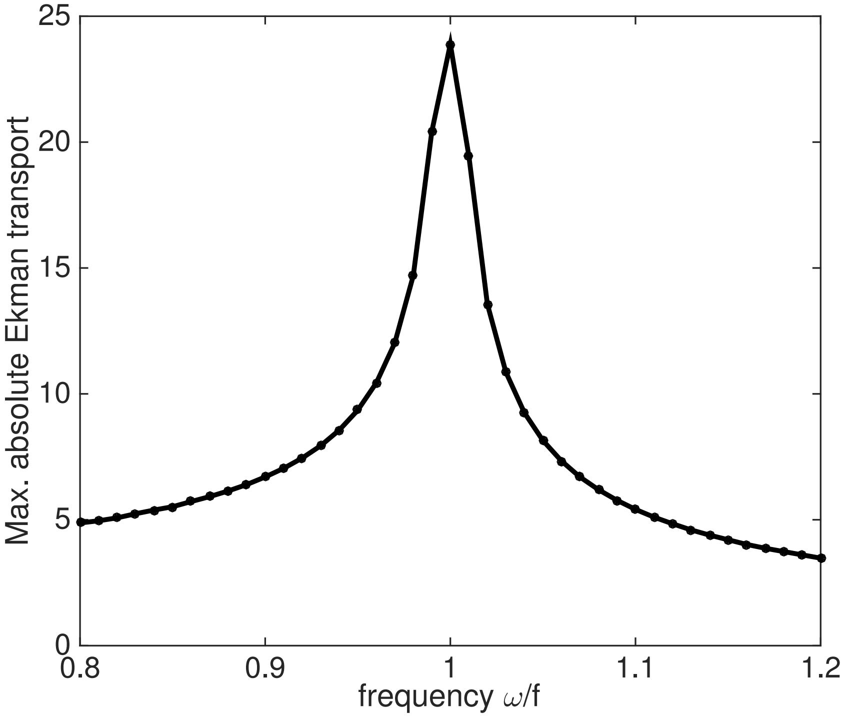

Figure 5.4: Maximum (with respect to time) cross-slope Ekman transport (absolute value and non-dimensionalized by $U\delta_e$) as a function of the far-field oscillation frequency ω for a one-dimensional simulation. The Ekman transport is calculated as the vertical integral of the non-dimensional cross-slope Ekman velocity in equations (5.38) and (5.39) . Black dots denote individual simulations.

The scaling for the thermal boundary layer is not affected by the higher frequency oscillations in the near-inertial regime. The buoyancy generation timescale (similar to the buoyancy shutdown and frictional spin-down timescales) is still used to determine δ_T because diffusion dominates the distribution of buoyancy over long times. Since the buoyancy generation process arises from a competition between Ekman advection of buoyancy surfaces and their diffusive adjustment near the boundary, we can test that our choice of using $\mathcal{T}_{\text{spindown}}$ is valid by using a one-dimensional model, which has similar set-up as in BT12 but with an oscillating mean flow over a sloping bottom. The result is shown in Fig. 5.5. Zero buoyancy anomalies, arising from flat isopycnals are initially apparent. However, after a period comparable to the buoyancy generation (or frictional spin-down) timescale, the isopycnals adjust to a state with downslope tilt, producing the persistent positive buoyancy anomalies for $t > \mathcal{T}_{shutdown}$. The buoyancy surfaces continue to oscillate around a steady state. This solution does not include the vertical advection of buoyancy, which makes a small contribution over long time scales.

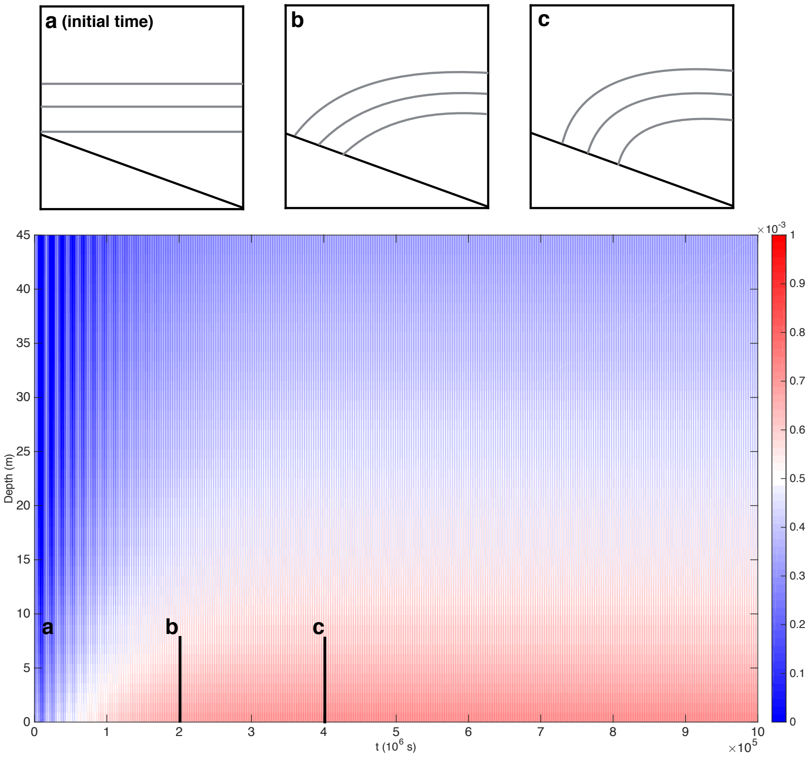

Figure 5.5: Buoyancy anomalies (m s^{-2}) over a sloping bottom ($\theta = 0.01$) in response to an oscillatory mean flow ($\sin(\omega t)$) with frequency $\omega/f = 5$. The shutdown timescale $\mathcal{T}_{\text{shutdown}} = \sigma^{-1}S^{-2}f^{-1}$ for this simulation is 4×10^5 s (denoted by the thick solid line). The long-term behavior is characterized by a diffusive timescale ($\mathcal{T}_{\text{diffusive}} = E^{-1}f^{-1}$) which tends to tilt the isopycnals down-slope (positive anomalies) to meet the no-buoyancy-flux boundary condition. Schematics (a)-(c) depict the buoyancy distribution at three different time a, b and c. Other parameters used in this simulation include $N^2 = 1.6 \times 10^{-5}$ s^{-2} and $\nu = \kappa = 5.27 \times 10^{-3}$ $m^2 s^{-1}$.

c. The high frequency regime

For the high-frequency oscillation regime ($\omega/f \gg 1$), the Ekman layer is no longer arrested by rotation. Instead, the frictional bottom boundary layer thickness can be expressed as $\delta_e = \sqrt{2\nu/\omega}$. The thickness of the frictionally-balanced boundary layer is dependent on the mean-flow oscillation frequency, but the thermal boundary layer thickness retains the same scaling as in the near-inertial regime. For the remainder of the study, we will focus on the low-frequency and near-inertial regimes for two reasons. First, in the ocean, there are few processes that generate persistent oscillations at periods considerably smaller than the inertial period. Second, in this high-frequency regime, rotation effects are small, which leads to weak cross-slope velocities. In the absence of significant cross-slope velocities, convergence and divergence in the bottom boundary layers can not generate strong vertical velocities and the secondary circulation will also be weak. This effect can be seen from the velocity profiles in Fig. 5.3b[1].

5.5 Model solutions

In the following section, we describe numerical simulations of the equations discussed in section 5.4. This section is organized similar to the previous section, with each regime discussed in a separate subsection. The equations are non-dimensionalized and seperated into different systems (i.e. the Ekman layer, thermal boundary layer and interior) based on the variable decomposition given in each subsection in section 5.4 and then solved in each system at leading order and first order ($R_oE^{-1/4}$) separately using a combination of the Crank-Nicolson implicit method and Adam-Bashforth linear multi-step method. Parameters that are uniform across all three regimes are the slope angle $\theta = 0.01$, the jet width $L = 1 \times 10^4$ m, the Rossby number $Ro = 0.1$, the Ekman number $E = 6.42 \times 10^{-4}$, buoyancy frequency (squared) $N^2 = 1.6 \times 10^{-5}$ s^{-2} and the inertial frequency $f = 1 \times 10^{-4}$ s^{-1}. Based on these parameters, the β value is 1.01 from (5.9). In the low-frequency regime the system of equations is similar to those that appear in section 4 of BT13. In the near-inertial regime a time-dependent Ekman layer must be added and the revised scalings alters the expansion as detailed in the previous section.

a. The buoyancy shutdown regime

In the low-frequency regime, Ekman layer dynamics, the secondary circulation and buoyancy diffusion are all active, which give rise to both buoyancy shutdown and frictional spin-down effects. Fig. 5.6 shows a snapshot of the velocity components from an example solution in the low-frequency regime. The snapshot is taken at $t/\mathcal{T}_{\text{spindown}} = 0.15$, however the velocity fields repeat the same cycles across each oscillation period, $2\pi/\omega$.

Although the background mean flow is continuously evolving, the inertial timescale is much shorter than the oscillation timescale, such that the Ekman layer is always close to its steady-state, developed structure. This quasi-steady Ekman transport

---

[1] Once again, the flat-bottom examples discussed in this section are introduced to provide insight into the relationship between the oscillating background flow and the Ekman layer dynamics. In the remainder of this study, we discuss simulations that have a sloping bottom boundary.

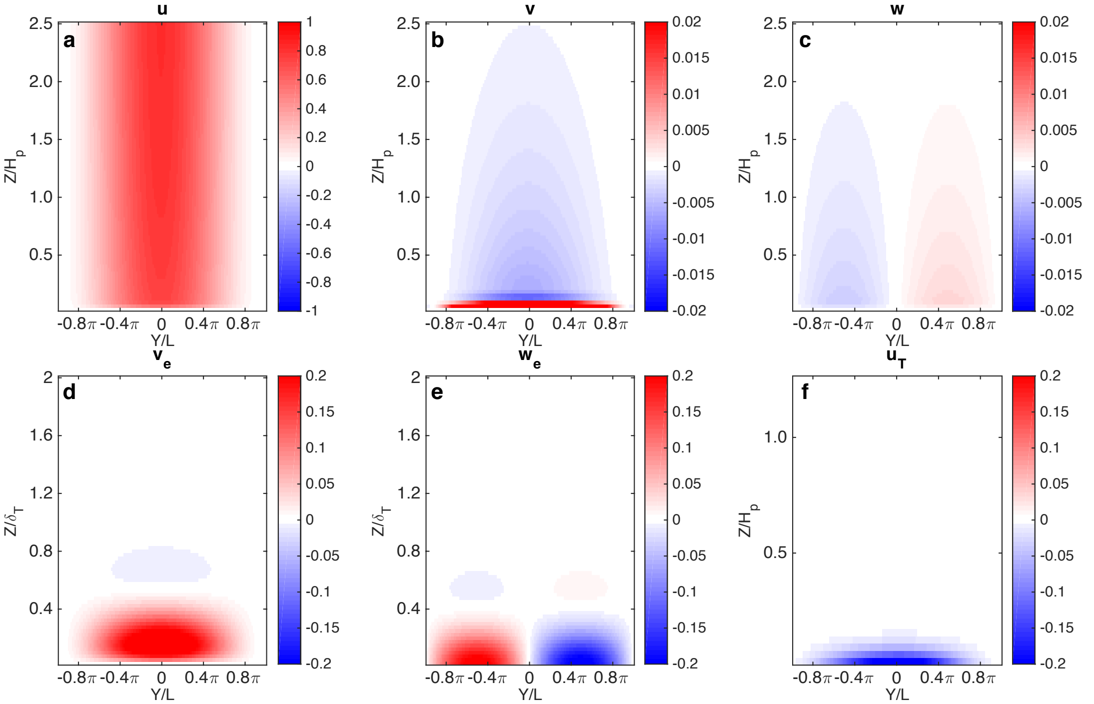

Figure 5.6: Snapshots of non-dimensional velocities at time $t/\mathcal{T}_{\text{spindown}} = 0.15$ in the low-frequency regime ($\mathcal{T}_{\text{spindown}} = E^{-1/2}f^{-1}$), $\omega/f = 0.1$: (a) total along-slope velocity, (b) total cross-slope velocity, (c) total velocity normal to the slope, (d) Ekman cross-slope velocity, (e) Ekman velocity normal to the slope and (f) thermal component of the along-slope velocity. The latter is the opposing velocity from the buoyancy shutdown. Note that the vertical axes and color scales have different normalizations ($\delta_T = E^{1/4}H_p$) and ranges respectively to better demonstrate the velocity structures.

is to the left of the mean flow ($f > 0$), as is shown in Fig. 5.6b. Due to the laterally-sheared mean flow, convergence and divergence in the Ekman layer induce a secondary circulation that has a signature in the interior v and w fields (Fig. 5.6b,c). The component of the total vertical velocity that comes from Ekman layer dynamics w_e has the opposite sign of the interior vertical velocity w_i, which is necessary to satisfy the bottom boundary condition, $w = 0$. Nonlinearity in the system arises from interaction between the buoyancy field and the vertical velocity in the thermal boundary layer. By decomposing the variables as discussed in section 5.4a and expanding (5.20) in powers of $RoE^{-1/4}$ (BT13), the buoyancy equation becomes:

$$\frac{\partial b_T}{\partial t} + RoE^{-1/4} w_i(z = 0) \frac{\partial b_T}{\partial \xi} = \frac{1}{2} \frac{\partial^2 b_T}{\partial \xi^2}. \tag{5.40}$$

where ξ is the vertical axis for the thermal boundary layer. The vertical velocity w_i is evaluated at the bottom since variations in w across the thermal boundary layer are small.

The temporal evolution of the buoyancy field b is shown in Fig. 5.7. The Ekman transport advects buoyancy anomalies (isopycnals) up-slope and down-slope in the bottom-most frictional boundary layer δ_e, and buoyancy anomalies are then diffused deeper into the thermal boundary layer δ_T. At early times, Ekman pumping and suction are stronger during the up-slope transport phase as compared to the down-slope transport phase. This occurs because the fluid becomes more stratified with upslope-buoyancy advection, whereas down-slope buoyancy advection destroys the stratification. This asymmetry weakens over time as buoyancy diffusion takes over. At longer times, an asymmetry in the vertical extent of the buoyancy anomalies develops with positive buoyancy anomalies extending further into the interior. This arises due to the nonlinear vertical buoyancy advection in (5.40).

As buoyancy anomalies accumulate in the interior over time, this results in an asymmetry in the isopycnal tilting with greater tilting on the cyclonic side of the along-slope current, where the negative buoyancy anomalies are located (Fig. 5.1). Because the isopycnals are tilted more steeply around the cyclonic axis, the resulting stronger thermal wind shear leads to stronger Ekman suction than Ekman pumping, as discussed in BT13. These asymmetries may contribute to the preference for anti-cyclonic vortex formation as found both in measurements (Garfield et al., 1999) and numerical simulations (Kurian et al., 2011).

While these simulations have many similarities with BT13, when the mean flow is allowed to oscillate, the system never completely achieves the shutdown state. Ekman velocities are persistently generated and continue to advect buoyancy surfaces throughout the duration of the simulation. This leads to the persistent generation of buoyancy anomalies that are continuously advected into the interior. The relationship between Ekman layer, thermal layer and interior dynamics becomes more complicated in the near-inertial regime as discussed in the next subsection.

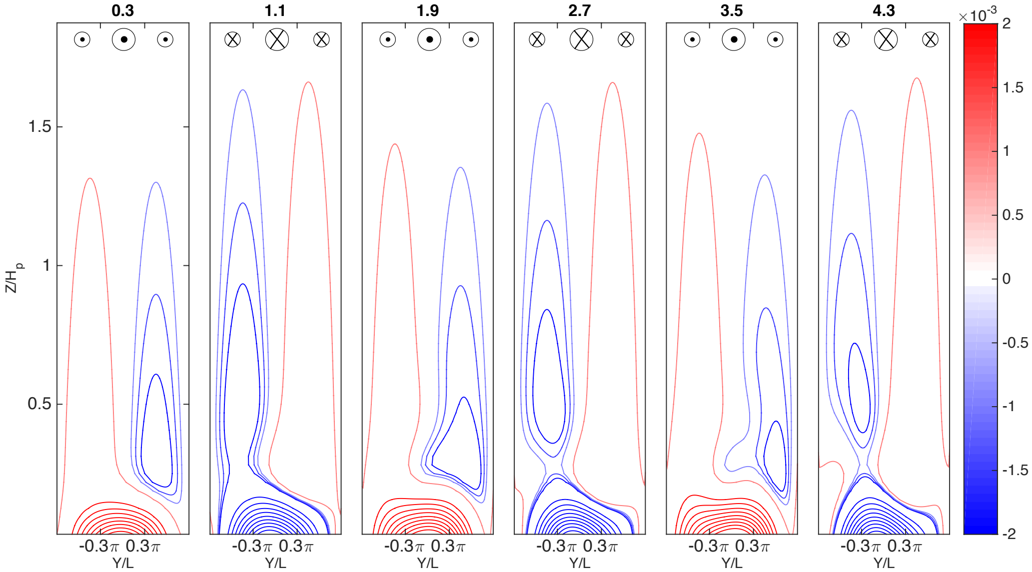

Figure 5.7: Evolution of the buoyancy anomaly in the low-frequency or buoyancy shutdown regime ($\omega/f = 0.1$). Numbers above each panel denote the non-dimensional time $t' = t/\mathcal{T}_{\text{spindown}}$ with a non-dimensional period being $\pi/2$. Snapshots are chosen to show buoyancy distributions twice per cycle of the background flow oscillation. In the Ekman and thermal boundary layers, buoyancy anomalies are generated by up-slope and down-slope advection of the isopycnals and buoyancy diffusion. Higher-order nonlinear vertical buoyancy advection results in slightly stronger Ekman suction compared with Ekman pumping due to stronger isopycnal tilting over the cyclonic flank of the jet.

b. The near-inertial regime

The structure of the velocity and the buoyancy fields are similar in the near-inertial regime to the fields shown in Fig. 5.6. As discussed above, the biggest difference between the near-inertial regime and the low-frequency regime is that in the latter, the Ekman layer is always in a quasi-steady state. In the near-inertial regime a time-dependent Ekman solution is required. Specifically, there may be a phase shift between the mean flow amplitude and the Ekman response, which can modify the coupling between the vertical velocity and the buoyancy or potential vorticity fields. This coupling between the different fields is sensitive to ω as discussed below.

Additionally, for $\omega \sim f$, resonance may occur in the Ekman layer, which strongly enhances the Ekman and vertical velocities. This behavior was discussed by Brink and Lentz (2010b) in the context of a turbulent boundary layer with an oscillating background mean flow with no lateral variations. We have repeated similar experiments, *e.g.* one-dimensional with an oscillatory background mean flow, but with a laminar background, consistent with the rest of this study. We also find a narrow peak in Ekman transport for $\omega = f$ (Fig. 5.4). Although this solution is calculated for a one-dimensional case, the Ekman transport, at each position along the continental slope, will scale with the strength of the mean flow, such that for a laterally-sheared mean flow oscillation, the Ekman convergence and thus the secondary circulation will also have peak for $\omega = f$.

c. The high-frequency regime

Persistent oscillations with frequencies much greater than f are rare in the ocean. Furthermore, for $\omega \gg f$, both the frictional boundary layer, essentially a diffusive layer for momentum, and the thermal boundary layer are controlled by viscosity and diffusivity (assumed constant in this study) respectively. More importantly, the Ekman layer shifts into a regime where its vertical extent is determined by ω, as opposed to f ($\delta_e \sim \sqrt{\frac{\nu}{\omega}}$). The Ekman transport is both suppressed and confined to narrower boundary layers, which results in a smaller velocity component in the cross-slope direction. Therefore the high-frequency regime produces smaller vertical fluxes and smaller injection of fluid into the interior.

5.6 PV dynamics

The Ertel PV is defined as $q = \omega_a \cdot \nabla B$ where $\nabla B = \nabla b + N^2\hat{z}$ is the total buoyancy gradient and $\omega_a = f\hat{z} + \nabla \times \mathbf{u}$ is the absolute vorticity. The non-dimensionalized PV is given by $q' = q/(fN^2)$. For the remainder of this section, we remove the primes, but non-dimensionalized quantities are understood and we discuss the non-dimensional PV to $O(RoE^{-1/4})$. The leading order PV comes from the background stratification and in its non-dimensional form, is equal to 1. The additional contributions to the potential vorticity come from vortex stretching, the relative vorticity and lateral buoyancy gradients, assumed to be in thermal wind balance. Using this approach, the PV is expressed as

$$q \approx 1 + \underbrace{\frac{\partial b}{\partial z}}_{q_b} \underbrace{- Ro\frac{\partial u}{\partial y}}_{q_\zeta} \underbrace{- (Ro\theta/\Gamma)\frac{\partial u}{\partial z}}_{q_{\mathrm{tw}}} . \tag{5.41}$$

Modifications to the PV arising from the vertical buoyancy gradient q_b are mainly due to buoyancy adjustment in the Ekman and the thermal boundary layers. The modification to the PV due to relative vorticity q_ζ is dominated by the horizontal gradient of the mean along-slope velocity. Finally, the vertical gradient of the along-slope velocity (thermal wind), which gives rise to q_{tw}, is generated by the opposing geostrophic velocity in the boundary layer due to tilted isopycnals.

The oscillation frequency $\omega/f = 0.1$ is adopted as an example to analyze the PV dynamics. The low-frequency regime provides a clearer demonstration of the physical processes that are responsible for the rectification of the PV flux. A non-zero PV flux develops both in the boundary layers and in the interior, but the amplitude of the PV flux is significantly stronger within the thermal bounday layer (Fig. 5.8c). In the thermal boundary layer, the PV develops a positive anomaly for a negative along slope flow, as in Fig. 5.8b. The positive PV near the bottom mainly comes from the stretching and thermal wind components, which are shown in Fig. 5.9. In the interior, the PV is dominated by horizontal shear of the mean flow. The vertical velocity arises from the Ekman convergence and is symmetric, to leading order, about $y/L = 0$. At higher order, the amplitude of the downward vertical velocity in Fig. 5.8a is stronger due to vertical buoyancy advection and results in asymmetric isopycnal tilting.

The vertical eddy PV flux is given by $w'q'$, where $'$ represents a deviation from the spatial (cross-slope and depth) mean value. In the thermal boundary layer, the PV flux obtains both positive and negative values, however, in a cross-slope average $\langle w'q'\rangle > 0$, where $\langle\cdot\rangle$ represents an average over $-\pi < y/L < \pi$ (Fig. 5.8d). In the interior, the sign of the horizontal shear is correlated with the sign of the vertical velocity due to the secondary circulation, such that the PV flux is always positive. Thus the oscillatory mean flow generates a persistent rectified PV flux due correlations between the secondary circulation and the PV anomalies in both the boundary layer and the interior. In the interior, the eddy PV flux decays with height above bottom (Fig. 5.8d). In the boundary layer, the asymmetry in the eddy PV flux mainly results from the asymmetry in the isopycnal tilting between cyclonic and anticyclonic flanks of the along-slope flow. This then influences the stretching component of the PV. The spatially-averaged PV flux $\langle w'q'\rangle$ is strongest in the thermal boundary layer and critically is positive for all phases of the oscillation. Converting from non-dimensional variables back to dimensional quantities, we find that the eddy PV flux can penetrate to a depth of at least 500 m based on the current parameters. This may represent a large fraction of the water column in regions close to the continental shelf. The PV flux has a maximum (dimensional) magnitude of order 10^{-15} m s^{-4}, consistent with BT12 and discussed further in section 5.7.

The three components of the Ertel PV anomaly, q_ζ, q_b, q_{tw}, in one phase of the

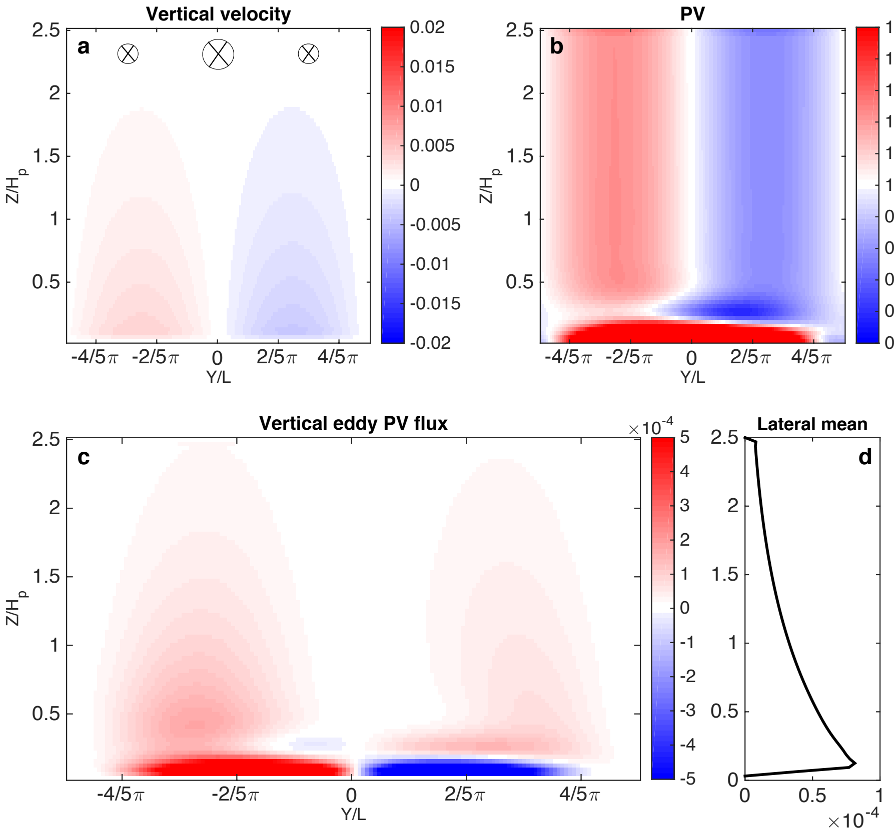

Figure 5.8: Characterization of potential vorticity and vertical potential vorticity flux for an experiment with $\omega/f = 0.1$ at $t/\mathcal{T}_{\text{spindown}} = 2.45$: (a) total vertical velocity, (b) Ertel PV and (c) vertical eddy PV flux. (d) Cross-slope mean eddy PV flux corresponding to panel (c). The lack of cancellation of the cross-slope averaged eddy PV flux in the bottom boundary layer results from the asymmetry in the isopycnal tilting between cyclonic and anticyclonic flanks of the jet, which directly modifies the stretching component of the PV (Fig. 5.9).

mean flow oscillation period, are shown in Fig. 5.9. Again, in the interior, the PV is dominated by q_ζ. In the Ekman and thermal boundary layers, all three components contribute. In the Ekman layer, q_b arises from the advection of bouyancy surfaces by the Ekman velocities, Fig. 5.9b. However, q_b modifies the PV throughout the thermal boundary layer, as the buoyancy surfaces respond to vertical advection caused by Ekman convergence. This gives rise to a dipole structure in the vertical direction. In Fig. 5.9c, q_{tw} is shown for a relatively early time in the experiment. Over longer times, buoyancy diffusion will lead q_{tw} to extend throughout the thermal boundary layer, but it does not have the dipole structure of q_b.

Fig. 5.10 summarizes the vertical PV flux for a range of oscillations frequencies,

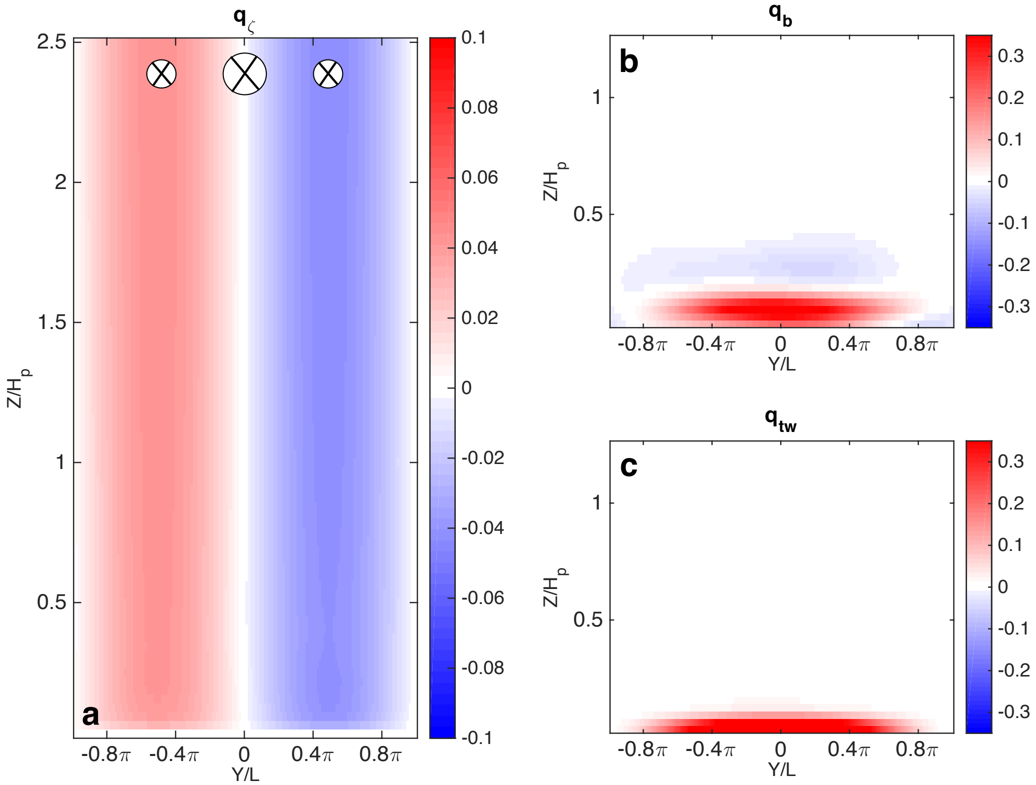

Figure 5.9: Decomposition of the eddy Ertel PV for the snapshot shown in Fig. 5.8b: (a) q_ζ, (b) q_b and (c) q_{tw}, as defined in (5.41). These terms represent (a) the horizontal gradient of the along-slope velocity, which is mostly from the barotropic mean flow shear throughout the water column; (b) the vertical buoyancy gradient; and (c) the vertical gradient of the along-slope velocity, which is due to the generated opposing velocity in the lower boundary. The color scales are not uniform because the vertical velocity and buoyancy gradients near the bottom boundary are larger.

ω/f. Each dot represents a separate numerical simulation, where the eddy PV flux has been calculated as an average over time and area ($y - z$ plane) after the transient adjustment period. In the low-frequency regime, the vertical eddy PV flux increases rapidly and non-linearly with an increase in ω/f (Fig. 5.10, inset). In the low-frequency regime, although the Ekman layer is in a quasi-steady state, the oscillations are effective in avoiding a buoyancy shutdown scenario, which would bring the PV flux to zero (the $\omega/f = 0$ case) after adjustment to the arrested state. This highlights the significance of temporal oscillations in modifying interior distributions of buoyancy and PV. As the frequency becomes larger and $\omega/f \to 1$, the near-inertial regime is approached, where quasi-steady dynamics in the Ekman boundary layer is no longer expected. The phase difference between the Ekman layer and interior response would, by itself, act to reduce the PV flux. However, the resonance that occurs in the Ekman layer (Fig. 5.4) significantly amplifies the secondary circulation, which in turn leads to a peak in the PV flux for $\omega \approx f$. The frequency associated with the peak PV injection falls near the inertial frequency, which suggests that diurnal and semi-diurnal tides, as well as inertial oscillations, may be critical for understanding water mass structure and fluid transport in coastal regions (Flexas et al., 2015). For $\omega > f$, the amplitude of the eddy PV flux decays rapidly, which can be explained by the dynamics in the high frequency regime where there is no longer strong Ekman velocities generated. The change in sign of the PV flux for the high-frequency simulations is related to changes in the phase between oscillations in the velocity and the buoyancy anomalies. This abrupt change in sign needs to be verified in more realistic models.

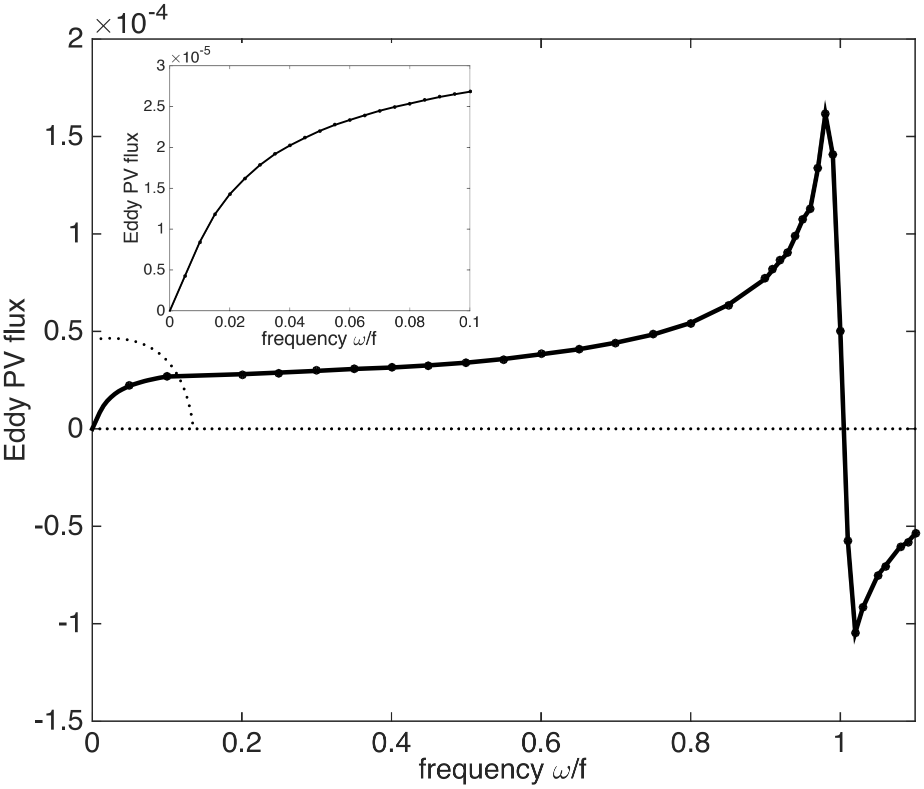

Figure 5.10: Time- and area-averaged non-dimensional vertical eddy PV flux ($\langle \overline{w'q'} \rangle / \Gamma U f N^2 Ro E^{-1/4}$) as a function of oscillation frequency ω. Black dots denote individual simulations. The dotted lines indicate the parameter space shown in the inset plot.

An exploration of the sensitivity of the vertical PV flux to external parameters, including the mean flow amplitude, bottom slope angle and background stratification, is shown in Fig. 5.11. Two values of ω/f are chosen, $\omega/f = 0.1$ for the low-frequency regime and $\omega/f = 0.6$ for the near-inertial regime. The Coriolis frequency is held fixed, although its influence on the simulation can be seen in terms of the slope Burger number $S = (N\theta/f)^2$. The model set-up is the same as is presented in section 5.5.

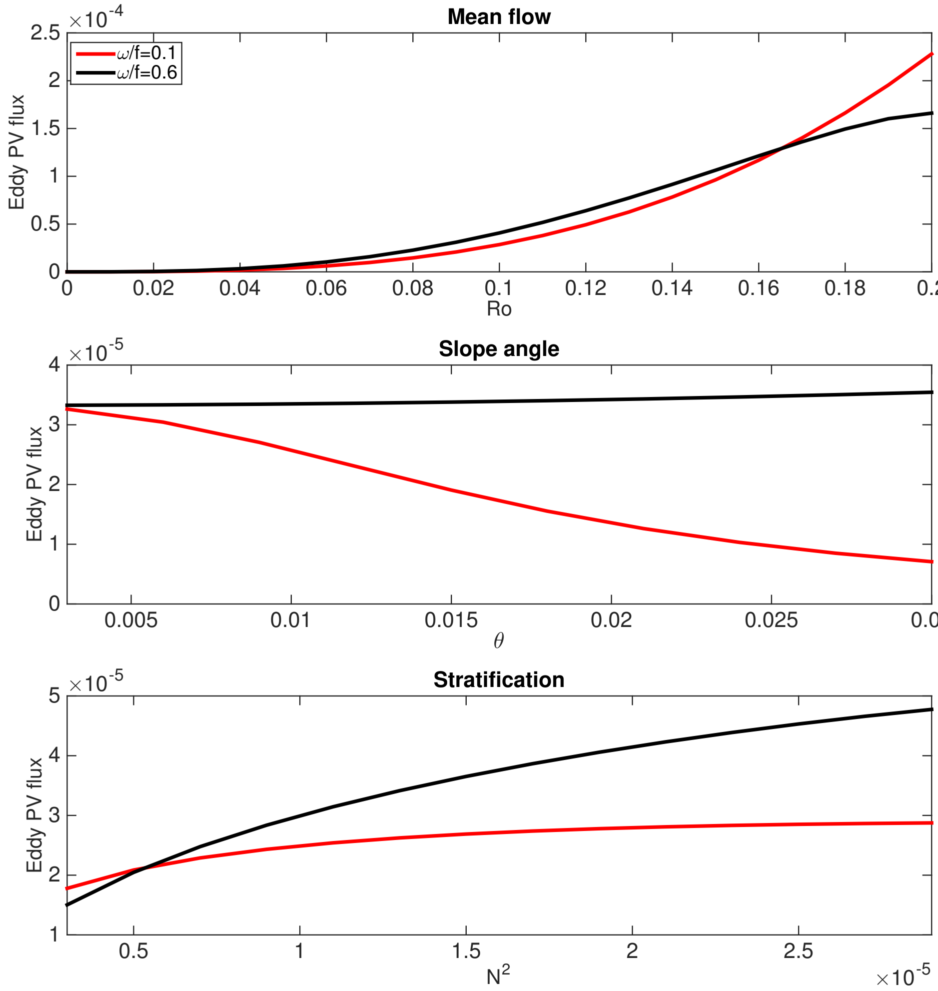

Figure 5.11: Time- and area-averaged vertical eddy PV flux as a function of (a) Rossby number (b) slope angle θ and (c) background stratification N^2 s^{-2}. The latter influences the non-dimensional Ekman number E. In panel (c), the depth over which the PV flux was integrated is equivalent to the Prandtl depth H_p, since H_p varies with changes in N^2. Red and black curves are for simulations with $\omega/f = 0.1$ (low-frequency regime) and $\omega/f = 0.6$ (near-inertial regime) respectively.

Increasing the amplitude of the background mean flow leads to stronger convergence and divergence and thus stronger vertical velocities (Fig. 5.11a), which results in a larger vertical PV flux. Mean flow amplitudes are tested between 0 and 0.2 m s^{-1}, which is equivalent to a change in Ro between 0 and 0.2 since $fL = 1$ m s^{-1}. The eddy PV flux is more sensitive to the amplitude of the topographic slope in the low-frequency regime (Fig. 5.11b). This can be explained by (5.9). As the slope angle θ increases, the slope Burger number S increases leading to a more effective buoyancy shutdown, *i.e.* it occurs over a shorter timescale. Thus during each oscillation cycle, the Ekman layer comes closer to achieving buoyancy shutdown, which reduces the vertical velocity and limits the vertical PV flux. However, in the near-inertial regime, the buoyancy shutdown effect is already weak and therefore the vertical PV flux is almost unaffected by changes in θ. The PV flux increases as the stratification increases (Fig. 5.11c). When the stratification increases, the PV anomaly is enhanced primarily through buoyancy related contributions and thus an enhanced eddy PV flux. Note that the PV fluxes calculated in Fig. 5.11c are integrated in the depth range $0 < z < H_p$, rather than throughout the entire domain. This is done because H_p changes with the stratification and the PV flux extends to different depths when N^2 is varied. Also, considering the variable H_p, the vertical axis in Fig. 5.12 is non-dimensionalized using δ_T. In summary, a larger background stratification will lead to a stronger PV export out of the thermal boundary layer, but this PV flux will not penetrate as far vertically into the interior.

5.7 Conclusions

The coupling between the buoyancy shutdown and the frictional spin-down processes with a laterally-sheared, oscillating mean flow is explored using an asymptotic approach to solving the equations of motion. Three distinct physical regimes are identified. In the low-frequency regime, in which buoyancy shutdown is effective, Ekman transport produces buoyancy anomalies in the frictional boundary layer. The resultant vertical buoyancy gradient interacts with the Ekman-induced vertical velocity in a thermal bounday layer; buoyancy diffusion also occurs in this layer. More importantly, the convergence and divergence in the Ekman transport generates a secondary circulation that penetrates up to 500 m with realistic ocean parameters. The coupling between the vertical circulation and PV anomalies results in a rectified vertical eddy PV flux. In this study, the dominant contribution of PV anomalies is from the laterally-sheared background mean flow rather than from the BBL. Detailed quantification of frictional and diabatic PV fluxes from the BBL awaits

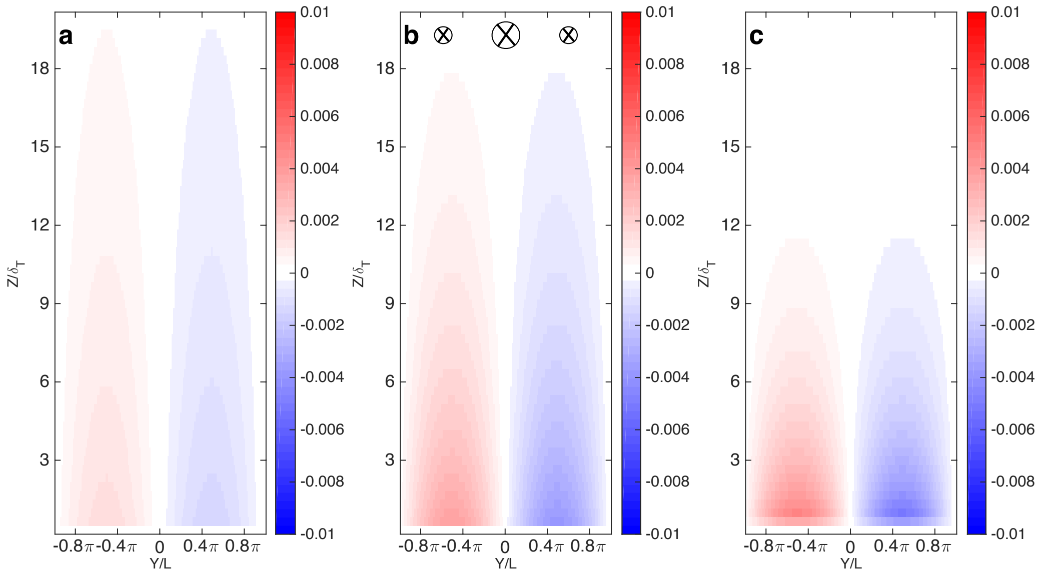

Figure 5.12: Non-dimensional interior vertical velocity distribution ($w_i/\Gamma U$) for an experiment with $\omega/f = 0.1$ at $t/\mathcal{T}_{\text{spindown}} = 4.0$ and different stratifications: (a) $N^2 = 1\times10^{-6}\ \text{s}^{-2}$, (b) $N^2 = 1\times10^{-5}\ \text{s}^{-2}$ and (c) $N^2 = 1\times10^{-4}\ \text{s}^{-2}$. The penetration depth of the secondary circulation decreases with increasing N^2.

further studies using more realistic models. In the absence of oscillations, buoyancy shutdown may run its course and produce a state with no flow in the Ekman layer and no secondary circulation, which eliminates the eddy PV flux as well as the frictional and diabatic PV fluxes due to the slippery (no stress) boundary layer. Even relatively slow temporal oscillations are shown to effectively avoid this state. In the near-inertial regime, the PV injection is influenced by time-dependent Ekman dynamics. As ω approaches f, resonance in the Ekman layer results in amplification of the secondary circulation and a peak in the PV flux. Finally in the high-frequency regime, narrower boundary layers and weaker cross-slope transport greatly reduce the injection of the PV anomaly into the ocean interior.

The vertical eddy PV flux depends on both the oscillation frequency and various external parameters. Specifically, the eddy PV flux is a non-linear function of oscillation frequencies, with strong sensitivity in the low-frequency regime; the

PV flux peaks when $\omega \approx f$. Mean flow amplitude directly influences the Ekman transport, the secondary circulation and thus the PV pumping. The impact of the slope angle is more acute in the buoyancy shutdown regime where the slope angle, contained in the slope Burger number, determines the efficiency of the buoyancy shutdown process over an oscillation period. Increases in background N^2 enhance the injection of PV into the interior, but the stronger interior stratification limits the vertical extent of the eddy PV flux.

The formation of meso-scale and sub-mesoscale eddies along the continental slope arising from interactions between mean flows and sloping topography have recently received attention in a number of studies (Molemaker et al., 2015; Gula et al., 2015). This work has emphasized continental slopes as a lateral boundary that serves as a platform for ageostrophic centrifugal instability to occur. We propose that the PV anomalies that are injected by the processes discussed in this paper could additionally influence the formation of deep eddies near continental shelves and slopes. A key result of this work is that buoyancy and PV anomalies generated in thin boundary layers may be advected much deeper into the interior through secondary circulations. Variability in boundary currents over a range of timescales are likely to minimize the importance of complete buoyancy shutdown. Future work needs to more directly address the interaction between interior and BBL flows than could be explored in the simple model considered here.

The generation of PV anomlies due to surface wind stresses, for example down-front winds (Thomas, 2005), has greatly improved our understanding of mixed layer variability and the upper ocean PV budget. Our understanding of variability of bottom circulations is considerably more limited; this idealized study offers support for the bottom boundary layer playing an important role in larger-scale circulation dynamics. This bottom PV pump mechanism should be considered in the context of slope current variability, water mass formation and continental shelf-slope exchange. These dynamics may be particularly important in high latitude regions where relatively warm but deep waters must cross large topographic (PV) barriers, e.g. Circumpolar Deep Water at the Antarctic margins (Thoma et al., 2008; Thompson et al., 2014). The size of the PV fluxes that occur through the oscillating mean flow are small compared to PV fluxes generated at the ocean surface, (*e.g.* Thomas, 2005), or over the shallow continental shelf (Gula et al., 2015). Nevertheless, the mechanism described here is capable of generating a persistent PV flux in the presence of a variable along-slope current, for instance due to a tidally-oscillating boundary current. As mentioned by BT12, the net modification depends on both a temporal and spatial average of the PV fluxes. Surface processes are likely to be intermittent in both space and time, whereas boundary currents may extend over a broad geographic extent along continental slopes and mid-ocean ridges. While this model is too simple to provide a global assessment of its contribution to deep ocean PV fields, it focuses the attention of future work on boundary processes, consistent with recent assessments of the importance of sloping bottoms on the abyssal overturning circulation (Mashayek et al., 2015).

5.8 Appendix: Analytical solutions for the buoyancy shutdown process on a sloping bottom with laterally uniform and slowly oscillating mean flow.

The basic equations with constant diffusivity κ and viscosity ν following BT 2012 are listed below. The co-ordinate system is rotated similarly as is described early in the main context.

$$\frac{\partial u}{\partial t} - fv = F^x = \frac{\partial}{\partial z}(\nu\frac{\partial u}{\partial z}) \tag{5.42}$$

$$\frac{\partial v}{\partial t} + f(u-U) + \theta b = F^y = \frac{\partial}{\partial z}(\nu\frac{\partial v}{\partial z}) \tag{5.43}$$

$$\frac{\partial b}{\partial t} - N^2\theta v = D = \frac{\partial}{\partial z}(\kappa\frac{\partial b}{\partial z}) \tag{5.44}$$

With the initial conditions:

$$u = U(0), \qquad t = 0 \tag{5.45}$$

$$v = b = 0, \qquad t = 0 \tag{5.46}$$

where the along-slope mean flow U will be addressed below. The no-slip, insulating boundary and far-field boundary conditions are:

$$u = v = 0, \qquad z = 0 \tag{5.47}$$

$$\frac{\partial b}{\partial z} + N^2 = 0, \qquad z = 0 \tag{5.48}$$

$$u \rightarrow U, \qquad z \rightarrow \infty \tag{5.49}$$

$$v, b \rightarrow 0, \qquad z \rightarrow \infty \tag{5.50}$$

Based on the model decomposition in Thomas and Rhines, 2002, variables are decomposed into contributions from the Ekman layer, the thermal boundary layer, and the interior: $u = u_i + u_T + u_e$, $v = v_i + v_T + v_e$ and $b = b_i + b_T + b_e$ where subscripts e, T and i represent the Ekman layer, the thermal boundary layer and the interior respectively. Time is nondimensionalized by the buoyancy shutdown timescale. Other basic variables are nondimensionlized as below:

$$u = |U_{Thorpe}|u', \qquad v = |U_{Thorpe}|u', \qquad b = N^2\delta_T b', \tag{5.51}$$

where U_{Thorpe} is a steady state solution for the along-slope velocity given by Thorpe, 1987. We neglect the nondimensionalized equations, the power expansion of the variables and the separation of variables into different systems here (refer to BT12 for details) and only discuss the leading order solutions in the thermal boundary system with a modified far-field boundary condition. Instead of a constant mean flow boundary condition that was used in BT12, an oscillating flow is given over the sloping boundary, with ω being the oscillating frequency (dimensional):

$$U = U_0 \cdot \cos(\omega t) \tag{5.52}$$

The above boundary condition is nondimensionalized as following (primes dropped):

$$U = \frac{U_0}{|U_{Thorpe}|} \cdot \cos(\omega t) \tag{5.53}$$

The equation below shows the single reduced diffusion equation with variable u_T being the thermal boundary components of the along-slope velocity where ξ is the nondimensionalized vertical axis for the thermal boundary system ($\xi' = z/\delta_T$). All of the following equations and results are in non-dimensional form with primes dropped:

$$\frac{\partial u_T}{\partial t} = \frac{1}{2}\frac{\partial^2 u_T}{\partial \xi^2} \tag{5.54}$$

The initial condition:

$$u_T(t = 0) = 0 \tag{5.55}$$

The boundary conditions:

$$\frac{\partial u_T}{\partial \xi}(\xi = 0) - u_T(\xi = 0) = 1 + \frac{U}{|U_{Thorpe}|} \tag{5.56}$$

$$u_T \to 0, \qquad \xi \to \infty \tag{5.57}$$

The equation is solved by using the Laplace transform, $\widetilde{U_T}(s, \xi) = \int_0^\infty u_T(t, \xi)e^{-st}dt$. The transformed form of equation (5.54) is:

$$s\widetilde{U_T}(\xi, s) - U_T(s, 0) = \frac{1}{2}\frac{d^2\widetilde{U_T}(\xi, s)}{d\xi^2} \tag{5.58}$$

with the use of initial and boundary conditions, a solution is reached as below:

$$\widetilde{U_T}(\xi, s) = C \cdot e^{-\sqrt{2s}\xi} \; (C \; as \; a \; constant) \tag{5.59}$$

Equation (5.59) is plugged back into equation (5.56) and the far-field boundary condition (5.53) is used:

$$\frac{\partial \widetilde{U}(0)}{\partial \xi} - \widetilde{U}(0) = \frac{1}{s} + \frac{U_0}{|U_{Thorpe}|} \int_0^{\infty} e^{-st} \cos{(\omega t)} dt \tag{5.60}$$

Since $\int e^{-st} \cos{(\omega t)} dt = \frac{e^{-st}[\omega \sin{(\omega t)} - s \cos{(\omega t)}]}{s^2+\omega^2}$, $C = -\frac{1}{1+\sqrt{2s}}(\frac{1}{s} + \frac{U_0}{|U_{Thorpe}|}\frac{s}{s^2+\omega^2})$
The final form of $\widetilde{U_T}(\xi, s)$ is:

$$\widetilde{U_T}(\xi, s) = -\frac{e^{-\sqrt{2s}\xi}}{1+\sqrt{2s}}(\frac{1}{s} + \frac{U_0}{|U_{Thorpe}|}\frac{s}{s^2+\omega^2}) \tag{5.61}$$

The final results for the time-dependent thermal boundary layer along-slope velocity are derived using the inverse Laplace transform (Abramowitz and Stegun, 1972). The solutions for the thermal boundary along-slope velocity are composed of one right on the bottom boundary ($\xi = 0$) and one away from the boundary ($\xi > 0$):

$$\begin{aligned} u_T(\xi > 0, t) = {} & [\frac{e^{\frac{t}{2}}}{\sqrt{2\pi}} \int_0^t (\frac{\xi}{\tau} - 1) \frac{e^{-\frac{\tau}{2} - \frac{\xi^2}{2\tau}}}{\sqrt{\tau}} d\tau - \frac{\xi}{\sqrt{2\pi}} \int_0^t \tau^{-\frac{3}{2}} e^{-\frac{\xi^2}{2\tau}} d\tau] \\ & + \frac{U_0}{|U_{Thorpe}|}[\int_0^t \frac{2\omega \sin{[\omega(t-\tau)]} - \cos{[\omega(t-\tau)]} + e^{\frac{t-\tau}{2}}}{4\omega^2+1} \frac{\xi}{\sqrt{2\pi}} \tau^{-\frac{3}{2}} e^{-\frac{\xi^2}{2\tau}} d\tau] \\ & - \frac{U_0}{|U_{Thorpe}|}[\int_0^t \frac{4\omega^2 \cos{[\omega(t-\tau)]} + 2\omega \sin{[\omega(t-\tau)]} + e^{\frac{t-\tau}{2}}}{4\omega^2+1} \frac{1}{\sqrt{2\pi\tau}} e^{-\frac{\xi^2}{2\tau}} d\tau] \end{aligned} \tag{5.62}$$

and

$$\begin{aligned} u_T(\xi = 0, t) = {} & (-1 + e^{\frac{t}{2}} - \sqrt{\frac{2t}{\pi}} - \frac{e^{\frac{t}{2}}}{\sqrt{2\pi}} \int_0^t \tau^{\frac{1}{2}} e^{-\frac{\tau}{2}} d\tau) \\ & + \frac{U_0}{|U_{Thorpe}|}[\frac{2\omega \sin{(\omega t)} - \cos{(\omega t)} + e^{\frac{t}{2}}}{4\omega^2+1}] \\ & - \frac{U_0}{|U_{Thorpe}|}[\frac{1}{\sqrt{2}} \int_0^t \frac{1}{\sqrt{\pi\tau}} \frac{4\omega^2 \cos{[\omega(t-\tau)]} + 2\omega \sin{[\omega(t-\tau)]} + e^{\frac{t-\tau}{2}}}{4\omega^2+1} d\tau] \end{aligned} \tag{5.63}$$

Chapter 6

CONCLUSIONS

This thesis explores the connection between the oceanic bottom boundary layers (BBL) and the abyssal overturning circulation in terms of water mass transformation (WMT) and kinetic energy budget, with a focus on submesoscale dynamics near the BBL. It demonstrates the potential importance of these small-scale physics, which are currently unresolved in general circulation models (GCM), in sustaining a global scale abyssal circulation.

We first proposed an additional pathway to close the overturning circulation and transform Lower Circumpolar Deep Water (LCDW) over sloping topography near the BBL along the path of the Antarctic Circumpolar Current (ACC). Based on the observed evidence of enhanced horizontal buoyancy gradient, large bottom mixed layer thickness and signals of modified water masses, we show that BBL mixing facilitated by submesoscale symmetric instability may contribute significantly to the modification of LCDW. More importantly, depending on the property of the water masses that LCDW mixes with, LCDW may become lighter, instead of all getting incorporated into dense Antarctic Bottom Water (AABW) near the Antarctic margin. Interactions between narrow frontal currents and sloping topography in the BBL occur elsewhere along the path of the ACC, which leads us to propose that such interactions may contribute significantly to the modification of deep and bottom waters in the Southern Ocean, and thus to the closure of the abyssal overturning circulation.

We then shifted our focus to the other end of the abyssal overturning circulation, namely the consumption of AABW away from their formation sites. In particular, we ask the question: what maintains the stratification near the mid-ocean ridge system to allow for effective water mass transformation and the lightening of AABW. To this end, we performed three sets of numerical simulations to examine the flow patterns and restratification mechanisms associated with the wave-breaking induced mixing in the mid-ocean ridge system: a two-dimensional mid-ocean ridge, a three-dimensional mid-ocean ridge without a canyon and a three-dimensional mid-ocean ridge with a canyon. We show that restratification with a mean up-slope buoyancy advection over a two-dimensional ridge is too weak to maintain local stratification.

In the three-dimensional simulations, two different restratification mechanisms have been found. Over the flanks of the mid-ocean ridge, submesoscale baroclinic eddies develop in response to the isopycnal tilting and they subsequently re-stratify the near-bottom fluid by releasing the available potential energy via buoyancy flux; Inside the ridge-flank canyons, however, a stronger stratification is maintained due to a large up-ridge mean flow that reaches more than 1 cm/s. As a consequence of the restratification in the three-dimensional simulations, turbulent buoyancy flux is sustained and thus a persistent convergence near the bottom of the ridge, resulting in a net lightening of the dense bottom water. WMT rates reach a quasi-equilibrium compared with the two-dimensional run. The net consumption of the densest bottom water over the 100 km wide mid-ocean ridge system is around 0.05 Sv, mounting to around 2 Sv in the entire Brazil Basin covering forty degrees in latitude. This is similar to estimates made about the transformation rate of AABW in observations. We reached the conclusion that in order to simulate the bottom water transformation in the GCMs and to close the abyssal meridional overturning circulation, submesoscale baroclinic eddies in the abyss need to be better represented either with enhanced model resolution or with suitable parameterizations, similar to those in the surface boundary layers.

Starting in chapter 4, we moved from mixing-driven BBL to mean flow-driven BBL. The bulk structure of a stratified oceanic BBL over a smooth slope, under the influence of a downwelling-favorable mean flow, is explored using both scaling analyses and large-eddy simulations. We provided two expressions that predict the height of the bottom mixed layer in a state of Ekman arrest, based on the momentum budget and also on the turbulent characteristics. Using these mixed layer depth expressions, we can form a non-dimensional number, the Ekman arrest number, which describes the evolution of the friction velocity and cross-slope Ekman transport in the BBL. Global quantification of the bottom dissipation rate, using either observations from deep ocean current meters or from numerical models (that typically apply uniform drag coefficients), has not accounted for the modification of near-bottom flows due to the presence of stratification and topographic slopes. This chapter thus provides a new theoretical framework to parameterize the bottom friction and the advection of stratification across the sloping topography. In the last chapter, with the BBL turbulence parameterized using constant eddy coefficients, we added the horizontal shear and temporal oscillation into the external mean flow. We explored the coupling between the buoyancy shutdown (Ekman arrest) and the frictional spindown processes using an asymptotic approach to solving the equations of motion and identified three distinct physical regimes as the oscillation frequency varies. We argue that similar exploration with a more realistic turbulent representation is needed to examine the response of the BBL to variations in the external mean flow and the BBL-interior mass exchange.

The focus of this thesis is on the impacts of the BBL and submesoscale dynamics on the abyssal overturning circulation. Each chapter, as they currently stand, focuses on distinct processes, including boundary layer turbulence, submesoscale dynamics and mesoscale frontal currents interacting with the BBL. The associated spatial scales vary between several centimeters and a thousand kilometers. While many questions remain, it becomes increasingly clear that the BBL and submesoscale dynamics have played outsized roles in sustaining the abyssal overturning circulation and its associated WMT.

On the other hand, it seems challenging to combine relevant dynamics of various spatial scales in the future, considering the specific techniques required in approaching the targeted aspects of this BBL-overturning connection. The ultimate goal of studying these small-scale physics is to be able to reproduce a more complete abyssal overturning circulation in the GCM and thus reduce uncertainties in making future climate predictions. Until enough computing power becomes available to resolve all the dynamical scales of interest, the only way forward relies on solid understanding and parameterizations of BBL dynamics. High-resolution *in-situ* observations have become more important in setting the ground-truth reference for future explorations. Passive tracer experiments will undoubtedly shed light on the statistical pathways of the abyssal overturning circulation. The combination of micro-scale profiler measurements on turbulent mixing and high-resolution hydrographic surveys near topographic hotspots with fast mean flows and enhanced eddy kinetic energy will reveal key dynamics involved in the boundary layer upwelling and BBL-interior mass exchange.

The large-scale ocean circulation community has started asking the question: is the abyssal circulation pulled by local geostrophic flows due to density adjustment near the BBL or is it pushed by dense water formation and spreading. This ”pull or push” question is really asking what controls the abyssal circulation. If the former, would the abyssal circulation depend more sensitively on local dynamics or atmospheric events? If the latter, would the abyssal circulation experience seasonality or even longer periods in the glacial/interglacial cycles with different atmospheric conditions? What would be the implications for BBL-interior exchange and more importantly heat and carbon storage in the abyssal ocean? The answers to these questions will depend on the exploration of the BBL and abyssal overturning circulation and will ultimately lead to a better understanding of Earth's climate over long timescales.

BIBLIOGRAPHY

Abramowitz, M. and I. A. Stegun (1972). *Handbook of mathematical functions*. Vol. 1. Dover New York.

Allen, J. S. and P. A. Newberger (1998). "On symmetric instabilities in oceanic bottom boundary layers". In: *Journal of Physical Oceanography* 28.6, pp. 1131–1151.

Arbic, B. K. et al. (2009). "Estimates of bottom flows and bottom boundary layer dissipation of the oceanic general circulation from global high-resolution models". In: *Journal of Geophysical Research: Oceans* 114.C02024.

Armi, L. (1978). "Some evidence for boundary mixing in the deep ocean". In: *Journal of Geophysical Research: Oceans* 83.C4, pp. 1971–1979.

Benthuysen, J. A. and L. N. Thomas (2012). "Friction and diapycnal mixing at a slope: Boundary control of potential vorticity". In: *Journal of Physical Oceanography* 42.9, pp. 1509–1523.

– (2013). "Nonlinear stratified spindown over a slope". In: *Journal of Fluid Mechanics* 726, pp. 371–403.

Bewley, T. R. (2012). *Numerical Renaissance: simulation, optimization, & control*. Renaissance Press.

Brink, K. H. (2012). "Buoyancy arrest and shelf–ocean exchange". In: *Journal of Physical Oceanography* 42.4, pp. 644–658.

Brink, K. H. and S. J. Lentz (2010a). "Buoyancy arrest and bottom Ekman transport. Part I: Steady flow". In: *Journal of Physical Oceanography* 40.4, pp. 621–635.

– (2010b). "Buoyancy arrest and bottom Ekman transport. Part II: Oscillating flow". In: *Journal of Physical Oceanography* 40.4, pp. 636–655.

Burns, K. J. et al. (2016). "Dedalus: Flexible framework for spectrally solving differential equations". In: *Astrophysics Source Code Library*.

Callies, J. (2018). "Restratification of abyssal mixing layers by submesoscale baroclinic eddies". In: *Journal of Physical Oceanography* 48.9, pp. 1995–2010.

Callies, J. and R. Ferrari (2018). "Dynamics of an abyssal circulation driven by bottom-intensified mixing on slopes". In: *Journal of Physical Oceanography* 48.6, pp. 1257–1282.

Chapman, D. C. (2002). "Deceleration of a Finite-Width, Stratified Current over a Sloping Bottom: Frictional Spindown or Buoyancy Shutdown?*". In: *Journal of Physical Oceanography* 32.1, pp. 336–352.

Church, J. A. et al. (2011). "Revisiting the Earth's sea-level and energy budgets from 1961 to 2008". In: *Geophysical Research Letters* 38.L18601.

Clark, P. U. et al. (2002). “The role of the thermohaline circulation in abrupt climate change”. In: *Nature* 415.6874, p. 863.

Clément, L., A. M. Thurnherr, and L. C. St. Laurent (2017). “Turbulent mixing in a deep fracture zone on the Mid-Atlantic Ridge”. In: *Journal of Physical Oceanography* 47.8, pp. 1873–1896.

Coleman, G. N., J. H. Ferziger, and P. R. Spalart (1990). “A numerical study of the turbulent Ekman layer”. In: *Journal of Fluid Mechanics* 213, pp. 313–348.

De Lavergne, C. et al. (2016). “On the consumption of Antarctic Bottom Water in the abyssal ocean”. In: *Journal of Physical Oceanography* 46.2, pp. 635–661.

De Lavergne, C. et al. (2017). “Abyssal ocean overturning shaped by seafloor distribution”. In: *Nature* 551.7679, p. 181.

Deardorff, J. W., G. E. Willis, and D. K. Lilly (1969). “Laboratory investigation of non-steady penetrative convection”. In: *Journal of Fluid Mechanics* 35.1, pp. 7–31.

Dell, R. W. (2013). “Boundary layer dynamics and deep ocean mixing in Mid-Atlantic Ridge canyons”. PhD thesis. Massachusetts Institute of Technology and Woods Hole Oceanographic Institution.

Deusebio, E. et al. (2014). “A numerical study of the unstratified and stratified Ekman layer”. In: *Journal of Fluid Mechanics* 755, pp. 672–704.

Dulaiova, H. et al. (2009). “Shelf-derived iron inputs drive biological productivity in the southern Drake Passage”. In: *Global Biogeochemical Cycles* 23.4.

Ferrari, R. (2014). “Oceanography: What goes down must come up”. In: *Nature* 513.7517, p. 179.

Ferrari, R. and C. Wunsch (2009). “Ocean circulation kinetic energy: Reservoirs, sources, and sinks”. In: *Annual Review of Fluid Mechanics* 41.

Ferrari, R. et al. (2014). “Antarctic sea ice control on ocean circulation in present and glacial climates”. In: *Proceedings of the National Academy of Sciences*, p. 201323922.

Ferrari, R. et al. (2016). “Turning ocean mixing upside down”. In: *Journal of Physical Oceanography* 46.7, pp. 2239–2261.

Flexas, M. M. et al. (2015). “Role of tides on the formation of the Antarctic Slope Front at the Weddell-Scotia Confluence”. In: *Journal of Geophysical Research: Oceans* 120.5, pp. 3658–3680.

Flores, O. and J. J. Riley (2011). “Analysis of turbulence collapse in the stably stratified surface layer using direct numerical simulation”. In: *Boundary-Layer Meteorology* 139.2, pp. 241–259.

Garfield, N. et al. (1999). “Lagrangian exploration of the California Undercurrent, 1992-95”. In: *Journal of Physical Oceanography* 29.4, pp. 560–583.

Garrett, C. (1991). “Marginal mixing theories”. In: *Atmosphere-Ocean* 29.2, pp. 313–339.

Garrett, C., P. MacCready, and P. Rhines (1993). “Boundary mixing and arrested Ekman layers: Rotating stratified flow near a sloping boundary”. In: *Annual Review of Fluid Mechanics* 25.1, pp. 291–323.

Gayen, B. and S. Sarkar (2011). “Negative turbulent production during flow reversal in a stratified oscillating boundary layer on a sloping bottom”. In: *Physics of Fluids (1994-present)* 23.10, p. 101703.

Gayen, B., S. Sarkar, and J. R. Taylor (2010). “Large eddy simulation of a stratified boundary layer under an oscillatory current”. In: *Journal of Fluid Mechanics* 643, pp. 233–266.

Gill, A. E. (1973). “Circulation and bottom water production in the Weddell Sea”. In: *Deep Sea Research and Oceanographic Abstracts*. Vol. 20. 2. Elsevier, pp. 111–140.

Greenspan, H. P. and L. N. Howard (1963). “On a time-dependent motion of a rotating fluid”. In: *Journal of Fluid Mechanics* 17.03, pp. 385–404.

Gruber, N. et al. (2006). “Eddy-resolving simulation of plankton ecosystem dynamics in the California Current System”. In: *Deep Sea Research Part I: Oceanographic Research Papers* 53.9, pp. 1483–1516.

Gula, J., M. J. Molemaker, and J. C. McWilliams (2015). “Gulf Stream dynamics along the southeastern US seaboard”. In: *Journal of Physical Oceanography* 45.3, pp. 690–715.

– (2016). “Topographic generation of submesoscale centrifugal instability and energy dissipation”. In: *Nature communications* 7, p. 12811.

Hill, C. et al. (2007). “Investigating solution convergence in a global ocean model using a 2048-processor cluster of distributed shared memory machines”. In: *Scientific Programming* 15.2, pp. 107–115.

Hogg, N. and W. B. Owens (1999). “Direct measurement of the deep circulation within the Brazil Basin”. In: *Deep Sea Research Part II: Topical Studies in Oceanography* 46.1-2, pp. 335–353.

Hogg, N. et al. (1982). “On the transport and modification of Antarctic Bottom Water in the Vema Channel”. In: *Journal of Marine Research* 40.23, pp. 1–263.

Holmes, R. M., J. D. Zika, and M. H. England (2019). “Diathermal Heat Transport in a global ocean model”. In: *Journal of Physical Oceanography* 49.1, pp. 141–161.

Holtslag, A. A. M. and F. T. M. Nieuwstadt (1986). “Scaling the atmospheric boundary layer”. In: *Boundary-Layer Meteorology* 36.1-2, pp. 201–209.

Kurian, J. et al. (2011). “Eddy properties in the California current system”. In: *Journal of Geophysical Research: Oceans* 116.C8.

Ledwell, J. R. et al. (2000). “Evidence for enhanced mixing over rough topography in the abyssal ocean”. In: *Nature* 403.6766, p. 179.

Levitus, S. et al. (2012). “World ocean heat content and thermosteric sea level change (0–2000 m), 1955–2010”. In: *Geophysical Research Letters* 39.10.

Losch, M. et al. (2010). “On the formulation of sea-ice models. Part 1: Effects of different solver implementations and parameterizations”. In: *Ocean Modelling* 33.1-2, pp. 129–144.

Lozovatsky, I. D., H. J. S. Fernando, and S. M. Shapovalov (2008). “Deep-ocean mixing on the basin scale: Inference from North Atlantic transects”. In: *Deep Sea Research Part I: Oceanographic Research Papers* 55.9, pp. 1075–1089.

Lumpkin, R. and K. Speer (2007). “Global ocean meridional overturning”. In: *Journal of Physical Oceanography* 37.10, pp. 2550–2562.

MacCready, P. and P. B. Rhines (1991). “Buoyant inhibition of Ekman transport on a slope and its effect on stratified spin-up”. In: *Journal of Fluid Mechanics* 223, pp. 631–661.

MacKinnon, J. A. et al. (2017). “Climate process team on internal wave–driven ocean mixing”. In: *Bulletin of the American Meteorological Society* 98.11, pp. 2429–2454.

Manucharyan, G. E. and C. P. Caulfield (2015). “Entrainment and mixed layer dynamics of a surface-stress-driven stratified fluid”. In: *Journal of Fluid Mechanics* 765, pp. 653–667.

Marshall, J., D. Jamous, and J. Nilsson (1999). “Reconciling thermodynamic and dynamic methods of computation of water-mass transformation rates”. In: *Deep Sea Research Part I: Oceanographic Research Papers* 46.4, pp. 545–572.

Marshall, J. and T. Radko (2003). “Residual-mean solutions for the Antarctic Circumpolar Current and its associated overturning circulation”. In: *Journal of Physical Oceanography* 33.11, pp. 2341–2354.

Marshall, J. and K. Speer (2012). “Closure of the meridional overturning circulation through Southern Ocean upwelling”. In: *Nature Geoscience* 5.3, p. 171.

Marshall, J. et al. (1997). “A finite-volume, incompressible Navier Stokes model for studies of the ocean on parallel computers”. In: *Journal of Geophysical Research: Oceans* 102.C3, pp. 5753–5766.

Mashayek, A. et al. (2015). “Influence of enhanced abyssal diapycnal mixing on stratification and the ocean overturning circulation”. In: *Journal of Physical Oceanography* 45.10, pp. 2580–2597.

McDougall, T. J. (1989). “Dianeutral advection”. In: *Parameterization of Small-Scale Processes: Proc.’Aha Huliko ’a Hawaiian Winter Workshop*, pp. 289–315.

McDougall, T. J. and R. Ferrari (2017). “Abyssal upwelling and downwelling driven by near-boundary mixing”. In: *Journal of Physical Oceanography* 47.2, pp. 261–283.

McManus, J. F. et al. (2004). “Collapse and rapid resumption of Atlantic meridional circulation linked to deglacial climate changes”. In: *Nature* 428.6985, p. 834.

Menemenlis, D. et al. (2005). “NASA supercomputer improves prospects for ocean climate research”. In: *Eos, Transactions American Geophysical Union* 86.9, pp. 89–96.

Menemenlis, D. et al. (2008). “ECCO2: High resolution global ocean and sea ice data synthesis”. In: *Mercator Ocean Quarterly Newsletter* 31, pp. 13–21.

Molemaker, M. J., J. C. McWilliams, and W. K. Dewar (2015). “Submesoscale instability and generation of mesoscale anticyclones near a separation of the California Undercurrent”. In: *Journal of Physical Oceanography* 45.3, pp. 613–629.

Moum, J. N. et al. (2004). “Convectively driven mixing in the bottom boundary layer”. In: *Journal of Physical Oceanography* 34.10, pp. 2189–2202.

Munk, W. H. (1966). “Abyssal recipes”. In: *Deep Sea Research and Oceanographic Abstracts*. Vol. 13. 4. Elsevier, pp. 707–730.

Murphy, D. M. et al. (2009). “An observationally based energy balance for the Earth since 1950”. In: *Journal of Geophysical Research: Atmospheres* 114.D17.

Naveira Garabato, A. C., A. Williams, and S. Bacon (2014). “The three-dimensional overturning circulation of the Southern Ocean during the WOCE era”. In: *Progress in Oceanography* 120, pp. 41–78.

Naveira Garabato, A. C. et al. (2007). “Short-circuiting of the overturning circulation in the Antarctic Circumpolar Current”. In: *Nature* 447.7141, p. 194.

Nikurashin, M. and R. Ferrari (2011). “Global energy conversion rate from geostrophic flows into internal lee waves in the deep ocean”. In: *Geophysical Research Letters* 38.8.

Nikurashin, M. and S. Legg (2011). “A mechanism for local dissipation of internal tides generated at rough topography”. In: *Journal of Physical Oceanography* 41.2, pp. 378–395.

Orsi, A. H., W. M. Smethie, and J. L. Bullister (2002). “On the total input of Antarctic waters to the deep ocean: A preliminary estimate from chlorofluorocarbon measurements”. In: *Journal of Geophysical Research: Oceans* 107.C8, pp. 31–1.

Orsi, A. H. and T. Whitworth III (2005). *Hydrographic Atlas of the World Ocean Circulation Experiment (WOCE) Volume 1: Southern Ocean*.

Orsi, A. H., T. Whitworth III, and W. D. Nowlin Jr (1995). “On the meridional extent and fronts of the Antarctic Circumpolar Current”. In: *Deep Sea Research Part I: Oceanographic Research Papers* 42.5, pp. 641–673.

Osborn, T. R. (1980). “Estimates of the local rate of vertical diffusion from dissipation measurements”. In: *Journal of Physical Oceanography* 10.1, pp. 83–89.

Perlin, A., J. N. Moum, and J. M. Klymak (2005). “Response of the bottom boundary layer over a sloping shelf to variations in alongshore wind”. In: *Journal of Geophysical Research: Oceans* 110.C10.

Perlin, A. et al. (2007). “Organization of stratification, turbulence, and veering in bottom Ekman layers”. In: *Journal of Geophysical Research: Oceans* 112.C5.

Phillips, O. M. (1970). “On flows induced by diffusion in a stably stratified fluid”. In: *Deep Sea Research and Oceanographic Abstracts*. Vol. 17. 3. Elsevier, pp. 435–443.

Phillips, O. M., J-H Shyu, and H. Salmun (1986). “An experiment on boundary mixing: mean circulation and transport rates”. In: *Journal of Fluid Mechanics* 173, pp. 473–499.

Polzin, K. L. et al. (1997). “Spatial variability of turbulent mixing in the abyssal ocean”. In: *Science* 276.5309, pp. 93–96.

Polzin, K. L. et al. (2014). “Boundary mixing in Orkney Passage outflow”. In: *Journal of Geophysical Research: Oceans* 119.12, pp. 8627–8645.

Pope, S. B. (2001). *Turbulent flows*.

Primeau, F. W. and M. Holzer (2006). “The ocean?s memory of the atmosphere: Residence-time and ventilation-rate distributions of water masses”. In: *Journal of Physical Oceanography* 36.7, pp. 1439–1456.

Rhein, M. et al. (2013). “Observations: ocean”. In: *Climate change*, pp. 255–316.

Rhines, P. B. (1986). “Vorticity dynamics of the oceanic general circulation”. In: *Annual Review of Fluid Mechanics* 18.1, pp. 433–497.

Rosso, I. et al. (2015). “Topographic influence on submesoscale dynamics in the Southern Ocean”. In: *Geophysical Research Letters* 42.4, pp. 1139–1147.

Ruan, X. and A. F. Thompson (2016). “Bottom Boundary Potential Vorticity Injection from an Oscillating Flow: A PV Pump”. In: *Journal of Physical Oceanography* 46.11, pp. 3509–3526.

Ruan, X. et al. (2017). “Contribution of topographically generated submesoscale turbulence to Southern Ocean overturning”. In: *Nature Geoscience* 10.11, pp. 840–845.

Sagaut, P. (2006). *Large eddy simulation for incompressible flows: an introduction*. Springer Science & Business Media.

Sarmiento, J. L. and J. R. Toggweiler (1984). “A new model for the role of the oceans in determining atmospheric pCO2”. In: *Nature* 308.5960, p. 621.

Schneider, T., I. M. Held, and S. T. Garner (2003). “Boundary effects in potential vorticity dynamics”. In: *Journal of Atmospheric Sciences* 60.8, pp. 1024–1040.

Scott, R. B. and Y. Xu (2009). “An update on the wind power input to the surface geostrophic flow of the World Ocean”. In: *Deep Sea Research Part I: Oceanographic Research Papers* 56.3, pp. 295–304.

Sen, A., R. B. Scott, and B. K. Arbic (2008). “Global energy dissipation rate of deep-ocean low-frequency flows by quadratic bottom boundary layer drag: Computations from current-meter data”. In: *Geophysical Research Letters* 35.9.

Shingai, K. and H. Kawamura (2002). “Direct numerical simulation of turbulent heat transfer in the stably stratified Ekman layer”. In: *Thermal Science & Engineering* 10, p. 25.

Sigman, D. M. and E. A. Boyle (2000). “Glacial/interglacial variations in atmospheric carbon dioxide”. In: *Nature* 407.6806, p. 859.

Silvester, J. M. et al. (2014). “Observations of a diapycnal shortcut to adiabatic upwelling of Antarctic Circumpolar Deep Water”. In: *Geophysical Research Letters* 41.22, pp. 7950–7956.

Sloyan, B. and S. R. Rintoul (2001). “The Southern Ocean limb of the global deep overturning circulation”. In: *Journal of Physical Oceanography* 31.1, pp. 143–173.

Smith, W. H. F. and D. T. Sandwell (1997). “Global sea floor topography from satellite altimetry and ship depth soundings”. In: *Science* 277.5334, pp. 1956–1962.

Spall, M. A. et al. (2008). “Western Arctic shelfbreak eddies: Formation and transport”. In: *Journal of Physical Oceanography* 38.8, pp. 1644–1668.

Speer, K., S. R. Rintoul, and B. Sloyan (2000). “The diabatic Deacon cell”. In: *Journal of physical oceanography* 30.12, pp. 3212–3222.

St Laurent, L. C. and A. M. Thurnherr (2007). “Intense mixing of lower thermocline water on the crest of the Mid-Atlantic Ridge”. In: *Nature* 448.7154, p. 680.

Stommel, H. and A. B. Arons (1959). “On the abyssal circulation of the world ocean–I. Stationary planetary flow patterns on a sphere”. In: *Deep Sea Research (1953)* 6, pp. 140–154.

Stone, P. H. (1966). “On non-geostrophic baroclinic stability”. In: *Journal of the Atmospheric Sciences* 23.4, pp. 390–400.

Talley, L. D. (2013). “Closure of the global overturning circulation through the Indian, Pacific, and Southern Oceans: Schematics and transports”. In: *Oceanography* 26.1, pp. 80–97.

Tamsitt, V. et al. (2017). “Spiraling pathways of global deep waters to the surface of the Southern Ocean”. In: *Nature communications* 8.1, p. 172.

Taylor, J. R. (2008). “Numerical simulations of the stratified oceanic bottom boundary layer”. PhD thesis. University of California, San Diego.

Taylor, J. R. and R. Ferrari (2010). “Buoyancy and wind-driven convection at mixed layer density fronts”. In: *Journal of Physical Oceanography* 40.6, pp. 1222–1242.

Taylor, J. R. and S. Sarkar (2008). “Stratification effects in a bottom Ekman layer”. In: *Journal of Physical oceanography* 38.11, pp. 2535–2555.

Thoma, M. et al. (2008). “Modelling circumpolar deep water intrusions on the Amundsen Sea continental shelf, Antarctica”. In: *Geophysical Research Letters* 35.18.

Thomas, L. N. (2005). “Destruction of potential vorticity by winds”. In: *Journal of physical oceanography* 35.12, pp. 2457–2466.

Thomas, L. N. and P. B. Rhines (2002). “Nonlinear stratified spin-up”. In: *Journal of Fluid Mechanics* 473, pp. 211–244.

Thomas, L. N. et al. (2013). “Symmetric instability in the Gulf Stream”. In: *Deep Sea Research Part II: Topical Studies in Oceanography* 91, pp. 96–110.

Thompson, A. F. and K. J. Heywood (2008). “Frontal structure and transport in the northwestern Weddell Sea”. In: *Deep Sea Research Part I: Oceanographic Research Papers* 55.10, pp. 1229–1251.

Thompson, A. F., A. L. Stewart, and T. Bischoff (2016). “A multibasin residual-mean model for the global overturning circulation”. In: *Journal of Physical Oceanography* 46.9, pp. 2583–2604.

Thompson, A. F. et al. (2014). “Eddy transport as a key component of the Antarctic overturning circulation”. In: *Nature Geoscience* 7.12, pp. 879–884.

Thorpe, S. A. (1987). “Current and temperature variability on the continental slope”. In: *Philosophical Transactions of the Royal Society of London. Series A, Mathematical and Physical Sciences* 323.1574, pp. 471–517.

– (2005). *The turbulent ocean*. Cambridge University Press.

Thurnherr, A. M. et al. (2005). “Mixing associated with sills in a canyon on the midocean ridge flank”. In: *Journal of physical oceanography* 35.8, pp. 1370–1381.

Todd, R. E. (2017). “High-frequency internal waves and thick bottom mixed layers observed by gliders in the Gulf Stream”. In: *Geophysical Research Letters* 44.12, pp. 6316–6325.

Toole, J. M. (2007). “Temporal characteristics of abyssal finescale motions above rough bathymetry”. In: *Journal of physical oceanography* 37.3, pp. 409–427.

Trowbridge, J. H. and S. J. Lentz (1991). “Asymmetric behavior of an oceanic boundary layer above a sloping bottom”. In: *Journal of Physical Oceanography* 21.8, pp. 1171–1185.

– (1998). “Dynamics of the bottom boundary layer on the northern California shelf”. In: *Journal of Physical Oceanography* 28.10, pp. 2075–2093.

Umlauf, L., W. D. Smyth, and J. N. Moum (2015). “Energetics of bottom Ekman layers during buoyancy arrest”. In: *Journal of Physical Oceanography* 45.12, pp. 3099–3117.

Walin, G. (1982). “On the relation between sea-surface heat flow and thermal circulation in the ocean”. In: *Tellus* 34.2, pp. 187–195.

Waterhouse, A. F. et al. (2014). “Global patterns of diapycnal mixing from measurements of the turbulent dissipation rate”. In: *Journal of Physical Oceanography* 44.7, pp. 1854–1872.

Weatherly, G. L. and P. J. Martin (1978). “On the structure and dynamics of the oceanic bottom boundary layer”. In: *Journal of Physical Oceanography* 8.4, pp. 557–570.

Wenegrat, J. O., J. Callies, and L. N. Thomas (2018). “Submesoscale baroclinic instability in the bottom boundary layer”. In: *Journal of Physical Oceanography* 48.11, pp. 2571–2592.

Whitworth, T. et al. (1998). “Water masses and mixing near the Antarctic Slope Front”. In: *Ocean, ice, and atmosphere: interactions at the Antarctic continental margin*, pp. 1–27.

Williams, R. G. and V. Roussenov (2003). “The role of sloping sidewalls in forming potential vorticity contrasts in the ocean interior”. In: *Journal of Physical Oceanography* 33.4, pp. 633–648.

Wolfe, C. L. and P. Cessi (2011). “The adiabatic pole-to-pole overturning circulation”. In: *Journal of Physical Oceanography* 41.9, pp. 1795–1810.

Woodgate, R. A. et al. (2001). “The Arctic Ocean boundary current along the Eurasian slope and the adjacent Lomonosov Ridge: Water mass properties, transports and transformations from moored instruments”. In: *Deep Sea Research Part I: Oceanographic Research Papers* 48.8, pp. 1757–1792.

Wright, C. J. et al. (2013). “Global observations of ocean-bottom subinertial current dissipation”. In: *Journal of Physical Oceanography* 43.2, pp. 402–417.

Wunsch, C. (1970). “On oceanic boundary mixing”. In: *Deep Sea Research and Oceanographic Abstracts*. Vol. 17. 2. Elsevier, pp. 293–301.

– (1998). “The work done by the wind on the oceanic general circulation”. In: *Journal of Physical Oceanography* 28.11, pp. 2332–2340.

Wunsch, C. and R. Ferrari (2004). “Vertical mixing, energy, and the general circulation of the oceans”. In: *Annual Review of Fluid Mechanics* 36, pp. 281–314.